Numerical Simulation and Subgrid-Scale Modeling of Mixing and Wall-Bounded Turbulent Flows

Thesis by

Daniel Chung

In Partial Fulfillment of the Requirements

for the Degree of

Doctor of Philosophy

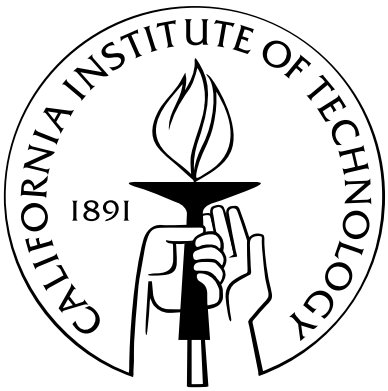

California Institute of Technology

Pasadena, California

2009

(Defended May 1, 2009)

Acknowledgements

I would like to thank my advisor Professor Dale Pullin who led our discussions with considerable skill and gave me much-needed encouragement in what turned out to be a challenging research project—I will never forget the first time I saw his blackboard illustration that was meant to describe my progress: a point on a hill located just before it slopes downward. Little did we know that the illustration had to make frequent appearances for another two years. Dale taught me the value of answering in the wrong way the right questions as opposed to answering in the right way the wrong questions; it was after I understood this principle that my research approach matured.

I would also like to express my appreciation to my thesis committee members, Professors Oscar Bruno, Tim Colonius, Mory Gharib, and Beverley McKeon, who took the time to read my thesis and offered suggestions that improved my thesis.

Thanks to everybody at GALCIT and Caltech, the research playground of the world. It was a privilege to associate with some of the smartest and funnest people who have and will continue to shape the future of our world. I would specifically like to thank the various members of the Iris and Puckett laboratories, Iván, Michio, Richard, Manuel, Mike and Karen, Andrew, and Yue. I would also like to thank my friends in the wider Caltech community for the memorable mountain-biking trips, beach days, and late-night parties: Waheb, Rogier, Chris and Lydia, Christian and Jennifer, Giselle, Vala, Sean and Marta, Liliya, Anusha, Aaron, Maria, Raviv, Angel, Alex, and Melanie.

Special thanks to Bill Bing, who ran the Caltech Monday Jazz Band with energy and passion—drumming for the Caltech MJB was one of the highlights of my week.

Thanks to Professors Min Chong and Andrew Ooi at The University of Melbourne, who first got me interested in fluid mechanics through their inspiring lectures and also gave me the opportunity to perform undergraduate research with their group; my interactions at Melbourne with Matteo, Keith, Anne, Malcolm, Jason, and Ronny instilled in me an appreciation for careful fluid mechanics research.

I am also fortunate to associate with friends from the Art Center College of Design: Michelle, Katherine, Eric, and Simone; I got to experience and learn about lots of awesome art.

Much thanks to Sumi and Maria who gave me the opportunity to bake with them at Europane; it was one of the most rewarding experiences of my graduate life. It is fair to say that the only

experiment in fluid mechanics that I performed during my graduate study is folding egg whites.

Thanks to Doctors David Hill and Carlos Pantano for conversations and e-mail exchanges that assisted me in understanding various numerical issues that cropped up in my research.

All the present computations were carried out on the excellently administrated Shared Heterogeneous Cluster (SHC) at the Caltech CACR, with access kindly provided by ASCI (Professor Dan Meiron) and PSAAP (Professor Michael Ortiz).

Thanks to Professor Beverley McKeon who gave us the idea for the material in chapter 5 during the summer of 2008.

I wish to thank Professor J. Jiménez who provided DNS spectra from $Re_\tau = 2\,\mathrm{k}$ channel flow, and Doctors W. H. Cabot and A. W. Cook who provided DNS spectra from high-Re Rayleigh–Taylor instability.

I would like to thank my parents, Edmund Chung and Goh Kwang Ging, as well as my brother, Collin Chung, who gave me their unconditional love, support, and encouragement during the course of my graduate study.

Finally, I thank God for giving me the undeserved opportunity to study at this amazing school—it was a blast.

This work is partially supported by the NSF under grant CBET 0651754.

Abstract

We extend the idea of multiscale large-eddy simulation (LES), the underresolved fluid dynamical simulation that is augmented with a physical description of subgrid-scale (SGS) dynamics. Using a vortex-based SGS model, we consider two areas of specialization: active (buoyant) scalar mixing and wall-bounded turbulence.

First, we develop a novel method to perform direct numerical simulation (DNS) of statistically stationary buoyancy-driven turbulence by using the fringe-region technique within a triply periodic domain, in which a mixing region is sandwiched between two fringes that supply the flow with unmixed fluids—heavy on top of light. Spectra exhibit small-scale universality, as evidenced by collapse in inner scales. A comparison with high-resolution DNS spectra from Rayleigh–Taylor turbulence reveals some similarities.

We perform LES of this flow to show that a passive scalar SGS model can also be used in an unstably stratified environment. LES spectra, including subgrid extensions, show good agreement with DNS data. For stably stratified flows, we develop an active scalar SGS model by performing a perturbation expansion in small Richardson numbers of the passive scalar SGS model to obtain an expression for the SGS scalar flux that contains buoyancy corrections.

We then develop a wall model for LES in which the near-wall region is unresolved. A special near-wall SGS model is constructed by averaging the streamwise momentum equation together with an assumption of local–inner scaling, giving an ordinary differential equation for the local wall shear stress that is coupled with the LES. An extended form of the stretched-vortex SGS model, which incorporates the production of near-wall Reynolds shear stresses due to the winding of streamwise momentum by near-wall attached SGS vortices, then provides a log relation for the off-wall LES boundary conditions. A Kármán-like constant is calculated dynamically as part of the LES. With this closure we perform LES of turbulent channel flow for friction-velocity Reynolds numbers $Re_\tau = 2\,\mathrm{k}$–$20\,\mathrm{M}$. Results, including SGS-extended spectra, compare favorably with DNS at $Re_\tau = 2\,\mathrm{k}$, and maintain an $O(1)$ grid dependence on Re_τ.

Finally, we apply the wall model to LES of long channels to capture effects of large-scale structures. Computed correlations are found to be consistent with recent experiments.

Contents

List of Figures

List of Tables

Chapter 1

Introduction

In the present research, we extend our capability to simulate complex fluid behavior. This research represents a contribution to the area of computational fluid dynamics, which has and will continue to have enormous impact on many diverse areas of science and engineering over a large range of Reynolds numbers, from the galactic scale, through climate modeling, to industrial and engineering applications.

The ideal is direct numerical simulation (DNS) in which all relevant physical processes are properly represented and all lengthscales are resolved. For turbulence this will include the Kolmogorov energy-dissipation scales and the Batchelor scalar-dissipation scales. At the large Reynolds numbers required for practical engineering applications, full DNS for all but the simplest physics and boundary conditions is unlikely to be practicable for many decades to come. The standard engineering prediction tool has been Reynolds-averaged modeling (RANS). Whilst RANS will remain useful for many applications, there is a growing need for a more detailed, DNS-like but computationally tractable, simulation capability in engineering. Examples include engine, energy, and environmental applications where physically realistic modeling of turbulent mixing, combustion, and near-wall flows is required. In particular, the absence of a reliable numerical simulation method at moderate cost for near-wall flows is perhaps the most severe roadblock to the further expansion of our present engineering prediction capabilities.

To address this growing need, we develop the multiscale large-eddy simulation (LES) approach in which conventional LES is enhanced by a physical representation of unresolved subgrid-scale (SGS) dynamics. While we do not expect to achieve DNS fidelity, we believe that multiscale LES can bring LES predictions substantially closer to the DNS ideal for many turbulent flows of practical interest, but at a small fraction of DNS cost. This is the focus of the present work. First, we describe the LES methodology.

1.1 LES

LES, the numerical simulation of fluid flow in which large-scale motion ("large eddy") is computed directly while small-scale motion is modeled, shows considerable potential for the underresolved but accurate simulation of complex turbulent flows. To date, an LES practitioner wishing to simulate a turbulent flow effectively assumes that the dynamics of large-scale, resolved eddies are dominated by the flow geometry along with associated large-scale boundary conditions or other turbulence-generating forcing. Accordingly, it is then thought sufficient to simulate numerically only those large eddies yet retain the capability to accurately recover at least first- and second-order statistics (means, correlations, and power spectral densities). The underlying ansatz is that the small scales are universal and can be parameterized in some way by the local resolved flow properties, with no explicit dependence on boundary conditions. If these assumptions are valid, successful LES should require only a computational grid that scales with flow geometry; specifically, the computational grid should be independent, $O(1)$ or weakly dependent, $O(\log Re)$, say, on the Reynolds number Re. LES promises enormous resource savings when compared to the prohibitively expensive but accurate DNS, where all scales of motion are computed. Typically, the required number of grid points for DNS scales as $O(Re^{9/4})$ (Rogallo and Moin 1984), which measures the size of the largest eddy relative to the smallest eddy in three dimensions. Further, the need to compute all scales, and then to perform massive data reduction renders DNS an inefficient and unpractical engineering design tool.

Also, fundamental questions in LES remain unanswered. For example, it is unclear how the LES resolved velocity is related to the observed real-world velocity. Pope (2004) provides some insight into this question. He argued that the relationship is one that is statistical. That is, the statistics of the observed velocity should only be compared to the model statistics obtained from the combination of both the LES resolved velocity and the modeled SGS motion. In particular, the statistics of the LES resolved velocity need not resemble the statistics obtained from the filtered observed velocity. This also raises the question of the meaning of LES-derived weather predictions at a given space and time, such as hurricane track predictions. In practice, the LES computation is correlated to the observed velocity up to a time horizon. For this reason, numerical weather prediction models are calibrated regularly to incorporate up-to-date observations. Indeed, even DNS, which aims to resolve all motions, but with finite resolution, is unable to provide accurate pointwise space–time predictions indefinitely.

Since the early work on LES by Smagorinsky (1963) and Deardorff (1970), LES has met with a mix of success and challenges. It is fair to say that the outcome of an LES depends largely on the validity of the assumptions held by our hypothetical LES practitioner. For flows in which these assumptions apply, typically unbounded flows, such as homogeneous isotropic turbulence (e.g.,

Misra and Pullin 1997), shear and wake/jet turbulence, and even the more challenging Richtmyer–Meshkov instability (e.g., Hill, Pantano and Pullin 2006), LES has performed exceedingly well. Despite continuing efforts, however (e.g., Cabot and Moin 1999, Voelkl, Pullin and Chan 2000, Piomelli and Balaras 2002, Wang and Moin 2002, Templeton, Medic and Kalitzin 2005, Piomelli 2008), the LES of wall-bounded flows, while improving, remains a challenging area of research.

One way forward is to augment LES with a physical description of the underlying SGS dynamics (multiscale LES). However, a detailed accounting of turbulence that contains all orders of statistical correlations is unnecessary at best and a waste of resources at worst since the main purpose of SGS modeling is to capture the average effects (low-order statistics) of the underresolved turbulence. Presently, this is accomplished via a simple vortex-based model of the SGS dynamics.

1.2 Vortex-Based SGS Model

Despite the complex nature of turbulence, simple vortex-based models have been successfully used to predict many statistical properties of turbulence (Lundgren 1982, Perry and Chong 1982, Pullin and Saffman 1994, Pullin and Lundgren 2001, O'Gorman and Pullin 2003). Presently, we focus on its use as a basis for SGS modeling in LES.

As an introduction to the central idea of the present work, consider the simple model of an initially linear passive-scalar field $c(r,\theta,t=0) = (\partial\widetilde{c}/\partial x) r\cos\theta$, under the convective action of a steady two-dimensional axisymmetric vortex (Pullin 2000), described by

$$\frac{\partial c}{\partial t} + \Omega(r)\frac{\partial c}{\partial \theta} = 0, \tag{1.1}$$

where $\Omega(r)$ is the angular velocity, (r,θ) are the cylindrical coordinates ($x = r\cos\theta$), and t is the time. The solution to (1.1) is

$$c(r,\theta,t) = \frac{\partial\widetilde{c}}{\partial x} r\cos\left(\theta - \Omega(r)t\right).$$

Averaging over volume, time, and initial conditions, the x-direction passive scalar flux generated by an ensemble of vortices characterized by scale Δ and kinetic energy K is (Pullin 2000)

$$\langle cu\rangle = -\frac{1}{2}\gamma\Delta K^{1/2}\frac{\partial\widetilde{c}}{\partial x},$$

where γ is an $O(1)$ constant. We will show that this highly stylized SGS model captures many essential aspects of turbulence, and we will exploit this model to extend the predictive capabilities of LES in the areas of active scalar mixing and wall-bounded turbulence. For active scalar mixing, we model the active scalar by adding buoyancy corrections to the passive scalar model, and for wall-bounded turbulence, we model the near-wall streamwise velocity as a passive scalar that is wound

by attached streamwise vortices.

1.3 Plan of Thesis

The two areas of the present research are active scalar mixing and wall-bounded turbulence. To better understand active scalar mixing, we propose a novel method to perform DNS of statistically stationary buoyancy-driven turbulence in chapter 2. In chapter 3, we develop an SGS model for active scalar mixing based on the vortex model given in § 1.2. We then shift our focus to developing a wall model for LES in chapter 4, again using ideas from § 1.2. Finally, we provide an application of the new wall model in chapter 5 before concluding in chapter 6. Owing to the different areas of specialization, each chapter will have its own set of notations.

Chapter 2

DNS of Statistically Stationary Buoyancy-Driven Turbulence

2.1 Background

The buoyancy-driven turbulent mixing of variable-density fluids arises in many applications, ranging from the naturally occurring exploding supernovae to the man-made inertial confinement fusion, and from the weighty subject of environmental pollution to the whimsical emptying of an inverted glass of water (Sandoval 1995, Cook and Dimotakis 2001, Dimotakis 2005). To better understand and predict these flows, researchers have proposed various ways to capture the essential physics of these flows in simple models that lend themselves to academic investigation through laboratory experiments, numerical simulations, and theoretical development.

In the spirit of such efforts, we propose a new model for the simulation of statistically stationary buoyancy-driven turbulent mixing of a variable-density fluid by employing a fringe region (Bertolotti, Herbert and Spalart 1992, Nordström, Nordin and Henningson 1999), which sustains an unstable density gradient within a triply periodic domain, in the presence of gravity. Following Sandoval (1995), we consider an incompressible binary fluid mixture comprised of fluids with microscopic densities ρ_1 and ρ_2, with the convention $\rho_2 > \rho_1$. Presently, we are interested in moderately high density ratios R ($\equiv \rho_2/\rho_1$), namely $R = 3$ and 7, a regime in which the Boussinesq assumption, formally $R = 1$, is no longer valid. The present model draws on many loosely related ideas from the literature; we will highlight some important similarities and differences in the following.

Overholt and Pope (1996), Yeung, Donzis and Sreenivasan (2005) simulated, in a triply periodic domain, the mixing of a passive scalar by forced isotropic–homogeneous turbulence embedded in background mean scalar gradient. Passive scalar fluctuations are continually produced by the background mean scalar gradient, but are kept in balance by diffusive dissipation, resulting in a statistically stationary flow. While, like Overholt and Pope (1996), our present model can also be viewed as a statistically stationary scalar-mixing flow in a background scalar gradient, there are two

important distinctions. First, the present model considers an active scalar, the mass fraction (algebraically related to the density), whose spatial variation is the source of buoyant potential energy that solely supplies the turbulent kinetic energy; in the model of Overholt and Pope (1996), the velocity field is forced externally. Second, the active scalar precludes a straightforward extension of the Overholt and Pope (1996) model for sustaining a passive scalar gradient because the resulting equations for the active scalar fluctuations can no longer be simulated in a triply periodic domain. We adapt the fringe-region technique (Bertolotti, Herbert and Spalart 1992) to our problem to overcome this difficulty.

Employing the Boussinesq assumption, Batchelor, Canuto and Chasnov (1992) studied the buoyancy-driven turbulent mixing of an active scalar in a triply periodic domain. A feature absent in Boussinesq flows is baroclinic vorticity, generated by misalignments between pressure and density gradients. Later, Sandoval (1995) and Livescu and Ristorcelli (2007, 2008) performed similar computations, generalizing to higher density ratios, and without using the Boussinesq assumption. All of these flows were initialized with blobs of unmixed fluid and allowed to decay as the initial potential energy is converted to kinetic energy, which drives the turbulent mixing, before it is finally dissipated by diffusion. Like Sandoval (1995), we presently compute the turbulent mixing of a moderately high-R incompressible binary fluid mixture within a triply periodic domain, but we additionally use a fringe region to sustain an unstable density gradient (heavy fluid on top of light fluid) to produce a statistically stationary flow.

Perhaps the most widely used model to study buoyancy-driven turbulent mixing is the Rayleigh–Taylor instability (e.g., Cook and Dimotakis 2001, Cook, Cabot and Miller 2004, Cabot and Cook 2006, Mueschke and Schilling 2009), where an initial perturbed interface separating unmixed heavy fluid on top of light fluid is accelerated toward the light fluid, resulting in a growing turbulent mixing layer. Rayleigh–Taylor instability is a statistically evolving flow, requiring expensive computational resources (e.g., Cabot and Cook 2006) to capture late-time asymptotic self-similar statistics. Our present simulations can perhaps be viewed as a model for the late-time Rayleigh–Taylor instability deep within the interior of the turbulent mixing zone, where the slowly evolving fine-scale turbulence is informed of the far-field boundary conditions only through the unstable density gradient. The analogy is incomplete, however, as a statistically evolving flow is fundamentally different to a statistically stationary flow. Two other flows that are related in this same way are forced isotropic–homogeneous turbulence and decaying isotropic–homogeneous turbulence.

A somewhat related flow is the closed-vessel experiment of Krawczynski et al. (2006), where passive scalar mixing is achieved by a continual injection of unmixed fluids from a series of impinging jets, resulting in a statistically stationary homogeneous isotropic turbulent flow. In the present simulations, the role of the jets is played by the fringe region, where unmixed fluids are continually introduced into the domain. Again, we consider a dynamically active scalar, and unlike the jets in

the experiment, the fringe region is not a source of momentum.

The plan of the chapter is as follows. The governing equations with source terms and the variable-density incompressible fluid model is introduced in § 2.2.1. We then determine the restrictions on the source terms when solving these equations in a triply periodic domain (§ 2.2.2). In § 2.2.3, we introduce our adaptation of the fringe-region technique, and then prescribe a condition on the external pressure gradient in § 2.2.4. A new method for solving the governing equations that guarantees discrete mass conservation, regardless of iteration errors, is described in § 2.3.1. The numerical discretization is detailed in § 2.3.2. We present results, including profiles of integral quantities, comparisons of present spectra with the Rayleigh–Taylor instability spectra of Cabot and Cook (2006) and mole fraction probability density functions in § 2.4.

2.2 Problem Description

2.2.1 Governing Equations

The species mass conservation equation and the Navier–Stokes equations govern the flow of a binary fluid mixture (see Sandoval 1995, Cook and Dimotakis 2001, Livescu and Ristorcelli 2007):

$$\frac{\partial}{\partial t}\left(\rho Y_1\right) + \frac{\partial}{\partial x_j}\left(\rho Y_1 u_j - \mathcal{D}\rho\frac{\partial Y_1}{\partial x_j}\right) = \omega_1, \tag{2.1}$$

$$\frac{\partial \rho}{\partial t} + \frac{\partial}{\partial x_j}\left(\rho u_j\right) = 0, \tag{2.2}$$

$$\frac{\partial}{\partial t}(\rho u_i) + \frac{\partial}{\partial x_j}\left(\rho u_i u_j + p\delta_{ij} - \tau_{ij}\right) = -\Gamma_i - \rho g \delta_{i3}, \tag{2.3}$$

where ρ is the density; u_i is the velocity; p is the pressure; $\Gamma_i(t)$ is the uniform pressure gradient; g is the magnitude of the gravitational acceleration that acts in the negative z-direction; $\omega_1(\boldsymbol{x}, t)$ is the source of fluid 1; x_i is the spatial coordinate; t is the time; and Y_1 is the mass fraction of fluid 1. We use the notations, $(x, y, z) = (x_1, x_2, x_3)$ and $(u, v, w) = (u_1, u_2, u_3)$, interchangeably. The mass fraction of fluid 2 is obtained from $Y_1 + Y_2 = 1$; its evolution equation need not be computed separately. Observe, from the right-hand side of (2.2), that there is no net source of mass, and so the source of fluid 1 must equal the sink of fluid 2, $\omega_1(\boldsymbol{x}, t) + \omega_2(\boldsymbol{x}, t) = 0$. τ_{ij} is the Newtonian viscous stress tensor, given by

$$\tau_{ij} = \mu\left(\frac{\partial u_i}{\partial x_j} + \frac{\partial u_j}{\partial x_i} - \frac{2}{3}\delta_{ij}\frac{\partial u_k}{\partial x_k}\right).$$

The nondimensional parameters that characterize the present flow are the Reynolds, Schmidt and Froude numbers, defined as

$$Re \equiv \rho_0 U\ell/\mu, \quad Sc \equiv \mu/(\rho_0 \mathcal{D}), \quad Fr^2 \equiv U^2/(g\ell),$$

where ρ_0 is the density scale; U is the velocity scale; ℓ is the lengthscale; $\mu = \mu_1 = \mu_2$ is the constant matched dynamic viscosity for both fluids; and $\mathcal{D}$ is the Fickian diffusion coefficient.

Density variation arises purely from variation in the local fluid composition. The relevant equation of state is then (Sandoval 1995)

$$\frac{1}{\rho(\boldsymbol{x},t)} = \frac{Y_1(\boldsymbol{x},t)}{\rho_1} + \frac{Y_2(\boldsymbol{x},t)}{\rho_2} = Y_1(\boldsymbol{x},t)\left(\frac{1}{\rho_1} - \frac{1}{\rho_2}\right) + \frac{1}{\rho_2}, \tag{2.4}$$

where ρ_1 and ρ_2 are the constant microscopic densities of their respective fluids. We fix the density scale $\rho_0 = (\rho_1 + \rho_2)/2$ so that

$$\frac{\rho_1}{\rho_0} = 1 - A \quad \text{and} \quad \frac{\rho_2}{\rho_0} = 1 + A, \quad \text{where} \quad A \equiv \frac{\rho_2 - \rho_1}{\rho_2 + \rho_1} = \frac{R-1}{R+1} > 0, \tag{2.5}$$

the Atwood number. Next, fix the velocity scale,

$$U = (Ag\ell)^{1/2} \quad \Rightarrow \quad Re = \rho_0 (Ag\ell)^{1/2}\ell/\mu, \quad Fr^2 = A,$$

making Re, Sc and A the three independent parameters for this flow. Presently, $Sc = 1$; we then perform a parametric study in the (Re, A) space.

We eliminate Y_1 by combining (2.1) and (2.4), and then using (2.2) to get

$$\frac{\partial u_j}{\partial x_j} = -\mathcal{D}\frac{\partial}{\partial x_j}\left(\frac{1}{\rho}\frac{\partial \rho}{\partial x_j}\right) - \omega_s, \quad \text{where} \quad \omega_s \equiv \left(\frac{1}{\rho_2} - \frac{1}{\rho_1}\right)\omega_1, \tag{2.6}$$

in contrast to constant density flows, where $\partial u_j/\partial x_j = 0$. We combine (2.6) and (2.2) to write

$$\frac{\partial s}{\partial t} + u_j \frac{\partial s}{\partial x_j} = \mathcal{D}\frac{\partial^2 s}{\partial x_j^2} + \omega_s, \tag{2.7}$$

where $s \equiv \log(\rho/\rho_0)$. We will use (2.7) as an alternative evolution equation for ρ.

2.2.2 Consequences of Periodicity

We wish to compute a nontrivial solution to the governing equations in a periodic domain. Given this constraint, we will now determine how to obtain a flow that is statistically stationary by choosing ω_1 in (2.1) or equivalently ω_s in (2.6). Denote the volume average by $\overline{(\,)}$, then periodicity implies

$\overline{\partial(\,)/\partial x_j} = 0$. From (2.1) and (2.2),

$$\frac{\partial}{\partial t}\overline{\rho Y_1} = \overline{\omega}_1, \quad \frac{\partial \overline{\rho}}{\partial t} = 0. \tag{2.8}$$

Without loss of generality, set $\overline{\rho} = \rho_0$. We rearrange (2.4) and (2.5), then average, to get

$$\overline{\rho Y_1} = (1 - \overline{\rho}/\rho_2)\,/(1/\rho_1 - 1/\rho_2) = \rho_1/2 = \rho_0(1-A)/2.$$

Likewise, $\overline{\rho Y_2} = \rho_0(1+A)/2$. Since $\overline{\rho Y_1}$ is a constant, (2.8) necessarily implies that $\overline{\omega}_1 = \overline{\omega}_s = 0$ at every instant of time.

Decomposing $\rho = \overline{\rho} + \rho'$, we can obtain the evolution equation for ρ'^2 from (2.2):

$$\frac{\partial \rho'^2}{\partial t} + \frac{\partial\left(u_j \rho'^2\right)}{\partial x_j} + \left(\rho^2 - \overline{\rho}^2\right)\frac{\partial u_j}{\partial x_j} = 0. \tag{2.9}$$

Use (2.6) to calculate

$$\rho^2 \frac{\partial u_j}{\partial x_j} = -\mathcal{D}\left[\frac{\partial^2}{\partial x_j^2}\left(\frac{1}{2}\rho^2\right) - 2\left(\frac{\partial \rho}{\partial x_j}\right)^2\right] - \rho^2 \omega_s,$$

which we then combine with the volume average of (2.9) to obtain the equation governing the density fluctuation variance:

$$\frac{\partial \overline{\rho'^2}}{\partial t} = -2\mathcal{D}\overline{\left(\frac{\partial \rho'}{\partial x_j}\right)^2} + \overline{\rho^2 \omega_s}. \tag{2.10}$$

Denote the long-time average by $\langle\,\rangle_\infty$, then $\langle \partial(\,)/\partial t\rangle_\infty = 0$ for any statistically stationary quantity. Time averaging (2.10),

$$2\mathcal{D}\left\langle \overline{(\partial\rho'/\partial x_j)^2}\right\rangle_\infty = \left\langle \overline{\rho^2\omega_s}\right\rangle_\infty > 0. \tag{2.11}$$

We choose $\omega_s(\boldsymbol{x}, t) = 0$ except in a region called the fringe. Then (2.11) says that, over time, the source of unmixed fluids, introduced in the fringe, necessarily balances the mixing occurring outside the fringe, resulting in a statistically stationary flow.

2.2.3 Fringe-Region Forcing

A source of unmixed fluids in unstable configuration (heavy fluid on top of light fluid) is required for buoyancy forces to drive the turbulent mixing process. In Rayleigh–Taylor turbulence, the infinite reservoirs of unmixed fluid supply the mixing zone, but the flow is not stationary owing to the growing height of the mixing zone. The kind of stationary flow that we envision presently has similarities with the partially stirred reactor of Krawczynski et al. (2006), which was used to study passive scalar mixing by jet-driven turbulence in a closed vessel. In our case, the scalar is active and

the turbulence is driven by buoyancy (not momentum).

Our goal is to simulate a turbulent mixing flow in a triply periodic domain. In the absence of any forcing, the flow decays, which is the flow computed by Livescu and Ristorcelli (2007). The present approach is to approximate the mixing chamber by using the fringe-region technique (e.g., Bertolotti, Herbert and Spalart 1992, Nordström, Nordin and Henningson 1999). A natural choice is to apply the technique directly to the source term ω_1 in (2.1):

$$\omega_1(\boldsymbol{x},t) = \Lambda_1\lambda_1(\boldsymbol{x})\rho_1 Y_2(\boldsymbol{x},t) - \Lambda_2\lambda_2(\boldsymbol{x})\rho_2 Y_1(\boldsymbol{x},t), \tag{2.12a}$$

or equivalently, using (2.4) and (2.6),

$$\omega_s(\boldsymbol{x},t) = \Lambda_1\lambda_1(\boldsymbol{x})(\rho_1/\rho(\boldsymbol{x},t) - 1) + \Lambda_2\lambda_2(\boldsymbol{x})(\rho_2/\rho(\boldsymbol{x},t) - 1), \tag{2.12b}$$

where $0 \le \lambda_1, \lambda_2 \le 1$ are the smooth fringe indicator functions (1 inside the fringe region, 0 outside the fringe region) corresponding to the respective fluid sources. Momentarily setting $(\lambda_1, \lambda_2) = (1, 0)$ in (2.12a), observe that the rate at which the light fluid is introduced in the flow is proportional to its microscopic density ρ_1 and its mass fraction deficit $Y_2 = 1 - Y_1$. A similar statement can be made for the heavy fluid source. The indicator functions are defined by

$$\lambda_1(\boldsymbol{x}) = \xi_1(x,y)\left[\Pi(z; 0, 0 + L_f) + \Pi(z; L_z, L_z + L_f)\right], \tag{2.13a}$$

$$\lambda_2(\boldsymbol{x}) = \xi_2(x,y)\left[\Pi(z; 0 - L_f, 0) + \Pi(z; L_z - L_f, L_z)\right], \tag{2.13b}$$

where L_z is the height of the periodic domain, shown in figure 2.1(a); $L_f/\ell = 2\pi/10$, the height of the fringe region; $0 \le \xi_1, \xi_2 \le 1$ are planar indicator functions to be defined; and Π is a top-hat function constructed from smooth step functions S (see figure 2.1(b))

$$\Pi(z; z_{\text{start}}, z_{\text{end}}) = S\left(\frac{z - z_{\text{start}}}{\Delta_{\text{rise}}} + \frac{1}{2}\right) - S\left(\frac{z - z_{\text{end}}}{\Delta_{\text{fall}}} + \frac{1}{2}\right), \tag{2.14a}$$

$$S(z) = \begin{cases} 0, & z \le 0, \\ 1/\left[1 + \exp\left(\frac{1}{z-1} + \frac{1}{z}\right)\right], & 0 < z < 1, \\ 1, & z \ge 1. \end{cases} \tag{2.14b}$$

We choose transition widths $\Delta_{\text{rise}} = \Delta_{\text{fall}} = 6\Delta_z$, where Δ_z is the computational grid height. $\lambda_1(\boldsymbol{x})$ and $\lambda_2(\boldsymbol{x})$ in (2.13) are chosen so that heavy fluid is introduced at the top of the flow domain and light fluid is introduced at the bottom of the domain. We use Π twice in each of (2.13) to preserve vertical periodicity.

The planar indicator functions have zero mean: $\langle\xi_1(x,y)\rangle = \langle\xi_2(x,y)\rangle = 0$, where $\langle\ \rangle$ denotes the

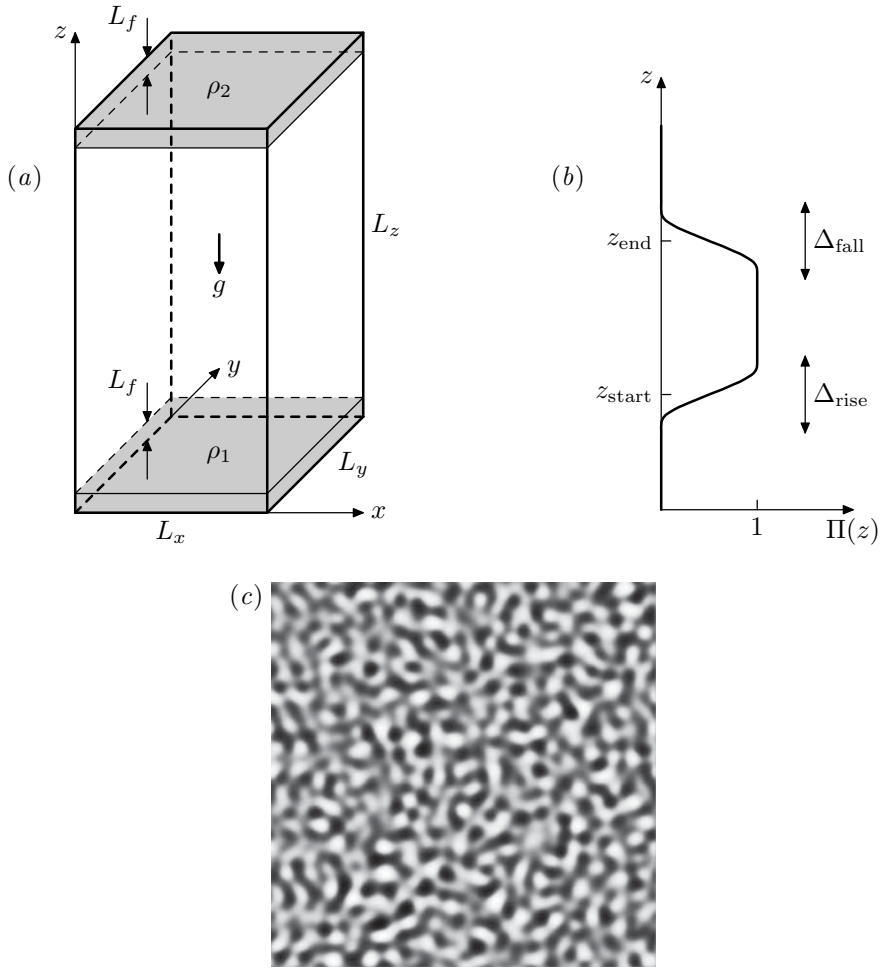

Figure 2.1. (a) Triply periodic flow domain showing the shaded fringe regions that supply the flow with unmixed fluids, heavy above light ($\rho_2 > \rho_1$). (b) Features of the smooth function $\Pi(z)$, $(2.14a)$, used to locate the fringe region. (c) Horizontal slice of the planar indicator function $\xi_1(x, y)$, constructed from applying the Gaussian spectral filter to a physical i.i.d. random field of $N(0, 1)$. The filter is centered on wavenumber $k_0\ell$ corresponding to wavelength $\lambda_0/\ell = 2\pi/16$ and the box shown has dimensions $2\pi\ell \times 2\pi\ell$.

xy-plane average. They are constructed in a manner similar to the construction of the perturbation field used by Cook, Cabot and Miller (2004). Briefly, independent and identically distributed (i.i.d.) normal random variables with zero mean and unit variance, $N(0,1)$, are assigned to each (x,y) grid point. We transform this field to Fourier space and apply a Gaussian filter centered on wavenumber $k_0\ell = 16$ with standard deviation $\sigma_k\ell = 4$. The resulting field is transformed back to physical space with value $\zeta(x,y)$ and steepened with the function

$$\xi_1(x,y) = 1/2 + \arctan[\pi\zeta(x,y)/(3\sigma_\zeta)]/\pi,$$

where σ_ζ is the standard deviation of ζ. A contour plot of ξ_1 is shown in figure 2.1(c).

Omitting convection and diffusion in (2.7), then substituting (2.12b), we obtain the simple balance between the source term and the unsteady term in the fringe:

$$\frac{\partial\rho}{\partial t} = \begin{cases} \Lambda_1(\rho_1 - \rho) & \text{if} \quad (\lambda_1,\lambda_2) = (1,0), \\ \Lambda_2(\rho_2 - \rho) & \text{if} \quad (\lambda_1,\lambda_2) = (0,1). \end{cases} \tag{2.15}$$

Observe that ω_s is designed to force $\rho(\boldsymbol{x},t)$ following a fluid particle to track ρ_1 (or ρ_2) at the rate Λ_1 (or Λ_2). The fringe region parameters, Λ_1 and Λ_2, are similar to the Damköhler number used in chemical reactions—it measures the strength of the source of unmixed fluids, introduced in the fringe, relative to the flow. The parameters, Λ_1 and Λ_2, can also be interpreted as inverse time constants of first-order systems, clearly seen in structure of (2.15). They are not independent; recall from § 2.2.2 the constraint $\overline{\omega}_1 = 0$, implying that

$$\Lambda_1\overline{\lambda_1(\boldsymbol{x},t)(\rho_1/\rho - 1)} + \Lambda_2\overline{\lambda_2(\boldsymbol{x},t)(\rho_2/\rho - 1)} = 0.$$

It remains to fix the upper limit:

$$\Lambda = \max\{\Lambda_1, \Lambda_2\}.$$

We use an order-of-magnitude argument to choose Λ. Since the fringe introduces unmixed fluids with densities ρ_1 and ρ_2 in a layer of width L_f subjected to gravity g, its characteristic velocity scale is $U_f = (AgL_f)^{1/2}$. The time it takes for a fluid particle to transit through fringe is $T_f = L_f/U_f = (L_f/Ag)^{1/2}$. We then choose $\Lambda(\ell/Ag)^{1/2} = 10$, which is much larger than the transit rate, $(\ell/Ag)^{1/2}/T_f = (\ell/L_f)^{1/2} = (10/2\pi)^{1/2} \approx 1.26$, a source rate high enough, relative to the flow, in order for $\rho(\boldsymbol{x},t)$ to take on the desired values ρ_1 or ρ_2.

2.2.4 Mean Pressure Gradient

A model is required for $\Gamma_i(t)$, the externally imposed spatially uniform pressure gradient. In Rayleigh–Taylor turbulence, the far-field quiescent boundary conditions determines Γ_i felt in the turbulent mixing zone. In a triply periodic domain where such far-field boundary conditions cannot be directly imposed, we model Γ_i by requiring that $\langle \partial u_i/\partial t \rangle_{z=L_z/2} = 0$, where $\langle\ \rangle_{z=L_z/2}$ denotes the xy-plane average taken at the $z = L_z/2$ plane (midplane). As noted by Livescu and Ristorcelli (2007), $\langle \partial u_i/\partial t \rangle_{z=L_z/2} \approx 0$ in the turbulent mixing zone, who considered a similar model by choosing $\partial \overline{u}_i/\partial t = 0$. For definiteness, we choose $\langle u_i \rangle_{z=L_z/2} = 0$.

Alternatively, Γ_i can also be determined from the volume average of (2.3),

$$\frac{\partial}{\partial t}\overline{\rho u_i} = -\Gamma_i(t) - \overline{\rho} g \delta_{i3}.$$

Upon taking the long-time average, the $\partial/\partial t$ term vanishes, and we obtain $\langle \Gamma_i \rangle_\infty = -\overline{\rho} g \delta_{i3}$. That is, over time, $\Gamma_i(t)$ fluctuates about its theoretical steady state. We use this result to check the internal consistency of our code.

2.3 Solution Method

2.3.1 Alternative Lagrange Multiplier to Pressure

In incompressible flows, a constraint on the velocity divergence has to be satisfied at all times. For variable density flows, the constraint is (2.6), while for constant density flows, the constraint is $\partial u_j/\partial x_j = 0$. This is enforced by treating p as a Lagrange multiplier. The elliptic equation for p is obtained by taking the divergence of (2.3), then enforcing the constraint (2.6). In constant density flows, this results in a constant-coefficient Poisson equation for p, which is readily solved. The nonconstant $1/\rho$ factor in variable density flows presents an additional complication.

This issue appears in a variety of forms in the literature and cannot be circumvented. Sandoval (1995) and Cook and Dimotakis (2001), for example, take the divergence of (2.3), resulting in a constant-coefficient Poisson equation for p, but use what amounts to a lower-order extrapolation for $\partial u_i/\partial t$, reducing the overall accuracy of the temporal discretization. Consequently, mass conservation in the form of (2.6) is never satisfied instantaneously. The advantage to their approach is that no iterations are required. Another approach to this issue is proposed by Livescu and Ristorcelli (2007), who derive an exact nonlinear equation for p (equation A15 in that paper) that requires an iterative solution method but eliminates temporal discretization errors. However, it remains that (2.6) cannot be discretely satisfied owing to the inevitable finite spatial resolution, even if infinite iterations were possible.

Our approach eliminates some, but not all, of these difficulties. For clarity, continuous differential operators will be used in the exposition but the method applies directly to their discrete counterparts. First, expand (2.3) and use (2.2) to get

$$\frac{\partial u_i}{\partial t} = -\frac{1}{\rho}\left(\frac{\partial p}{\partial x_i} + \Gamma_i\right) - u_j\frac{\partial u_i}{\partial x_j} + \frac{1}{\rho}\frac{\partial \tau_{ij}}{\partial x_j} - g\delta_{i3}. \tag{2.16}$$

The idea is to use the following Helmholtz–Hodge decomposition (Chorin and Marsden 1993):

$$\frac{1}{\rho}\left(\frac{\partial p}{\partial x_i} + \Gamma_i\right) = \frac{\partial \phi}{\partial x_i} + h_i + f_i, \quad h_i = \epsilon_{ijk}\frac{\partial \psi_k}{\partial x_j}. \tag{2.17}$$

That is, instead of (p, Γ_i), we use the alternative Lagrange multipliers (ϕ, ψ_i, f_i): ϕ is the scalar potential; ψ_i is the vector potential; and f_i is the harmonic component. With periodic boundary conditions, the harmonic component $f_i(t)$ is spatially uniform. Put (2.17) back into (2.16) to obtain

$$\frac{\partial u_i}{\partial t} = \frac{\partial \phi}{\partial x_i} + h_i + f_i + H_i, \tag{2.18}$$

where H_i contains the remaining terms in (2.16). Taking the divergence of (2.18) immediately gives a constant-coefficient Poisson equation for ϕ with a known right-hand side:

$$\frac{\partial^2 \phi}{\partial x_j^2} = \frac{\partial}{\partial t}\left(\frac{\partial u_j}{\partial x_j}\right) - \frac{\partial H_j}{\partial x_j},$$

where $\partial u_j/\partial x_j$ is found from (2.6). The solution to the discrete form of this equation is straightforward. Next, f_i is found from taking the $z = L_z/2$ plane average of (2.18) and applying the model boundary condition (§ 2.2.4): $\langle \partial u_i/\partial t \rangle_{z=L_z/2} = 0$ so

$$f_i(t) = -\left\langle \frac{\partial \phi}{\partial x_i} + h_i + H_i \right\rangle_{z=L_z/2}.$$

To solve for h_i, we first multiply (2.17) by ρ, then take the curl, giving a zero left-hand side:

$$0 = \epsilon_{ijk}\frac{\partial}{\partial x_j}\left[\rho\left(\frac{\partial \phi}{\partial x_k} + h_k + f_k\right)\right],$$

This is essentially the equation for h_i. We can simplify this further by splitting $\rho = \overline{\rho} + \rho'$ and using the gauge $\partial \psi_j/\partial x_j = 0$,

$$\frac{\partial^2 \psi_i}{\partial x_j^2} = \epsilon_{ijk}\frac{\partial}{\partial x_j}\left[\frac{\rho'}{\overline{\rho}}\left(\frac{\partial \phi}{\partial x_k} + h_k + f_k\right)\right].$$

Finally, take the curl again to obtain the nonlinear equation

$$\frac{\partial^2 h_i}{\partial x_j^2} = \frac{\partial}{\partial x_i}\frac{\partial B_j}{\partial x_j} - \frac{\partial^2 B_i}{\partial x_j^2}, \quad B_i = \frac{\rho'}{\overline{\rho}}\left(\frac{\partial \phi}{\partial x_i} + h_i + f_i\right). \tag{2.19}$$

We solve this by iterating: use the current $h_i^{(n)}$ in the right-hand side $B_i^{(n+1)}$ of the Poisson equation for the next $h_i^{(n+1)}$. If the density is constant, $\rho' = 0 \Rightarrow B_i = 0 \Rightarrow h_i = 0$ to recover $(p, \Gamma_i) = (\phi, f_i)$, verifiable from (2.19) and (2.17).

Using (2.17) allows the exact satisfaction of mass conservation (2.1) at every time instant and up to the machine precision of the spatial discretization, regardless of iteration errors in (2.19). This is because the part of the Lagrange multiplier $(1/\rho)(\partial p/\partial x_i)$ that plays the role of mass conservation is completely encapsulated by its curl-free component $\partial\phi/\partial x_i$. All errors from this method are isolated to iteration residuals in h_i. In the vorticity equation, its curl, $\epsilon_{ijk}\partial h_k/\partial x_j$, is the baroclinic source of vorticity. In physical terms, the present approach eliminates mass conservation errors but incurs errors on baroclinic vorticity. However, the vorticity equation is always subject to temporal discretization errors. A similar approach for the zero-divergence incompressible equations is taken by Chang, Giraldo and Perot (2002). Presently we control this error by iterating until $||h_i^{(n+1)} - h_i^{(n)}||/||h_i^{(n)}|| < 10^{-2}$, where $||\ ||$ denotes the L_2-norm. In practise, this takes 1–2 iterations.

Since p and Γ_i have been replaced by ϕ, ψ_i, and f_i, they are not required for the time integration of the governing equations. If required for diagnostics, they are readily calculated from

$$\frac{\partial^2 p}{\partial x_j^2} = \frac{\partial}{\partial x_j}\left[\rho\left(\frac{\partial\phi}{\partial x_j} + h_j + f_j\right)\right], \quad \Gamma_i(t) = \overline{\left[\rho\left(\frac{\partial\phi}{\partial x_i} + h_i + f_i\right)\right]}.$$

We remark that the satisfaction of discrete mass conservation is only one of many ways to assess the "goodness" of a solution. However, anecdotal evidence in the literature suggests that discrete mass conservation is important for numerical stability. Sandoval (1995), for example, reports numerical instability when the density ratio is large. Using the present discretization, no such numerical instability was found, even when $R = 7$. A study exploring the direct link between discrete mass conservation and numerical stability is beyond the scope of this work.

2.3.2 Numerical Discretization

The governing equations, in the form (2.6), (2.7), and (2.16), are discretized using the low-storage semi-implicit Runge-Kutta method of Spalart, Moser and Rogers (1991). Briefly, the method consists of three sequential substeps of the following form:

$$\frac{s^{(n+1)} - s^{(n)}}{\Delta_t} = \gamma H_s^{(n)} + \zeta H_s^{(n-1)} + \alpha\mathcal{D}\frac{\partial^2}{\partial x_j^2}s^{(n)} + \beta\mathcal{D}\frac{\partial^2}{\partial x_j^2}s^{(n+1)}, \tag{2.20a}$$

$$\frac{u_i^{(n+1)} - u_i^{(n)}}{\Delta_t} = \gamma H_i^{(n)} + \zeta H_i^{(n-1)} + \alpha\frac{\mu}{\rho_0}\frac{\partial^2}{\partial x_j^2}u_i^{(n)} + \beta\frac{\mu}{\rho_0}\frac{\partial^2}{\partial x_j^2}u_i^{(n+1)} - \frac{(\alpha+\beta)}{\rho^{(*)}}\left(\frac{\partial p}{\partial x_i} + \Gamma_i\right), \tag{2.20b}$$

$$\frac{\partial}{\partial x_j}u_j^{(n+1)} = -\mathcal{D}\frac{\partial^2}{\partial x_j}s^{(n+1)} - \omega_s^{(n+1)}, \tag{2.20c}$$

where

$$H_s = -u_j \frac{\partial s}{\partial x_j} + \omega_s,$$
$$H_i = -u_j \frac{\partial u_i}{\partial x_j} + \frac{\mu}{\rho_0}\left[\left(\frac{\rho_0}{\rho} - 1\right)\frac{\partial^2 u_i}{\partial x_j^2} + \frac{\rho_0}{\rho}\frac{1}{3}\frac{\partial}{\partial x_i}\frac{\partial u_j}{\partial x_j}\right] - g\delta_{i3},$$

$\rho \equiv \rho_0 \exp(s)$; $(\alpha+\beta)/\rho^{(*)} \equiv \alpha/\rho^{(n)} + \beta/\rho^{(n+1)}$; and ω_s is given by (2.12b). The values for α, β, γ, and ζ, different for each substep, are given in Spalart, Moser and Rogers (1991). For stability, we have chosen to split the viscous operator into the linear component, which we treat implicitly, and the nonlinear component, which we treat explicitly. Discretizing s, $\in (\infty, \infty)$, rather than ρ ensures that $\rho > 0$, but then, $\overline{\rho} = \rho_0$ can no longer be maintained discretely; we presently control this numerical drift with a small proportional control added to Λ_1 and Λ_2. The Courant–Friedrichs–Levy condition is dynamically adjusted so that

$$\Delta_t \max_{i=1,2,3} \{|u_i|/\Delta_i\} = 0.7,$$

where $\Delta_i \equiv L_i/N_i$. Presently, $\Delta \equiv \Delta_1 = \Delta_2 = \Delta_3$ everywhere.

The spatial discretization of (2.20) employs the Fourier pseudospectral method (e.g., Canuto et al. 1987), where the products and nonlinear terms in H_i and H_s are computed in physical space, then transformed to spectral space for the 2/3-rule dealiasing. The maximum dealiased wavenumber is then $(2/3)(\pi/\Delta)$, where Δ is the grid size. The 2/3-rule eliminates all aliasing errors arising from double products, but some higher-order aliasing from quotients and exponentials remains.

The steps for solving the system (2.20) are as follows: First, solve (2.20 a), and then solve (2.20 b), choosing the Lagrange multipliers (ϕ, ψ_i, f_i), where

$$\frac{1}{\rho^{(*)}}\left(\frac{\partial p}{\partial x_i} + \Gamma_i\right) \equiv \frac{\partial \phi}{\partial x_i} + \epsilon_{ijk}\frac{\partial \psi_k}{\partial x_j} + f_i,$$

so that (2.20 c) is discretely satisfied and that $\langle u_i^{n+1}\rangle_{z=L_z/2} = 0$. The latter step of determining the Lagrange multipliers is described using continuous operators in § 2.3.1.

2.3.3 Code Validation

As validation of our code, we reproduce the case 3Base of Livescu and Ristorcelli (2007) from three independent but statistically identical initial conditions (see figure 2.2). This is readily achieved by setting $\omega_s = 0$ in (2.6) and (2.7) and initializing the flow as random blobs of pure fluids in a cube of size $2\pi\ell$, a procedure documented in Livescu and Ristorcelli (2007). There is some statistical spread in the present initial conditions: the initial integral lengthscale $L_\rho/\ell = 0.3542$–0.3550, and the initial density fluctuations $\rho_{rms}/\overline{\rho} = 0.2248$–$0.2252$. Livescu and Ristorcelli (2007) reported these numbers

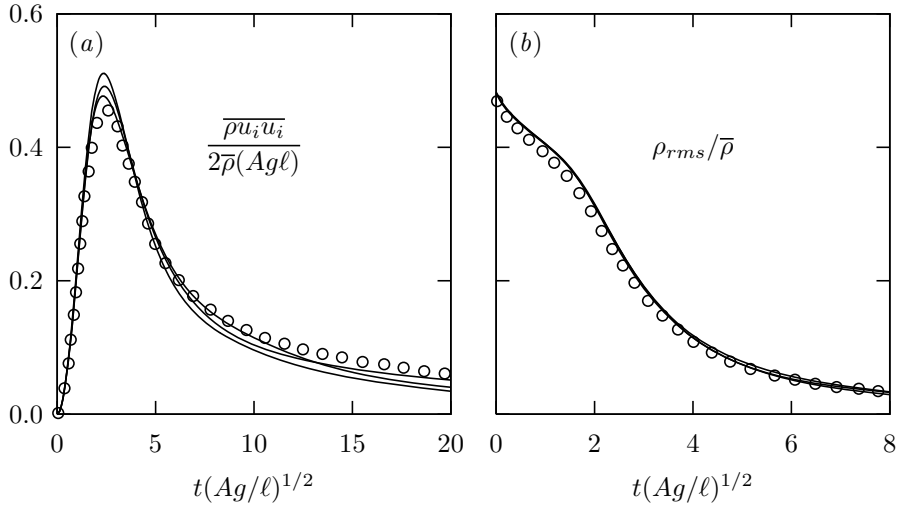

Figure 2.2. The present code shows fair agreement when validated against a simulation performed by Livescu and Ristorcelli (2007) (∘). Three independent but statistically identical simulations are shown (——).

as 0.3525 and 0.22 respectively.

2.4 Results and Discussion

The simulation parameters are given in table 2.1. In each case, the horizontal cross section is a square, $L_x = L_y$. To assess sensitivities to the choice of computational domain we perform the set of cases A, B, and C, which have identical Re and A, but different computational domains: case A in a cube domain $L_z = L_x$, case B in a short domain $L_z = L_x/2$, and case C is a tall domain $L_z = 2L_x$. Cases C, D, E, and F share the same tall domains, but have the four different permutations of $A = \{1/2, 3/4\}$ and $Re = \{(256/2\pi)^{3/2}, (384/2\pi)^{3/2}\} = \{260, 478\}$. The grid Reynolds number $Re_\Delta \equiv \rho_0(Ag\Delta)^{1/2}\Delta/\mu = Re(\Delta/\ell)^{3/2}$ is set to unity; the grid is equidimensional, $\Delta = L_x/N_x = L_y/N_y = L_z/N_z$. Simulations were advanced until volume-averaged statistics appear to reach a statistically stationary state at $t = t_{\text{start}}$. Then all statistics are averaged over T_e eddy-turnover times, defined as

$$T_e \equiv (t_{\text{end}} - t_{\text{start}})(\overline{u_i' u_i'}/3)^{1/2}/L_x,$$

listed in table 2.1. Unless stated otherwise, we will remove time dependence from all statistics to imply time averaging, avoiding cumbersome notation.

Visualizations of the heavy fluid mole fraction are shown in figure 2.3.

Table 2.1. DNS parameters for statistically stationary buoyancy-driven turbulence.

Key	Case	Re	Re_Δ	Sc	A	R	L_x/ℓ	L_y/ℓ	L_z/ℓ	L_f/ℓ	N_x	N_y	N_z	T_e
-·-·-·-	A	260	1	1	1/2	3	2π	2π	2π	$2\pi/10$	256	256	256	5.6
·····	B	260	1	1	1/2	3	4π	4π	2π	$2\pi/10$	512	512	256	3.2
———	C	260	1	1	1/2	3	2π	2π	4π	$2\pi/10$	256	256	512	5.3
— — —	D	260	1	1	3/4	7	2π	2π	4π	$2\pi/10$	256	256	512	8.5
———	E	478	1	1	1/2	3	2π	2π	4π	$2\pi/10$	384	384	768	5.3
— — —	F	478	1	1	3/4	7	2π	2π	4π	$2\pi/10$	384	384	768	4.0

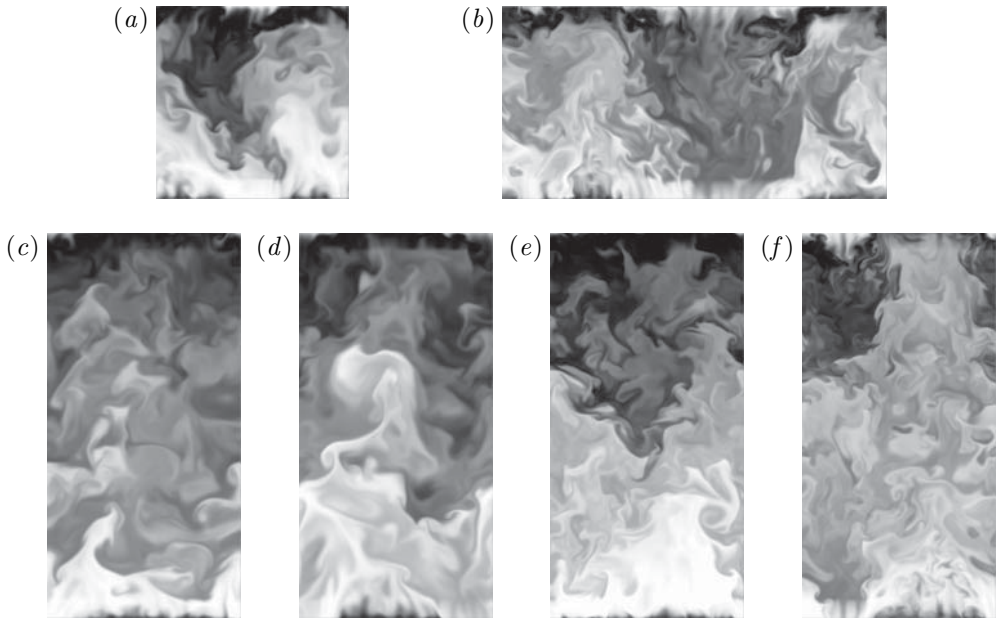

Figure 2.3. Representative xz-plane visualizations of X_2, defined by (2.23). Gravity points downward. The shades vary from light to dark as X_2 vary from 0 to 1. See table 2.1 for simulation parameters. (a) case A, (b) case B, (c) case C, (d) case D, (e) case E, and (f) case F.

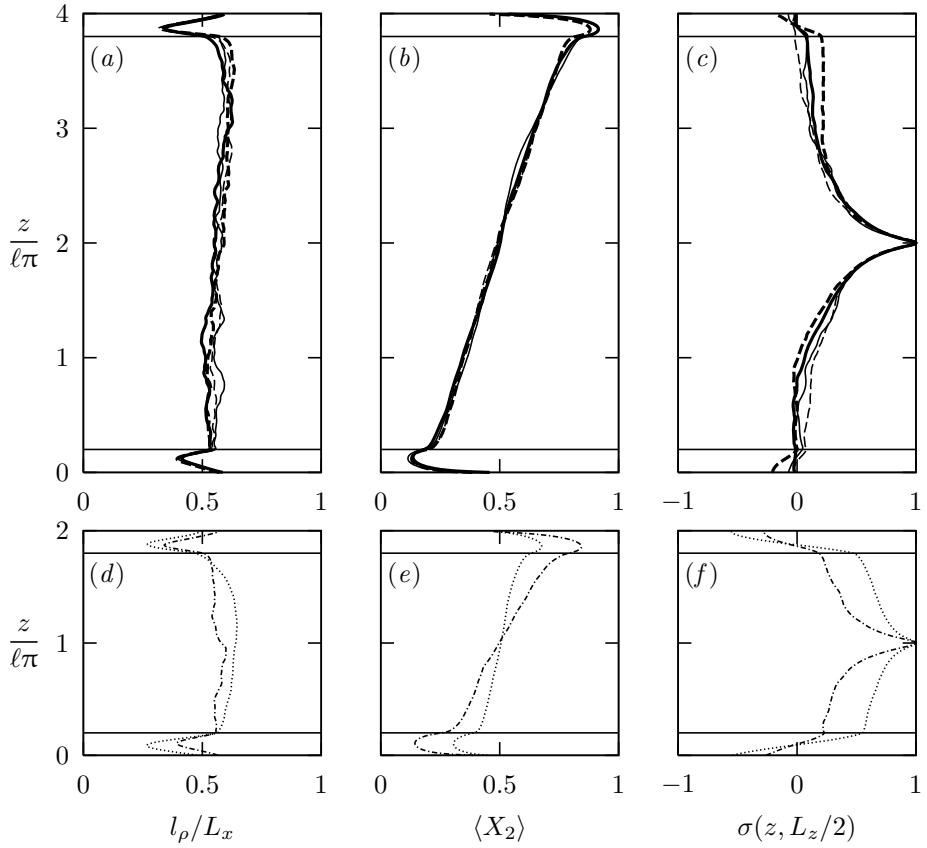

Figure 2.4. Profiles of the integral quantities l_ρ defined by (2.21), X_2 defined by (2.23), and $\sigma(z, L_z/2)$ defined by (2.24) (see table 2.1 for key). Horizontal lines indicate fringe-region boundaries.

2.4.1 Integral and Taylor Statistics

We define the characteristic horizontal wavelength l_ρ and integral lengthscale L_ρ of the density fluctuations at an xy-plane as

$$l_\rho \equiv 2\pi L_\rho \equiv 2\pi \frac{\int_0^\infty E_{\rho\rho}^{2D}(k_r)/k_r \,\mathrm{d}k_r}{\int_0^\infty E_{\rho\rho}^{2D}(k_r)\,\mathrm{d}k_r}, \tag{2.21}$$

where the planar cospectrum $E_{fg}(k_r)$ of the field variables, f and g, is normalized so that

$$\langle f'' g'' \rangle = \int_0^\infty E_{fg}^{2D}(k_r)\,\mathrm{d}k_r, \tag{2.22}$$

where $k_r^2 = k_x^2 + k_y^2$, $f = \langle f \rangle + f''$ and $g = \langle f \rangle + g''$. The characteristic horizontal wavelength is defined in (2.21) so that a delta-function spectrum, $E_{\rho\rho}^{2D} = \delta(k_r - k_\rho)$, would recover the standard definition $l_\rho = 2\pi/k_\rho$. We remark that L_ρ, defined as the integral of the plane-averaged autocorrelation function, differs by a factor of $\pi/2$ to its the volume-averaged counterpart.

Observe from the profile of l_ρ in figure 2.4(a, d) that, regardless of the aspect ratio L_z/L_x used for the computational domain, the characteristic wavelength of eddies (based on density fluctuations) is given by $l_\rho \approx 0.5 L_x$ ($L_\rho \approx 0.08 L_x$). This rules out a statistically stationary simulation that is independent of the horizontal box size, an issue also commonly found in forced homogeneous–isotropic turbulence simulations, where the energy-based integral lengthscale is reported as $\approx 0.15 L_x$ (e.g., Overholt and Pope 1996). This implies that, similar to forced homogeneous–isotropic turbulence simulations, the present simulations should be viewed as a model to study only the small scales of a buoyancy-driven variable-density turbulent mixing.

Since there are no physical lengthscales in our simulations, the existence of box-filling eddies is hardly surprising; this issue is also relevant in Rayleigh–Taylor instability simulations, where, to preserve the physical relevance of results, simulations are typically stopped before the size of the eddies overwhelm the box (Cook, Cabot and Miller 2004).

The heavy-fluid mole fraction is given by

$$X_2(\boldsymbol{x}, t) = \frac{\rho(\boldsymbol{x}, t) - \rho_1}{\rho_2 - \rho_1}. \tag{2.23}$$

The profiles of $\langle X_2 \rangle$ for the tall boxes ($L_z = 2L_x$), but with different Re and A, collapses (figure 2.4(b)), outside the fringe region, onto an approximate line that passes through the point $\langle X_2 \rangle = 0.5$ at $z = L_z/2$. In the upper fringe, $\langle X_2 \rangle < 1$ and, conversely, in the lower fringe, $\langle X_2 \rangle > 0$, implying that the "unmixing" process in the fringe is not complete, a desirable feature if we do not want the flow to relaminarize; a fringe with infinite source rate Λ implies $\langle X_2 \rangle = 0$ for the lower fringe and $\langle X_2 \rangle = 1$ for the upper fringe. The influence of L_z/L_x on the overall slope of $\langle X_2 \rangle$ is evident from

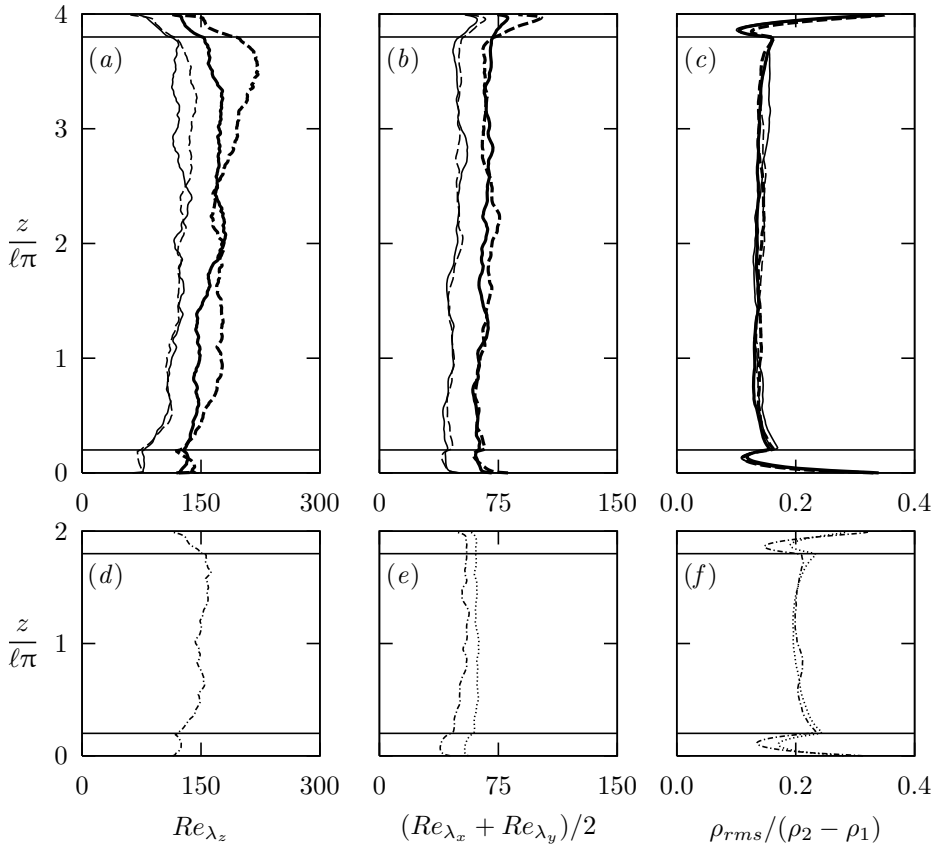

Figure 2.5. Profiles of Taylor-microscale Reynolds numbers, defined by (2.25), and density fluctuation intensities, defined by (2.26) (see table 2.1 for key). Horizontal lines indicate fringe-region boundaries. Case B (·····), for which $Re_{\lambda_z} \approx 600$, is out of the range of (d).

figure 2.4(b, e): a shorter box relative to its width reduces the slope of $\langle X_2 \rangle$.

To check that the the midplane statistics are independent of the fringe region, we plot the density fluctuation autocorrelation $\sigma(z, L_z/2)$, where

$$\sigma(z_1, z_2) = \frac{\langle \rho''(z_1)\rho''(z_2)\rangle}{\langle \rho''(z_1)\rho''(z_1)\rangle^{1/2}\,\langle \rho''(z_2)\rho''(z_2)\rangle^{1/2}}, \tag{2.24}$$

in figure 2.4(c, f). There appears to be some nontrivial fringe-region effects for the shorter boxes, cases A and B.

The Taylor-microscale Reynolds number is defined as

$$Re_{\lambda_\alpha} \equiv \frac{\langle\rho\rangle\lambda_\alpha \left[\left\langle (u''_\alpha)^2 \right\rangle\right]^{1/2}}{\mu}, \quad \text{where} \quad \lambda_\alpha \equiv \left[\frac{\left\langle (u''_\alpha)^2 \right\rangle}{\left\langle (\partial u''_\alpha/\partial x_\alpha)^2 \right\rangle}\right]^{1/2}, \tag{2.25}$$

no summation implied over α. The profiles of the Re_{λ_z} and $Re_{\lambda_{xy}} \equiv (Re_{\lambda_x} + Re_{\lambda_y})/2$, shown in figure 2.5, indicate that, except for case B, $Re_{\lambda_z}/Re_{\lambda_{xy}} \approx$ 2–2.5. Such numbers are also reported

in Cook and Dimotakis (2001), with $Re_{\lambda_z}/Re_{\lambda_{xy}} \approx 2.5$–4, depending on the characteristic scale of the initial conditions. In case B, however, $Re_{\lambda_z}/Re_{\lambda_{xy}} \approx 12$, perhaps owing to the large eddy sizes allowed by the horizontal extent of the computational domain. The general trend that $Re_{\lambda_z}/Re_{\lambda_{xy}}$ is higher with larger eddy sizes is also seen in Cook and Dimotakis (2001).

The root-mean-square (r.m.s.) density fluctuations at a constant-z plane is given by

$$\rho_{rms}(z) = \langle \rho'' \rho'' \rangle^{1/2}. \tag{2.26}$$

Its profiles for the tall boxes, but with different Re and A are plotted in figure 2.5(c). Outside the fringe, the profiles take on roughly constant values, scaling with $(\rho_2 - \rho_1)$, regardless of A. In Cook, Cabot and Miller (2004), an effective Atwood number A_e, defined at the center of the mixing zone as $\rho_{rms}/\langle\rho\rangle$, is shown to approach $0.48A$ at late times. Presently, $\langle\rho\rangle_{z=L_z/2} \approx \rho_0$ for all cases, and so $(A_e/A)_{z=L_z/2} = 2(\rho_{rms})_{z=L_z/2}/(\rho_2 - \rho_1)$, ranging from 0.35 to 0.4, depending on the aspect ratio of the computational domain.

2.4.2 Spectra

The planar spectra, $E^{2D}_{\rho\rho}$, $-E^{2D}_{\rho w}$, E^{2D}_{uu}, and E^{2D}_{vv}, as defined by (2.22), at the midplane location, are plotted in figures 2.6 and 2.7, nondimensionalized by their respective midplane Kolmogorov–Obukhov–Corrsin (KOC) scales: specific kinetic energy dissipation ϵ, density fluctuation dissipation ϵ_ρ and kinematic viscosity ν, which we will define as

$$\epsilon = \nu \left\langle \left(\frac{\partial u_i}{\partial x_j}\right)^2 + \frac{1}{3}\left(\frac{\partial u_i}{\partial x_i}\right)^2 \right\rangle, \quad \epsilon_\rho = \mathcal{D} \left\langle \left(\frac{\partial \rho}{\partial x_j}\right)^2 \right\rangle, \quad \nu = \frac{\mu}{\langle\rho\rangle}, \tag{2.27}$$

whence $\eta = (\nu^3/\epsilon)^{1/4}$. Observe that, when plotted in KOC scaling, all the spectra from the present simulations virtually collapse, especially in the high-wavenumber range, regardless of A, Re, and L_z/L_x. This suggests that, in modeling spectra, the standard scaling ideas (Lumley 1967) used for passive scalar mixing can still be applied to the active scalar mixing problem; in other words, ϵ, ϵ_ρ, and ν are still the relevant scales. Further, these spectra appear to approach the standard power-law scaling with the $-5/3$ exponent for E^{2D}_{ww} and $(E^{2D}_{uu} + E^{2D}_{vv})/2$, and the $-7/3$ exponent for $-E^{2D}_{\rho w}$. Note that the $E^{2D}_{\rho\rho}$ spectra appears to be slightly flatter than a $-5/3$ power law.

For comparison, we also show the 3072^3 DNS spectra from Cabot and Cook (2006) in figures 2.6 and 2.7, normalized by their constant-ν version of (2.27). We also ran a constant-ν, that is $\mu(\boldsymbol{x}, t) = \nu\rho(\boldsymbol{x}, t)$, version of the present flow simulations with no discernible differences in the spectra. The present data allows the comparison of statistically evolving Rayleigh–Taylor spectra relative to statistically stationary flow spectra at the same level of dissipation. When compared to the Rayleigh–Taylor spectra, the present $E^{2D}_{\rho\rho}$ and $-E^{2D}_{\rho w}$ show near collapse but E^{2D}_{ww} and $(E^{2D}_{uu} + E^{2D}_{vv})/2$

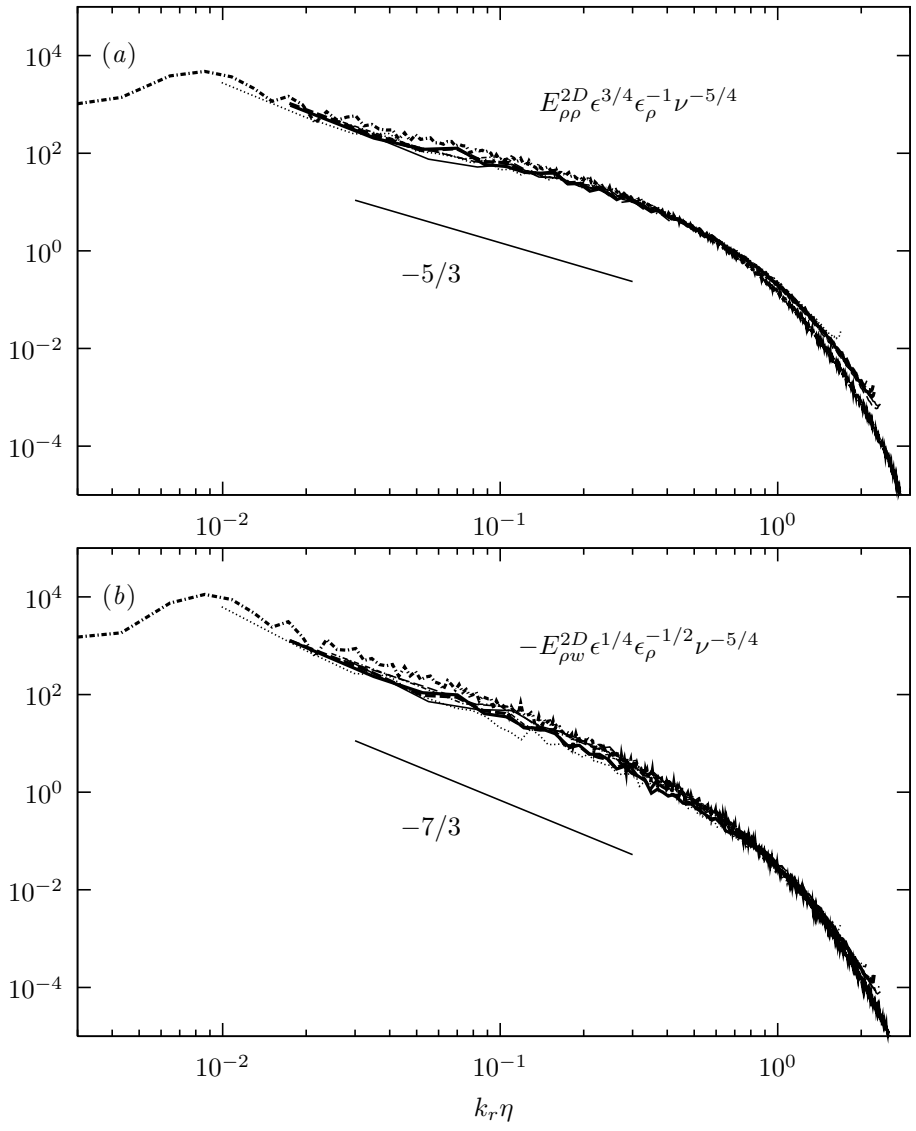

Figure 2.6. Midplane spectra normalized by KOC scales (2.27) of (a) density and (b) density–vertical-velocity: -·-·-·-, 3072^3 DNS of Rayleigh–Taylor instability (Cabot and Cook 2006); remaining lines are from present simulations (see table 2.1 for key).

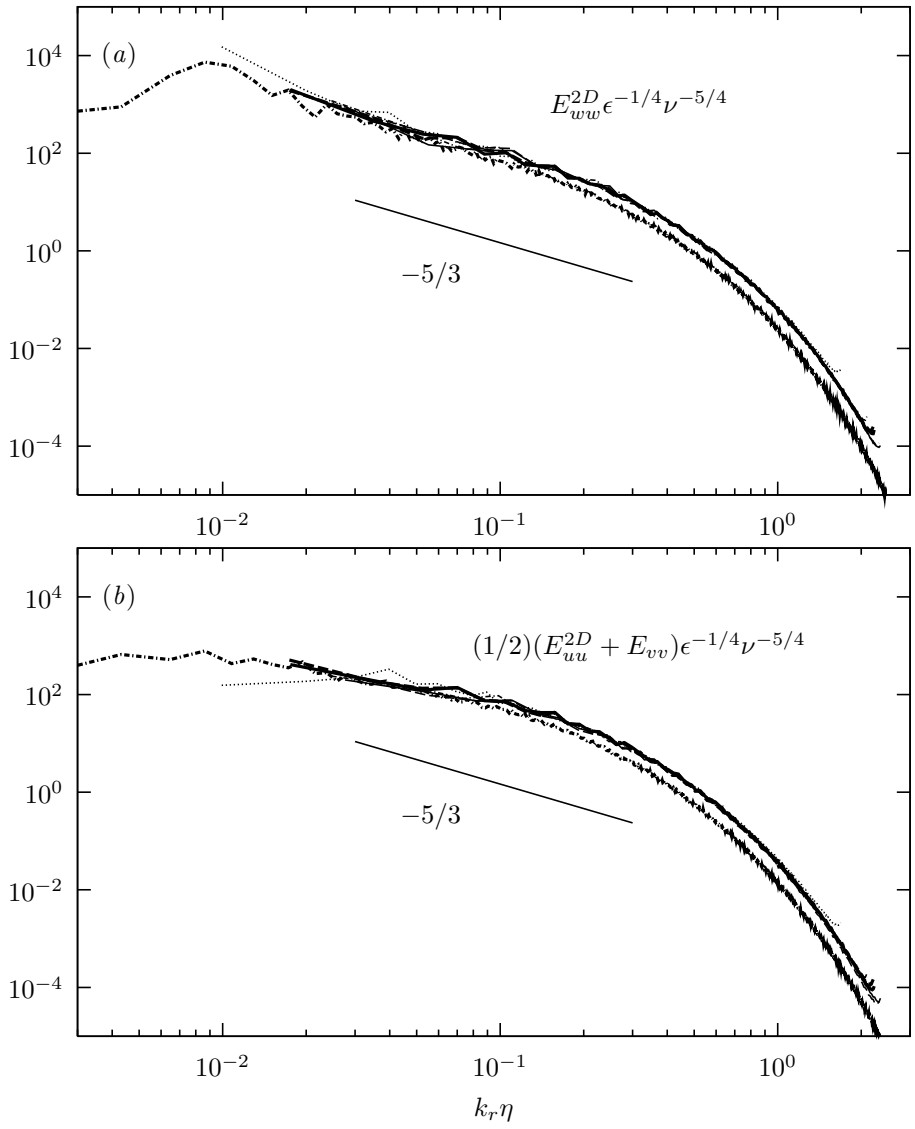

Figure 2.7. Midplane spectra normalized by KOC scales (2.27) of (a) vertical velocity and (b) horizontal velocity: -·-·-·-, 3072^3 DNS of Rayleigh–Taylor instability (Cabot and Cook 2006); remaining lines are from present simulations (see table 2.1 for key).

are slightly higher in the high-wavenumber range. This is perhaps not surprising since turbulence production is greater than dissipation in Rayleigh–Taylor turbulence whereas the present spectra represent "equilibrium" buoyancy-driven turbulence. Even though they do not collapse completely, they share common power-law slopes in the inertial range.

2.4.3 Mole Fraction Probability Density Functions

The probability density functions (p.d.f.) of X_2, shown in figure 2.8, are taken at various vertical locations: the left-most and right-most curves represent the p.d.f.s taken from the middle of the lower and upper fringes, respectively, and the remaining curves are p.d.f.s taken from the quarter-, half-, and three-quarter domain height. Outside the fringe regions, the p.d.f.s are roughly unimodal with peaks varying from 0 to 1. An exception is case B (figure 2.8(b)), which exhibits bimodal behavior, indicating the persistence of unmixed fluids. This can be attributed to the large eddies, permitted by the large horizontal dimensions (figure 2.4(d)), that cause large-scale sloshing motions as unmixed fluids clump together. In contrast, we observe better small-scale mixing when the eddies are smaller (cases A, C–F).

All else equal, the $A = 3/4$ runs (figure 2.8(d, f)) exhibit wider p.d.f.s compared to the $A = 1/2$ runs (figure 2.8(c, e)). We also observe a slight skew toward lower X_2 at the midplane location, seen in figure 2.8(c–f), consistent with the Rayleigh–Taylor turbulence LES performed by Cook, Cabot and Miller (2004) (figure 13).

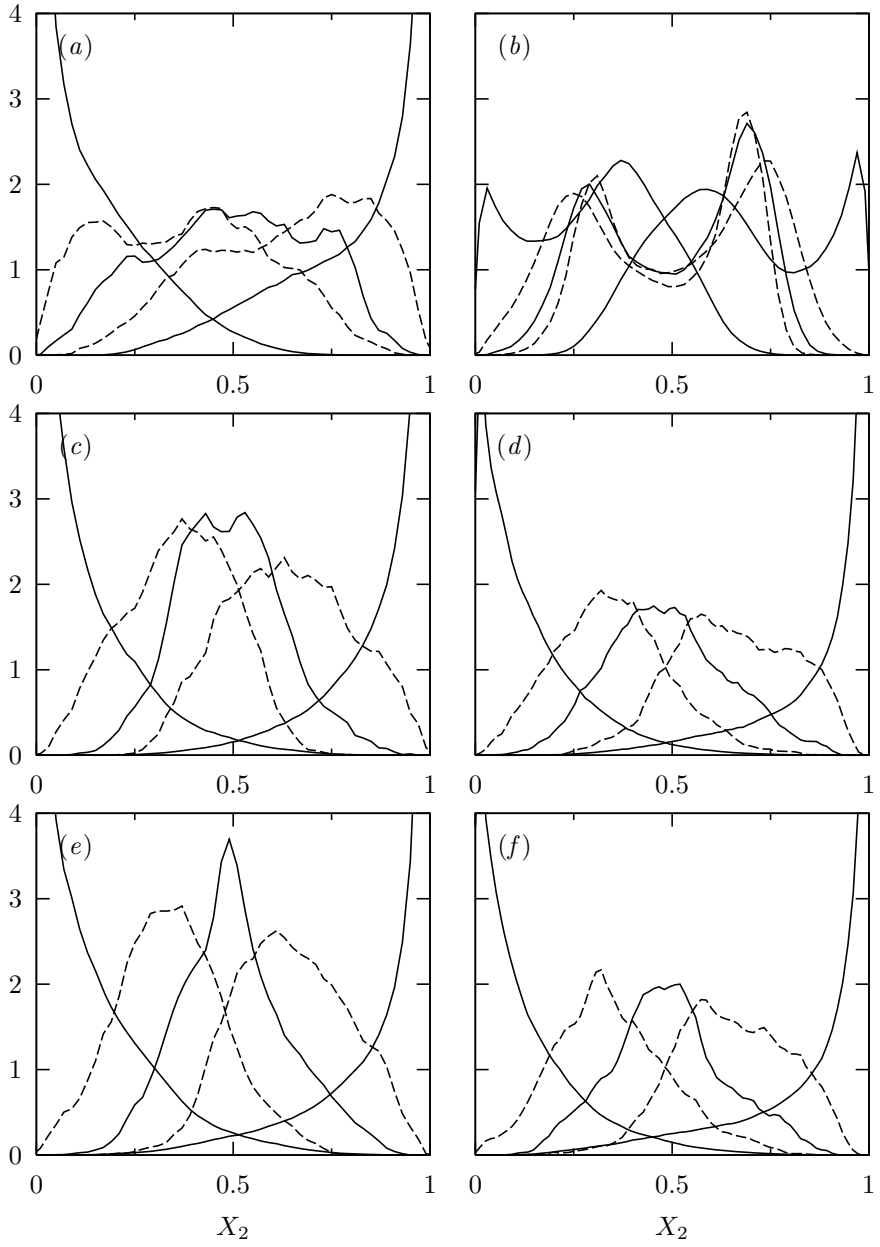

Figure 2.8. P.d.f.s of X_2, defined by (2.23), taken from xy-planes located at, from left to right (alternating between solid and broken lines for legibility), $z = 0.5L_f$, $0.25L_z$, $0.5L_z$, $0.75L_z$, and $L_z - 0.5L_f$. (a) case A, (b) case B, (c) case C, (d) case D, (e) case E and (f) case F.

Chapter 3

LES and SGS Modeling of Active Scalar Mixing Flows

3.1 Background

Originally, researchers (e.g., Pullin 2000, Burton 2008) developed SGS models for turbulent flows in which the scalar is passive. In this chapter, we extend the SGS passive scalar model of Pullin (2000) to handle mildly active (buoyant) scalars. We refer the interested reader to Sagaut (2006) for a review of other SGS active scalar models.

First, we define the relevant scale-dependent nondimensional parameters (see Shih et al. 2005, Ivey et al. 2008):

$$Re_\ell \equiv \frac{U\ell}{\nu}, \quad Ri_\ell \equiv \frac{N^2}{U^2/\ell^2}, \quad I \equiv \frac{\epsilon}{\nu N^2},$$

where N is the Brunt–Väisälä frequency defined by $N^2 = -g(\partial\overline{\rho}/\partial z)$; A is the Atwood number; g is the gravitational acceleration; $\partial\overline{\rho}/\partial z$ is the vertical (opposite to gravity) mean density gradient; ϵ is the viscous dissipation; and U is characteristic velocity at scale ℓ. If we further assume that $\epsilon = U^3/\ell$, we have the following relations:

$$Re_\ell = \left(\frac{\ell}{\eta}\right)^{4/3}, \quad Ri_\ell = \left(\frac{\ell}{L_O}\right)^{4/3}, \quad I = \frac{Re_\ell}{Ri_\ell} = \left(\frac{L_O}{\eta}\right)^{4/3},$$

where $\eta = (\nu^3/\epsilon)^{1/4}$, the Kolmogorov lengthscale and $L_O = (\epsilon/N^3)^{1/2}$, the Ozmidov lengthscale. Eddies smaller than η are strongly dissipated by viscosity, and eddies larger than L_O are strongly suppressed by stratification through conversion to potential energy (Turner 1973). In other words, the unrestrained turbulent eddies have sizes between η and L_O; therefore, $I = (L_O/\eta)^{4/3}$ provides a measure of turbulence activity. Brethouwer et al. (2007) call I the buoyancy Reynolds number.

Figure 3.1 summarizes the three mixing regimes described by Ivey, Winters and Koseff (2008). When $I < 7$, the flow is both strongly stratified and dominated by viscosity—motion is quickly suppressed. As I is increased, the flow first transitions before it becomes fully energetic when

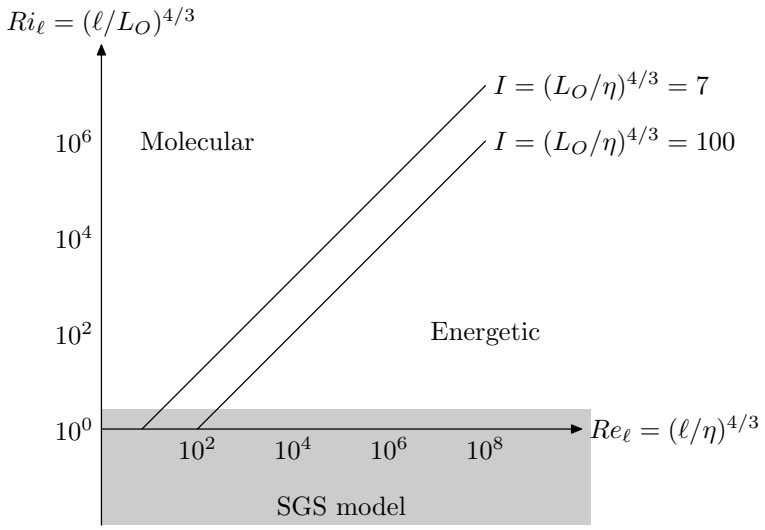

Figure 3.1. Flow regimes in stable stratification characterized by scale-dependent Ri_ℓ and Re_ℓ. Shaded area indicates the operating region for present SGS model extension.

$I > 100$, a process somewhat similar to the mixing transition (Dimotakis 2000). When $Ri_\ell \gg 1$ and $I \gg 1$, the energy spectrum E comprises a buoyancy subrange, $E \sim N^2 k^{-3}$ in $k \ll L_O^{-1}$, and an inertial subrange, $E \sim \epsilon^{2/3} k^{-5/3}$ in $L_O^{-1} \ll k \ll \eta^{-1}$ (Turner 1973). Turbulence in the atmosphere and ocean belong to this energetic regime.

When the flow is unstably stratified (also known as the Rayleigh–Taylor instability), the gradient Richardson number is negative, but its usual meaning—a measure of stratification relative to turbulence production—is undefined since, for stationary–homogeneous flows, buoyancy flux is the only source of turbulent kinetic energy and is therefore equal to the dissipation. In the context of SGS modeling, the effects of buoyancy have already been accounted for once the dissipation, readily determined from matching structure functions at the cutoff scale, is known. In this regime, the usual SGS models of Misra and Pullin (1997), Pullin (2000) are adequate. We demonstrate that this is indeed the case in § 3.2 by performing LES of the unstably stratified flow described in chapter 2.

For stable stratification, we present a new SGS model for the dynamics of the inertial range, $L_O^{-1} \ll k \ll \eta^{-1}$ (shaded region in figure 3.1). In this range, stratification alters the overall turbulent kinetic energy available for mixing and dissipation, but the Richardson cascade, characterized by this altered kinetic energy, is still preserved. In this sense, the scalar is deemed mildly active. To model this effect, we develop a first-order buoyancy correction to the SGS passive scalar flux model of Pullin (2000) in § 3.3. We expect that, using this SGS model, one is able to simulate, with reduced computations, fully developed stratified turbulence by directly simulating the eddies with sizes down to L_O while modeling the eddies with sizes from L_O down to η.

3.2 LES of Unstably Stratified Flow

We perform $32 \times 32 \times 64$, $64 \times 64 \times 128$, and $128 \times 128 \times 256$ LES of the DNS case E (table 2.1), which was run on a $384 \times 384 \times 768$ grid. We refer the reader to chapter 2 for full details of the DNS and flow setup. We only present LES-specific details in this chapter.

3.2.1 Filtered LES Equations and SGS Model

Following Mattner, Pullin and Dimotakis (2004), Hill, Pantano and Pullin (2006), we filter the governing equations in the form (2.1), (2.2) and (2.3), and then rearrange them using

$$1/\overline{\rho} = \widetilde{Y}_1/\rho_1 + (1 - \widetilde{Y}_1)/\rho_2 \tag{3.1}$$

to obtain:

$$\frac{\partial \widetilde{u}_j}{\partial x_j} = -\mathcal{D}\frac{\partial^2 s}{\partial x_j^2} + \frac{\partial q_j^s}{\partial x_j} - \omega_s, \tag{3.2a}$$

$$\frac{\partial s}{\partial t} + \widetilde{u}_j \frac{\partial s}{\partial x_j} = \mathcal{D}\frac{\partial^2 s}{\partial x_j^2} - \frac{\partial q_j^s}{\partial x_j} + \omega_s, \tag{3.2b}$$

$$\frac{\partial \widetilde{u}_i}{\partial t} + \widetilde{u}_j \frac{\partial \widetilde{u}_i}{\partial x_j} = -\frac{1}{\overline{\rho}}\left(\frac{\partial \overline{p}}{\partial x_i} + \Gamma_i\right) + \frac{1}{\overline{\rho}}\frac{\partial \tau_{ij}}{\partial x_j} - \frac{1}{\overline{\rho}}\frac{\partial \overline{\rho} T_{ij}}{\partial x_j} - g\delta_{i3}, \tag{3.2c}$$

where $s \equiv \log(\overline{\rho}/\rho_0)$. Given a field $\phi(\boldsymbol{x})$, we define its Favre-average by $\widetilde{\phi} \equiv \overline{\rho\phi}/\overline{\rho}$; this, in turn, is defined by the LES filter associated with cutoff scale Δ_c,

$$\overline{\phi}(\boldsymbol{x}) = \int G(\boldsymbol{x} - \boldsymbol{x}'; \Delta_c)\phi(\boldsymbol{x}')\,\mathrm{d}\boldsymbol{x}'.$$

The subgrid stress tensor is given by (Misra and Pullin 1997)

$$T_{ij} = (\delta_{ij} - e_i^v e_j^v)K, \tag{3.3}$$

and we choose the subgrid vortex to align with the most extensive eigenvector of the strain-rate tensor, $\boldsymbol{e}^v = \boldsymbol{e}_{\widetilde{S}}$. K is the subgrid (specific) kinetic energy, given by

$$K = \int_{k_c}^{\infty} E(\kappa)\,\mathrm{d}\kappa, \tag{3.4}$$

where $k_c \equiv \pi/\Delta_c$ and $\Delta_c = \Delta_x = \Delta_y = \Delta_z$. The energy spectrum of a spiral vortex is

$$E(\kappa) = \mathcal{K}_0 \epsilon^{2/3}\kappa^{-5/3} \exp\left[-\kappa^2\lambda_v^2\right], \tag{3.5}$$

where $\lambda_v^2 = 2\widetilde{\nu}/(3|\widetilde{a}|)$; $\widetilde{\nu} = \mu/\overline{\rho}$; and $\widetilde{a} = e_i^v e_j^v \widetilde{S}_{ij}$, so that

$$K = \frac{1}{2}\mathcal{K}_0'\Gamma[-1/3, k_c^2\lambda_v^2], \quad \text{where} \quad \mathcal{K}_0' = \mathcal{K}_0\epsilon^{2/3}\lambda_v^{2/3}. \tag{3.6}$$

We determine $\mathcal{K}_0'$ by matching an expression for the SGS model structure function with its observed value computed from the resolved part of the LES simulation (Pullin 2000, Voelkl, Pullin and Chan 2000, Hill, Pantano and Pullin 2006).

Since the filter is applied to the Y_1 equation, (2.1), we model its (specific) flux as if it were a passive scalar (Pullin 2000, Hill, Pantano and Pullin 2006):

$$q_i^{Y_1} \equiv \widetilde{Y_1 u_i} - \widetilde{Y_1}\widetilde{u}_i = -\gamma_{Y_1}\frac{\Delta_c}{2}K^{1/2}(\delta_{ij} - e_i^v e_j^v)\frac{\partial \widetilde{Y}_1}{\partial x_j}; \tag{3.7}$$

presently, $\gamma_{Y_1} = 1$. Upon substituting (3.1) into (3.7) and comparing the result with both the filtered form of (2.1) and (3.2 b), we find that

$$q_i^s \equiv \widetilde{u}_i - \overline{u}_i \equiv -\left(\frac{1}{\rho_1} - \frac{1}{\rho_2}\right)\overline{\rho} q_i^{Y_1} = -\gamma_{Y_1}\frac{\Delta_c}{2}K^{1/2}(\delta_{ij} - e_i^v e_j^v)\frac{\partial s}{\partial x_j}.$$

We can rearrange this to relate the subgrid mass flux, $\overline{\rho u_i}$, to the resolved density gradient, $\partial\overline{\rho}/\partial x_i$:

$$\overline{\rho u_i} - \overline{\rho}\,\overline{u}_i = -\gamma_{Y_1}\frac{\Delta_c}{2}K^{1/2}(\delta_{ij} - e_i^v e_j^v)\frac{\partial \overline{\rho}}{\partial x_j}. \tag{3.8}$$

By definition, the above quantity is equal to $\int_{k_c}^{\infty} E_{\rho u_i}(\kappa; \boldsymbol{e}^v)\,\mathrm{d}\kappa$, where $E_{\rho u_i}$ is the ρ–u_i cospectrum of the two-dimensional flow in the $\boldsymbol{e}^v$-oriented vortex cross section. After substituting (3.4) and (3.5) into (3.8), we solve for $E_{\rho u_i}$ to get

$$E_{\rho u_i}(\kappa; \boldsymbol{e}^v) = -\gamma_{Y_1}(2/3)^{1/2}\pi(\mathcal{K}_0')^{1/2}\lambda_v^2 F(\kappa\lambda_v)(\delta_{ij} - e_i^v e_j^v)\frac{\partial \overline{\rho}}{\partial x_j}, \tag{3.9}$$

where

$$F(\kappa_v) = \frac{\sqrt{3}}{4}\kappa_v^{-7/3}\frac{(\mathrm{e}^{-\kappa_v^2} + \kappa_v^{2/3}\Gamma[-1/3, \kappa_v^2])}{(\kappa_v^{2/3}\Gamma[-1/3, \kappa_v^2])^{1/2}}.$$

In the inertial range ($\kappa_v \to 0$), $F \sim \kappa_v^{-7/3}$. Equation (3.9) is consistent with the well-known result obtained from scaling arguments (e.g., Lumley 1967, Saddoughi and Veeravalli 1994) that $E_{\rho u}(\kappa) \sim -(\partial\overline{\rho}/\partial x)\epsilon^{1/3}\kappa^{-7/3}$.

3.2.2 Subgrid Extensions of Planar Spectra

Assuming that the subgrid vortices are aligned according to delta-function p.d.f.s with peaks at

$$\boldsymbol{e}^v(\boldsymbol{x}) = (\sin\alpha_0\cos\beta_0, \sin\alpha_0\sin\beta_0, \cos\alpha_0),$$

we use the following expressions, given by Hill, Pantano and Pullin (2006) (equations (6.11) and (6.12)), to obtain xy-plane velocity spectra from the vortex spectrum (see also Pullin and Saffman 1994):

$$E_{qq}^{2D}(k_r) = \frac{2k_r}{\pi}\int_{k_r}^{|k_r/\cos\alpha_0|} \frac{E(\kappa)}{(\kappa^2-k_r^2)^{1/2}(k_r^2-\kappa^2\cos^2\alpha_0)^{1/2}}\,\mathrm{d}\kappa, \tag{3.10a}$$

$$E_{33}^{2D}(k_r) = \frac{2k_r}{\pi}\int_{k_r}^{|k_r/\cos\alpha_0|} \frac{(k_r^2-\kappa^2\cos^2\alpha_0)^{1/2}E(\kappa)}{\kappa^2(\kappa^2-k_r^2)^{1/2}}\,\mathrm{d}\kappa, \tag{3.10b}$$

where $k_r = (k_x^2+k_y^2)^{1/2}$, the radial wavenumber; and $E(\kappa)$ is given by (3.5). In the present notation, $(E_{uu}^{2D}+E_{vv}^{2D})/2 = E_{qq}^{2D} - E_{33}^{2D}$ and $E_{ww}^{2D} = 2E_{33}^{2D}$. A similar expression can be found for the planar ρ–u_i cospectrum (see appendix A):

$$E_{\rho u_i}^{2D}(k_r) = \frac{2k_r}{\pi}\int_{k_r}^{|k_r/\cos\alpha_0|} \frac{E_{\rho u_i}(\kappa;\boldsymbol{e}^v)}{(\kappa^2-k_r^2)^{1/2}(k_r^2-\kappa^2\cos^2\alpha_0)^{1/2}}\,\mathrm{d}\kappa, \tag{3.11}$$

where $E_{\rho u_i}(\kappa;\boldsymbol{e}^v)$ is given by (3.9). Given k_r and z, we average (3.10) and (3.11) across the xy-plane to obtain subgrid extensions of planar spectra.

We plot in figure 3.2 the midplane ($z = L_z/2$) resolved-scale spectra and their subgrid extensions, normalized by $\nu \equiv \mu/\langle\overline{\rho}\rangle$ and $\epsilon' \equiv \langle\widetilde{S}_{ij}\tau_{ij} - \overline{\rho}\widetilde{S}_{ij}T_{ij}\rangle/\langle\overline{\rho}\rangle$, where $\langle\ \rangle$ denotes the xy-plane average. The LES spectra are in general agreement with their DNS counterparts, also shown in figure 3.2. However, the subgrid extensions show noticeable resolution dependence at the viscous rolloff. This can be understood as follows: the viscous rolloff is determined by the factor $\exp[-2\widetilde{\nu}\kappa^2/(3|\widetilde{a}|)]$ in the model energy spectrum, (3.5), but the local strain rate $\widetilde{a}$ is itself an LES resolution-dependent quantity. Since we expect that the energy transfer off the resolved-scale grid to subgrid scales will, in general, depend on the LES-resolution, then this approximation is acceptable and necessary for integrating the resolved-scale variables in time. For the purposes of subgrid extension, however, a different approximation is appropriate.

Following Lundgren (1982), we estimate that $\widetilde{a} = (\widetilde{\epsilon}/(15\widetilde{\nu}))^{1/2}$, where $\widetilde{\epsilon}$ is the local cell-averaged dissipation rate to be determined. With this estimate, the viscous rolloff is now characterized by the resolution-independent factor $\exp[-(1.61\widetilde{\eta})^2\kappa^2]$ in (3.5), where $\widetilde{\eta} = (\widetilde{\nu}^3/\widetilde{\epsilon})^{1/4}$. To determine $\widetilde{\epsilon}$, we solve the following transcendental equation, obtained from (3.3), (3.6), and the definitions of $\widetilde{\epsilon}$

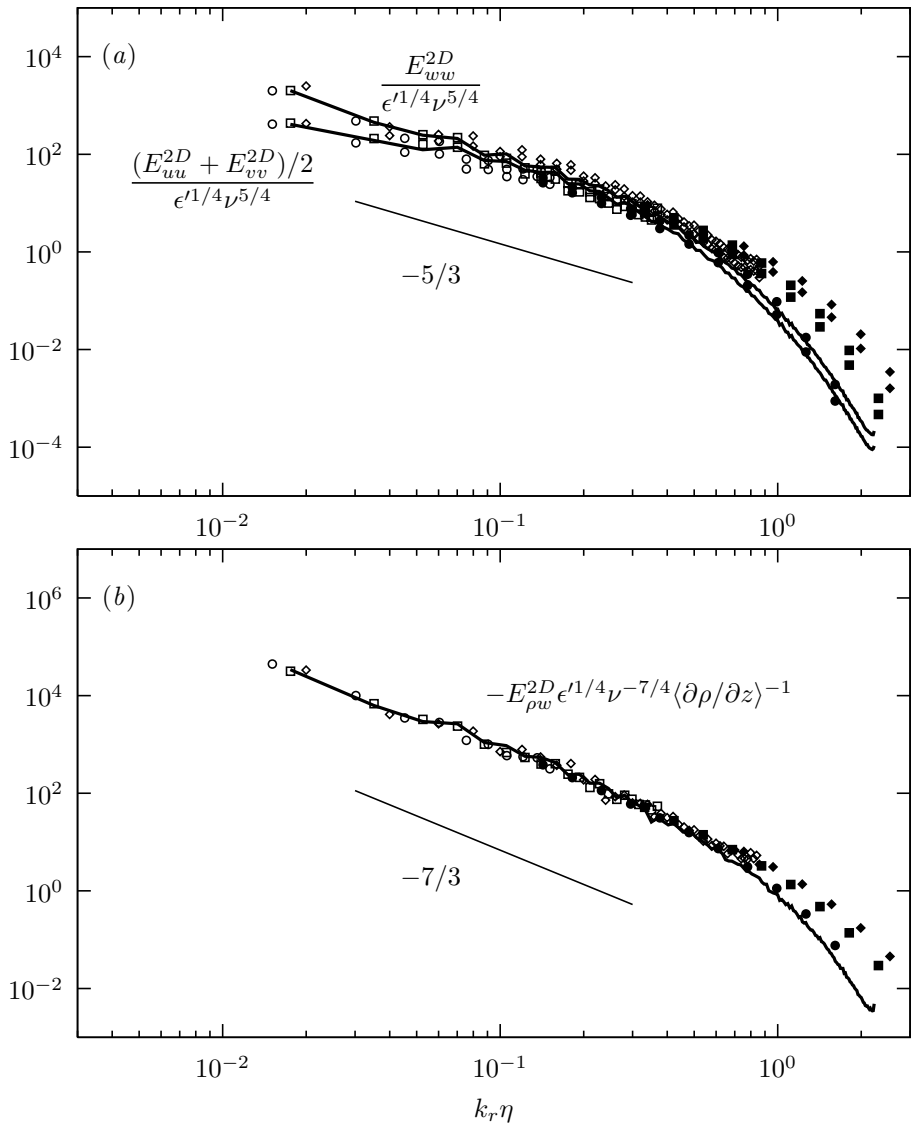

Figure 3.2. LES and DNS comparisons of (a) midplane vertical-velocity spectra and horizontal-velocity spectra and (b) midplane density–vertical-velocity cospectra: ○ , $32 \times 32 \times 64$ LES; □ , $64 \times 64 \times 128$ LES; ◇ , $128 \times 128 \times 256$ LES; open symbols, resolved; solid symbols, subgrid; ——— , $384 \times 384 \times 768$ DNS (case E from table 2.1).

and $\widetilde{\eta}$:

$$\left.\begin{aligned}\widetilde{\epsilon} &= \widetilde{S}_{ij}\tau_{ij}/\overline{\rho} - \widetilde{S}_{ij}(\delta_{ij} - e_i^v e_j^v)\frac{1}{2}A(1.61\widetilde{\eta})^{2/3}\Gamma[-1/3, (1.61\widetilde{\eta})^2 k_c^2], \\ \widetilde{\eta} &= (\widetilde{\nu}^3/\widetilde{\epsilon})^{1/4},\end{aligned}\right\} \tag{3.12}$$

where A is the inseparable group prefactor $\mathcal{K}_0\epsilon^{2/3}$ determined from the structure function matching procedure. Equation (3.12), analogous to (37) in Pullin and Saffman (1993), merely states that the local cell-averaged dissipation comprises the resolved and subgrid components. Having determined $\widetilde{\epsilon}$, we can then calculate the subgrid extensions as before but replacing $\lambda_v = 1.61\widetilde{\eta}$ in both (3.5) and (3.9).

We replot in figure 3.3(a) the midplane resolved-scale velocity spectra and their subgrid extensions, now normalized by ν and ϵ, where $\nu \equiv \mu/\langle\overline{\rho}\rangle$ as before, but now $\epsilon = \langle\widetilde{\epsilon}\rangle$, different from ϵ'. The general features of the LES spectra are in fair agreement with their DNS counterparts. However, LES slightly underpredicts both the vertical-velocity spectrum, E_{ww}^{2D}, and the horizontal-velocity spectrum, $(E_{uu}^{2D} + E_{vv}^{2D})/2$, at around $k_r\eta = 10^{-1}$. Observe that the improved subgrid extensions now collapse. The ρ–w cospectra, normalized by ν, ϵ, and $\langle\partial\rho/\partial z\rangle$, are shown in figure 3.3(b). The resolved part of the LES cospectra agree well with DNS and their subgrid extensions accurately capture the shape and location of the viscous rolloff, independent of the LES resolution. We remark that in the subgrid estimation, $\widetilde{\epsilon}$ is to be viewed as a random variable whose planar/timewise p.d.f. is determined by the LES itself. Pullin and Saffman (1993) argue that the effect of statistical variation of the effective strain can change the $-\kappa^2$ factor within the exponential of the Lundgren spectrum to $-\kappa$, as is observed in experiment and DNS. This effect can be seen in the present subgrid-scale extension, figure 3.4, a result that compares well with the high-Re experiments of Saddoughi and Veeravalli (1994), in which it was reported that $E(k) \propto \exp(-5.2k\eta)$ in the range $0.5 < k\eta < 3$.

Plotting the velocity-anisotropy parameter $E_{ww}^{2D}/E_{u_iu_i}^{2D} - 1/3$ in figure 3.5(a), we observe that the present LES captures the small-scale anisotropy observed in DNS. In particular, the decreasing anisotropy from low wavenumbers up to $k_r\eta = 10^{-1}$, followed by a gradually increasing anisotropy up to $k_r\eta = 2$ is reported by both DNS and LES. For the LES, the location of the minimum is independent of the LES resolution. It appears from figure 3.5(a) that the anisotropy increases indefinitely, albeit gradually, with increasing wavenumber. We superimpose the high-resolution Rayleigh–Taylor DNS velocity-anisotropy parameter from Cabot and Cook (2006) in figure 3.5(b) to see that the anisotropy eventually decreases after reaching a local maximum of about 0.18 at $k_r\eta = 2$.

That the anisotropy increases with wavenumber is perhaps counterintuitive, and perhaps contradictory to the notion of small-scale isotropy. We remark that Cabot and Cook (2006) measured small-scale anisotropy by comparing the relative magnitudes of directional Kolmogorov microscales, defined by $\eta_i = (\nu^3/\epsilon_i)^{1/4}$, $\epsilon_i = 15\nu\langle(\partial u_i/\partial x_i)^2\rangle$ (no summation), and found that, with this measure, the small scales were isotropic. A question then arises as to why the velocity-anisotropy parameter

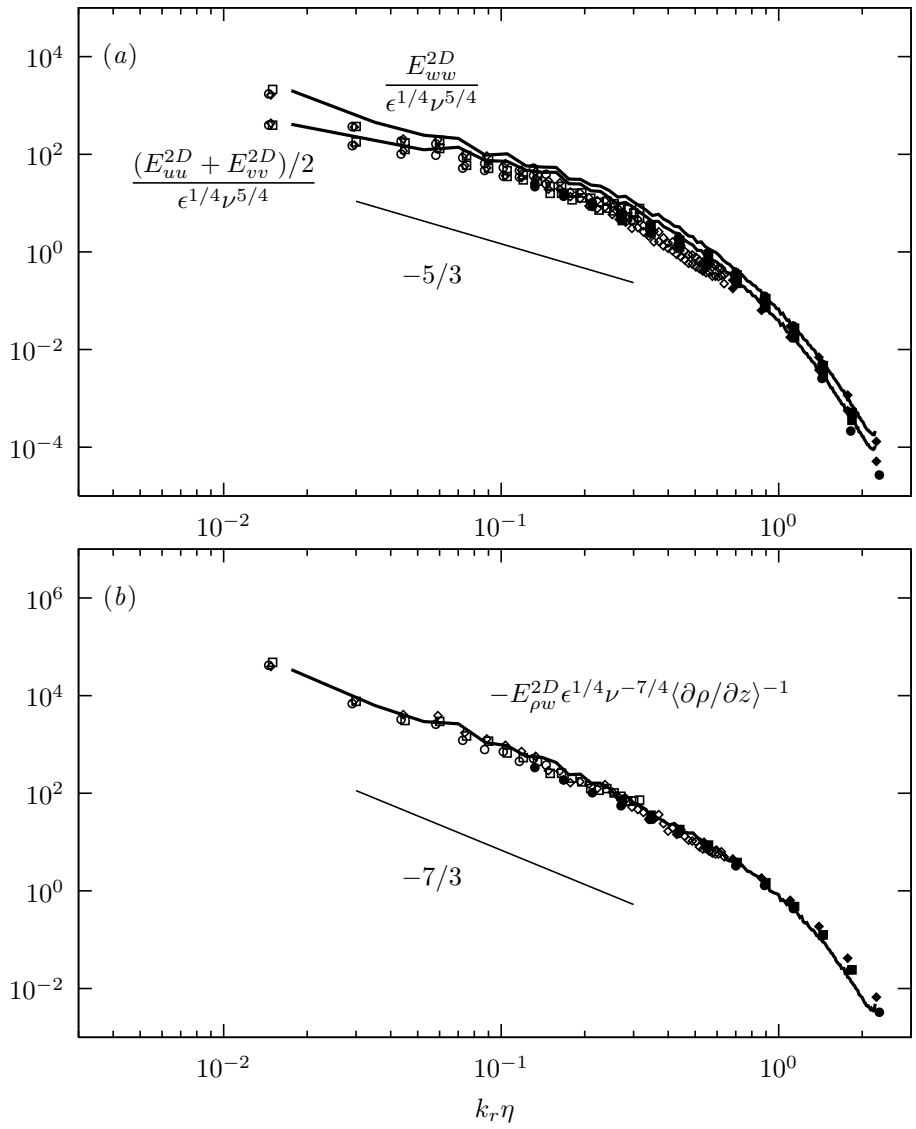

Figure 3.3. Improved subgrid extensions in LES and DNS comparisons of (a) midplane vertical-velocity spectra and horizontal-velocity spectra and (b) midplane density–vertical-velocity cospectra: ○ , $32 \times 32 \times 64$ LES; □ , $64 \times 64 \times 128$ LES; ◇ , $128 \times 128 \times 256$ LES; open symbols, resolved; solid symbols, subgrid; ——— , $384 \times 384 \times 768$ DNS (case E from table 2.1).

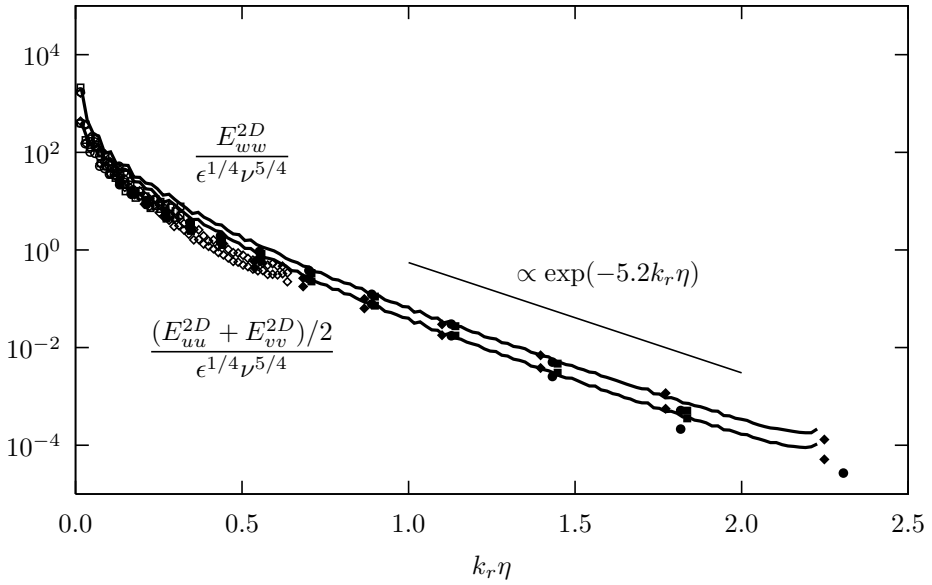

Figure 3.4. LES and DNS comparisons of midplane velocity spectra in log–linear coordinates: ∘ , $32 \times 32 \times 64$ LES; ▫ , $64 \times 64 \times 128$ LES; ◇ , $128 \times 128 \times 256$ LES; open symbols, resolved; solid symbols, subgrid; ——— , $384 \times 384 \times 768$ DNS (case E from table 2.1).

increases in the viscosity-dominated range $10^{-1} < k_r\eta < 2$. Since all components of velocity fluctuations are decreasing in this range (figure 3.3*a*), the anisotropy can only increase if the horizontal velocity fluctuations decrease faster than the vertical velocity fluctuations. This is somewhat similar to the late-time viscosity-dominated characteristics of decaying homogeneous buoyancy-driven turbulence (Batchelor, Canuto and Chasnov 1992, Livescu and Ristorcelli 2007, 2008), where the anisotropy measured by $w^2_{rms}/(u^2_{rms} + v^2_{rms} + w^2_{rms}) - 1/3$ is reported to be in the range 0.21–0.25 (Batchelor, Canuto and Chasnov 1992) and 0.22–0.3 (Livescu and Ristorcelli 2007). Livescu and Ristorcelli (2008) (figure 21) also reported a minimum in a related but different anisotropy parameter from DNS of decaying buoyancy-driven turbulence.

The fair agreement between DNS and the present LES suggests that a special SGS model for active scalars is not needed for unstably stratified flows; a passive scalar SGS model is sufficient. This can be explained as follows: modeling each LES cell as a unit of stationary–homogeneous unstably stratified turbulence, we find that the subgrid buoyancy flux in each cell is equal to the its subgrid dissipation, but, since the subgrid dissipation is already accounted for in a passive scalar SGS model (by matching structure functions at the cutoff scale), we have also indirectly accounted for the subgrid buoyancy flux. In broad terms, unstable stratification does not disrupt the classical picture of turbulent mixing embodied in the Richardson cascade.

The present LES is far cheaper to run. The DNS (case E in table 2.1) requires 400 hours of computing time on 64 processors to collect statistics over 5 eddy-turnover times. By contrast, the $32 \times 32 \times 64$ LES only requires 1 hour of computing time on 4 of the same processors to collect

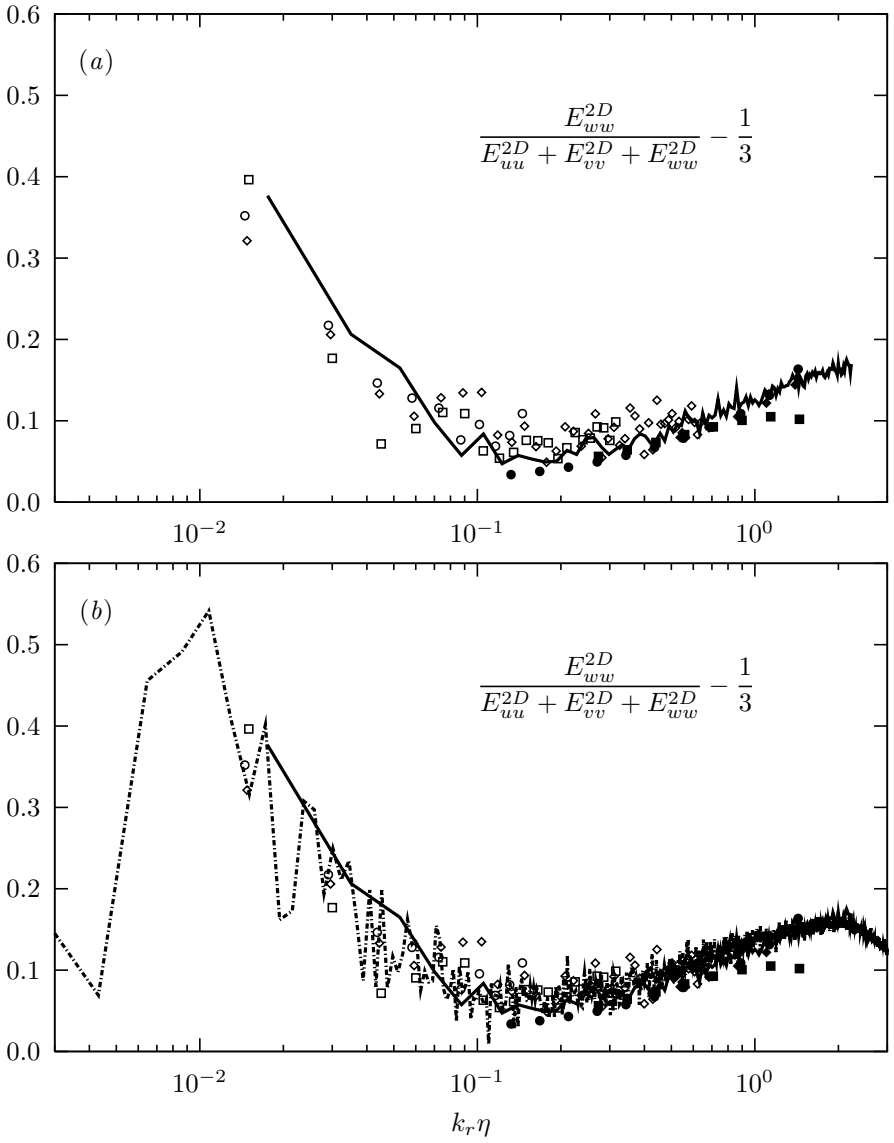

Figure 3.5. LES and DNS comparisons of the midplane velocity-anisotropy parameter: ○ , $32\times32\times64$ LES; □ , $64\times64\times128$ LES; ◇ , $128\times128\times256$ LES; open symbols, resolved; solid symbols, subgrid; ——— , $384\times384\times768$ DNS (case E from table 2.1); -·-·-·-, 3072^3 DNS of Rayleigh–Taylor instability (Cabot and Cook 2006).

statistics over 23 eddy-turnover times. In terms of processor-hours per 10 eddy-turnover times, this represents savings by a factor in excess of 10^5.

3.3 SGS Model for Stably Stratified Flows

The development of the SGS model for active scalar flux in a stably stratified flow is organized as follows. In § 3.3.1, we introduce the vortex-based model for active scalar dynamics by invoking assumptions similar to that used by Pullin (2000). We then perform a perturbation expansion for small Richardson numbers (mildly active scalar) of the model equations in § 3.3.2. The solution to the perturbation equations was then used to calculate the Ri-dependent corrections to the SGS kinetic energy (§ 3.3.3) and SGS scalar flux (§ 3.3.4). Finally, we use the DNS data of chapter 2 to perform an *a posteriori* testing of the new active scalar SGS model in § 3.3.5.

3.3.1 Vortex-Based SGS Model for Active Scalar Dynamics

To simplify the analysis, we will use the Boussinesq approximation of the governing equations. First, expand the flow variables in small Atwood number A,

$$s = As^{(1)} + O(A^2), \quad u_i = u_i^{(0)} + O(A), \quad p = p^{(0)} + O(A),$$

and then substitute these expansions into the governing equations, (2.6), (2.7), and (2.16), omitting the source term ω_s. Collecting leading-order terms while maintaining $Ag = O(1)$ gives the Boussinesq form of the governing equations:

$$\left.\begin{aligned} \frac{\partial s^{(1)}}{\partial t} + u_j^{(0)}\frac{\partial s^{(1)}}{\partial x_j} &= \mathcal{D}\frac{\partial^2 s^{(1)}}{\partial x_j^2}, \\ \frac{\partial u_j^{(0)}}{\partial x_j} &= 0, \\ \frac{\partial u_i^{(0)}}{\partial t} + u_j^{(0)}\frac{\partial u_i^{(0)}}{\partial x_j} &= -\frac{\partial P}{\partial x_i} + \nu\frac{\partial^2 u_j^{(0)}}{\partial x_j^2} - Ags^{(1)}\delta_{i3}, \end{aligned}\right\} \tag{3.13}$$

where $\nu = \mu/\rho_0$, $P = (p^{(0)} + \rho_0 g x_3)/\rho_0$. We will henceforth drop the cumbersome superscripts, and rename $As^{(1)} \to c$. Taking the curl of the momentum equation in (3.13), we obtain the vorticity equation that contains a buoyancy source (or sink):

$$\frac{\partial \omega_i}{\partial t} + u_j\frac{\partial \omega_i}{\partial x_j} = \omega_j\frac{\partial u_i}{\partial x_j} + \nu\frac{\partial^2 \omega_i}{\partial x_j^2} - g\epsilon_{ij3}\frac{\partial c}{\partial x_j}. \tag{3.14}$$

Following the simplified analysis of Pullin (2000), we model the SGS dynamics of a turbulent flow fields as an ensemble of idealized flows, each of which is a two-dimensional two-component (xy-plane)

inviscid vortex ($\nu = 0$) in an immiscible ($\mathcal{D} = 0$) fluid. In addition, these flows are now subjected to gravity, which now, without loss of generality, points in the $-y$ direction of the vortex frame. In polar coordinates, the governing equations for the active scalar $c(r, \theta, t)$, out-of-plane vorticity $\omega(r, \theta, t)$, and streamfunction $\psi(r, \theta, t)$ are

$$\left.\begin{aligned} \frac{\partial c}{\partial t} + \frac{1}{r}\left(\frac{\partial \psi}{\partial \theta}\frac{\partial c}{\partial r} - \frac{\partial c}{\partial \theta}\frac{\partial \psi}{\partial r}\right) &= 0, \\ \frac{\partial \omega}{\partial t} + \frac{1}{r}\left(\frac{\partial \psi}{\partial \theta}\frac{\partial \omega}{\partial r} - \frac{\partial \omega}{\partial \theta}\frac{\partial \psi}{\partial r}\right) &= -g\left(\frac{\partial c}{\partial r}\cos\theta - \frac{1}{r}\frac{\partial c}{\partial \theta}\sin\theta\right), \\ \omega &= -\left(\frac{1}{r}\frac{\partial}{\partial r}r\frac{\partial}{\partial r} + \frac{1}{r^2}\frac{\partial^2}{\partial \theta^2}\right)\psi, \end{aligned}\right\} \tag{3.15}$$

with initial conditions

$$\left.\begin{aligned} c(r, \theta, 0) &= \frac{\partial \widetilde{c}}{\partial x} r\cos\theta + \frac{\partial \widetilde{c}}{\partial y} r\sin\theta, \\ \omega(r, \theta, 0) &= \frac{1}{r}\frac{\mathrm{d}}{\mathrm{d}r} r^2 \Omega(r). \end{aligned}\right\} \tag{3.16}$$

where $x = r\cos\theta$ and $y = r\sin\theta$. $\Omega(r)$, $\partial\widetilde{c}/\partial x$, and $\partial\widetilde{c}/\partial y$ characterize the resolved vorticity and the resolved scalar gradient. This simplified vortex model now incorporates the buoyancy source—compare (3.14) and (3.15).

The relevant nondimensional parameter in this problem is the Richardson number

$$Ri \equiv \frac{-g(\partial\widetilde{c}/\partial y)}{1/T^2}, \tag{3.17}$$

where T is the eddy-turnover time of the subgrid vortex described by Ω. When the flow is stably stratified, $Ri > 0$.

3.3.2 Perturbation Expansion of Mildly Active Scalar Equations

Now, consider the case when the scalar is mildly active, $|Ri| \ll 1$. This occurs when the size of the vortex is small relative to the Ozmidov scale L_O. We can then perform a regular perturbation expansion in small Ri, or equivalently, small g, in which case, g is understood to be small relative to $(\partial\widetilde{c}/\partial y)^{-1}T^{-2}$:

$$c = c^{(0)} + gc^{(1)} + O(g^2), \quad \omega = \omega^{(0)} + g\omega^{(1)} + O(g^2), \quad \psi = \psi^{(0)} + g\psi^{(1)} + O(g^2). \tag{3.18}$$

Substituting (3.18) into (3.15) and (3.16), then collecting $O(g^0)$ terms, we obtain

$$\left.\begin{aligned}
\frac{\partial c^{(0)}}{\partial t} + \frac{1}{r}\left(\frac{\partial \psi^{(0)}}{\partial \theta}\frac{\partial c^{(0)}}{\partial r} - \frac{\partial c^{(0)}}{\partial \theta}\frac{\partial \psi^{(0)}}{\partial r}\right) &= 0, \\
\frac{\partial \omega^{(0)}}{\partial t} + \frac{1}{r}\left(\frac{\partial \psi^{(0)}}{\partial \theta}\frac{\partial \omega^{(0)}}{\partial r} - \frac{\partial \omega^{(0)}}{\partial \theta}\frac{\partial \psi^{(0)}}{\partial r}\right) &= 0, \\
\omega^{(0)} &= -\left(\frac{1}{r}\frac{\partial}{\partial r} r \frac{\partial}{\partial r} + \frac{1}{r^2}\frac{\partial^2}{\partial \theta^2}\right)\psi^{(0)},
\end{aligned}\right\}$$

with initial conditions

$$\left.\begin{aligned}
c^{(0)}(r,\theta,0) &= \frac{\partial \widetilde{c}}{\partial x} r\cos\theta + \frac{\partial \widetilde{c}}{\partial y} r \sin\theta, \\
\omega^{(0)}(r,\theta,0) &= \frac{1}{r}\frac{\mathrm{d}}{\mathrm{d}r} r^2 \Omega(r).
\end{aligned}\right\}$$

As expected, the $O(g^0)$ equations are the passive scalar equations. We immediately write its solution,

$$\left.\begin{aligned}
c^{(0)}(r,\theta,t) &= \frac{\partial \widetilde{c}}{\partial x} r\cos(\theta - \Omega t) + \frac{\partial \widetilde{c}}{\partial y} r \sin(\theta - \Omega t), \\
\omega^{(0)}(r,\theta,t) &= \frac{1}{r}\frac{\mathrm{d}}{\mathrm{d}r} r^2 \Omega, \\
\frac{\partial \psi^{(0)}}{\partial r}(r,\theta,t) &= -r\Omega,
\end{aligned}\right\} \tag{3.19}$$

which can be verified by direct substitution. This is the same as the solution obtained by Pullin (2000). Physically, (3.19) represents the convective action of the vortex, winding the linear scalar gradient into tight spirals, effectively flattening the mean scalar gradient, and results in a counter-gradient subgrid scalar flux.

The equations for the first-order correction can be obtained by collecting $O(g^1)$ terms in the perturbation expansion, giving

$$\left.\begin{aligned}
\frac{\partial c^{(1)}}{\partial t} + \Omega\frac{\partial c^{(1)}}{\partial \theta} + \frac{1}{r}\left(\frac{\partial \psi^{(1)}}{\partial \theta}\frac{\partial c^{(0)}}{\partial r} - \frac{\partial c^{(0)}}{\partial \theta}\frac{\partial \psi^{(1)}}{\partial r}\right) &= 0, \\
\frac{\partial \omega^{(1)}}{\partial t} + \Omega\frac{\partial \omega^{(1)}}{\partial \theta} + \frac{1}{r}\left(\frac{\partial \psi^{(1)}}{\partial \theta}\frac{\partial \omega^{(0)}}{\partial r} - \frac{\partial \omega^{(0)}}{\partial \theta}\frac{\partial \psi^{(1)}}{\partial r}\right) &= -\left(\frac{\partial c^{(0)}}{\partial r}\cos\theta - \frac{1}{r}\frac{\partial c^{(0)}}{\partial \theta}\sin\theta\right), \\
\omega^{(1)} &= -\left(\frac{1}{r}\frac{\partial}{\partial r} r \frac{\partial}{\partial r} + \frac{1}{r^2}\frac{\partial^2}{\partial \theta^2}\right)\psi^{(1)},
\end{aligned}\right\} \tag{3.20}$$

with initial conditions

$$c^{(1)}(r,\theta,0) = 0, \quad \omega^{(1)}(r,\theta,0) = 0.$$

Substituting the $O(g^0)$ quantities given by (3.19) into the $\omega^{(1)}$ equation in (3.20), we obtain

$$\frac{\partial\omega^{(1)}}{\partial t}+\Omega\frac{\partial\omega^{(1)}}{\partial\theta}+\frac{1}{r}\frac{\mathrm{d}}{\mathrm{d}r}\left(\frac{1}{r}\frac{\mathrm{d}}{\mathrm{d}r}r^2\Omega\right)\frac{\partial\psi^{(1)}}{\partial\theta}=\frac{\partial\widetilde{c}}{\partial x}\left(-\cos(\Omega t)-rt\Omega'\sin(\theta-\Omega t)\cos\theta\right)+\frac{\partial\widetilde{c}}{\partial y}\left(\sin(\Omega t)+rt\Omega'\cos(\theta-\Omega t)\cos\theta\right). \tag{3.21}$$

Based on the nonzero Fourier modes on the right-hand side of (3.21), we can write its solution as the Fourier expansion,

$$\left.\begin{aligned}\psi^{(1)}(r,\theta,t)&=\psi_0^{(1)}(r,t)+\psi_2^{(1)}(r,t)\mathrm{e}^{\mathrm{i}2\theta}+\psi_{-2}^{(1)}(r,t)\mathrm{e}^{\mathrm{i}(-2)\theta},\\ \omega^{(1)}(r,\theta,t)&=\omega_0^{(1)}(r,t)+\omega_2^{(1)}(r,t)\mathrm{e}^{\mathrm{i}2\theta}+\omega_{-2}^{(1)}(r,t)\mathrm{e}^{\mathrm{i}(-2)\theta},\end{aligned}\right\} \tag{3.22}$$

where $\omega_2^{(1)}=\omega_{-2}^{(1)*}$, $\psi_2^{(1)}=\psi_{-2}^{(1)*}$ and initial conditions $\omega_n^{(1)}(r,0)=0$, $c_n^{(1)}(r,0)=0$ for $n=0,\pm2$. The axisymmetric mode $\omega_0^{(1)}$ can be solved directly, and then integrated to obtain

$$\frac{\partial\psi_0^{(1)}}{\partial r}=-\frac{1}{r}\int r\omega_0^{(1)}\mathrm{d}r=\frac{\partial\widetilde{c}}{\partial x}\left(\frac{r\sin(\Omega t)}{2\Omega}\right)+\frac{\partial\widetilde{c}}{\partial y}\left(\frac{r(\cos(\Omega t)-1)}{2\Omega}\right). \tag{3.23}$$

Similarly, after substituting (3.19) and (3.22) into the $c^{(0)}$ equations in (3.20), and then inspecting the nonzero Fourier modes, we write its solution as the Fourier expansion,

$$c^{(1)}(r,t)=c_1^{(1)}(r,t)\mathrm{e}^{\mathrm{i}1\theta}+c_{-1}^{(1)}(r,t)\mathrm{e}^{\mathrm{i}(-1)\theta}+c_3^{(1)}(r,t)\mathrm{e}^{\mathrm{i}3\theta}+c_{-3}^{(1)}(r,t)\mathrm{e}^{\mathrm{i}(-3)\theta}. \tag{3.24}$$

3.3.3 Kinetic Energy

Summarizing the results of the previous section, the azimuthal velocity is

$$u_\theta=-\frac{\partial\psi}{\partial r}=-\frac{\partial\psi^{(0)}}{\partial r}+g\left(-\frac{\partial\psi_0^{(1)}}{\partial r}-\frac{\partial\psi_2^{(1)}}{\partial r}\mathrm{e}^{\mathrm{i}2\theta}-\frac{\partial\psi_{-2}^{(1)}}{\partial r}\mathrm{e}^{\mathrm{i}(-2)\theta}\right)+O(g^2),$$

and the radial velocity is

$$u_r=\frac{1}{r}\frac{\partial\psi}{\partial\theta}=g\left(\frac{\mathrm{i}2}{r}\psi_2^{(1)}\mathrm{e}^{\mathrm{i}2\theta}+\frac{\mathrm{i}(-2)}{r}\psi_{-2}^{(1)}\mathrm{e}^{\mathrm{i}(-2)\theta}\right)+O(g^2).$$

We then calculate the ensemble-averaged kinetic energy,

$$\begin{aligned}K_g&=\left\langle\frac{1}{2}\left(u_\theta^2+u_r^2\right)\right\rangle\\&=\left\langle\frac{1}{2}\left(\frac{\partial\psi^{(0)}}{\partial r}\right)^2\right\rangle+g\left\langle\frac{\partial\psi^{(0)}}{\partial r}\left(\frac{\partial\psi_0^{(1)}}{\partial r}+\frac{\partial\psi_2^{(1)}}{\partial r}\mathrm{e}^{\mathrm{i}2\theta}+\frac{\partial\psi_{-2}^{(1)}}{\partial r}\mathrm{e}^{\mathrm{i}(-2)\theta}\right)\right\rangle+O(g^2),\end{aligned}$$

where the average is taken over space, time and the sign of Ω:

$$\langle\,\rangle = \frac{1}{2}\sum_{\operatorname{sgn}\Omega}\frac{1}{T}\int_0^T \frac{1}{\pi R_1^2}\int_0^{2\pi}\int_0^{R_1}(\,)\,r\,\mathrm{d}r\,\mathrm{d}\theta\,\mathrm{d}t,$$

where T is the vortex eddy-turnover time and R_1 is the vortex size. The θ-integral removes terms containing the factor $\mathrm{e}^{n\theta}$ for $n \neq 0$, therefore simplifying K_g to

$$K_g = \left\langle \frac{1}{2}\left(\frac{\partial\psi^{(0)}}{\partial r}\right)^2 \right\rangle + g\left\langle \frac{\partial\psi^{(0)}}{\partial r}\frac{\partial\psi_0^{(1)}}{\partial r}\right\rangle + O(g^2).$$

Substituting the solutions, (3.19) and (3.23), we obtain

$$K_g = \frac{1}{R_1^2}\int_0^{R_1} r^3\Omega^2\,\mathrm{d}r + g\frac{\partial\widetilde{c}}{\partial y}\frac{1}{R_1^2}\int_0^{R_1}\frac{r^3(-\sin(\Omega T)+\Omega T)}{\Omega T}\,\mathrm{d}r + O(g^2).$$

Next, we rescale variables according to

$$\Omega(r) = \frac{\Gamma}{R^2}\widehat{\Omega}(\xi), \quad \xi = \frac{r}{R}, \quad \sigma = \frac{\Gamma T}{R^2},$$

where $R \leq R_1$ and $\sigma = O(1)$, to write

$$K_g = \frac{\Gamma^2}{R_1^2}\int_0^{R_1/R}\xi^3\widehat{\Omega}^2\,\mathrm{d}\xi + g\frac{\partial\widetilde{c}}{\partial y}\frac{R^4}{R_1^2}\int_0^{R_1/R}\frac{\xi^3(-\sin(\sigma\widehat{\Omega})+\sigma\widehat{\Omega})}{\sigma\widehat{\Omega}}\,\mathrm{d}\xi + O(g^2).$$

The dominant contribution to the second integral comes near $\xi = R_1/R$ because the integrand contains the ξ^3 factor, which is small near $\xi = 0$. Since $\widehat{\Omega}(R_1/R) \ll 1$ for a compact vortex, we can replace the sine with its series expansion about its origin, and then collect terms to obtain the simple expression

$$K_g \sim K_v(1 - Ri/6), \quad \text{where} \quad K_v = \frac{\Gamma^2}{R_1^2}\int_0^{R_1/R}\xi^3\widehat{\Omega}^2\,\mathrm{d}\xi. \tag{3.25}$$

K_v is the vortex kinetic energy for the passive scalar model (Pullin 2000) and Ri is defined in (3.17). When a flow is stably stratified ($Ri > 0$), (3.25) says that the kinetic energy is reduced as countergradient motion is converted into potential energy, and vice versa.

3.3.4 Scalar Flux

We calculate the ensemble-averaged scalar flux (f_x, f_y):

$$f_x + \mathrm{i}f_y \equiv \langle cu\rangle + \mathrm{i}\langle cv\rangle = \langle cu_r\mathrm{e}^{\mathrm{i}\theta}\rangle + \langle cu_\theta\mathrm{i}\mathrm{e}^{\mathrm{i}\theta}\rangle.$$

Substituting the $O(g^0)$ solution, (3.19), and the $O(g^1)$ Fourier expansions, (3.22) and (3.24), and then dropping the terms containing $\mathrm{e}^{n\theta}$ for $n \neq 0$, we write

$$f_x + \mathrm{i}f_y = \left\langle \frac{1}{2}\mathrm{i}\mathcal{C}\mathrm{e}^{\mathrm{i}\Omega t} r^2 \Omega \right\rangle + g\left(\left\langle -\mathrm{i}\,\mathcal{C}^* \mathrm{e}^{-\mathrm{i}\Omega t} \psi_{-2}^{(1)} \right\rangle + \left\langle \mathrm{i}c_{-1}^{(1)} r\Omega \right\rangle \right.$$
$$\left. + \left\langle -\frac{1}{2}\mathrm{i}r\mathcal{C}^* \frac{\partial \psi_{-2}^{(1)}}{\partial r} \mathrm{e}^{-\mathrm{i}\Omega t} \right\rangle + \left\langle -\frac{1}{2}\mathrm{i}r\mathcal{C} \frac{\partial \psi_0^{(1)}}{\partial r} \mathrm{e}^{\mathrm{i}\Omega t} \right\rangle \right) + O(g^2). \tag{3.26}$$

where

$$\mathcal{C} = \frac{\partial \widetilde{c}}{\partial x} + \mathrm{i}\frac{\partial \widetilde{c}}{\partial y}.$$

We further assume that the phases of the nonaxisymmetric modes, $\arg \psi_{-2}^{(1)}$ and $\arg c_{-1}^{(1)}$, are random (uniformly distributed in the range 0–2π), and therefore vanish under the ensemble average $\langle\ \rangle$. The remaining terms in (3.26) represent the scalar flux resulting from the interaction between the $O(g^0)$ scalar field and the collective effects of the $O(g^0)$ axisymmetric vorticity and its $O(g^1)$ correction. After ensemble-averaging, rescaling and expanding trigonometric functions under the integrals, (3.26) becomes

$$f_x + \mathrm{i}f_y = -\frac{1}{2}K_v T\mathcal{C} + g\left(\frac{-\mathrm{i}R_1^2 T}{16}\mathcal{C}\frac{\partial \widetilde{c}}{\partial x} + \frac{\mathrm{i}T^3 K_v}{48}\mathcal{C}\left(4\frac{\partial \widetilde{c}}{\partial x} + \mathrm{i}3\frac{\partial \widetilde{c}}{\partial y} \right) \right) + O(g^2),$$

Substitute $T = \gamma\Delta/K_v^{1/2}$ and further assume that $R_1 = \gamma\Delta$, where $\gamma = O(1)$, to get

$$\left.\begin{aligned} f_x &= -\frac{1}{2}\gamma\Delta K_v^{1/2}\frac{\partial \widetilde{c}}{\partial x}\left[1 + Ri\left(-\frac{1}{6} \right) \right], \\ f_y &= -\frac{1}{2}\gamma\Delta K_v^{1/2}\frac{\partial \widetilde{c}}{\partial y}\left[1 + Ri\left(-\frac{1}{8} + \frac{\zeta^2}{24} \right) \right], \end{aligned}\right\} \tag{3.27}$$

where $\zeta = (\partial\widetilde{c}/\partial x)/(\partial\widetilde{c}/\partial y)$ and $Ri = -g(\partial\widetilde{c}/\partial y)\Delta^2/K_v$; we set $\gamma = 1$ in the correction terms. According to (3.27), the active scalar flux is reduced when the fluid is stably stratified ($Ri > 0$). However, the size of the coefficients multiplying Ri in (3.27) suggests that the first-order corrections are small.

3.3.5 *A Posteriori* Testing of Active Scalar SGS Model

The DNS data of chapter 2 provides an opportunity to test our SGS model (3.27) for active scalar mixing in LES. Considered as part of a multiscale framework, each of the DNS simulations can be viewed as a unit of statistically stationary turbulence found in an LES cell embedded in a density gradient.

Even though we have argued that the buoyancy corrections are only useful for stably stratified flows ($Ri > 0$), the terms in (3.27) are still defined when $Ri < 0$, and we can certainly set $Ri = 0$

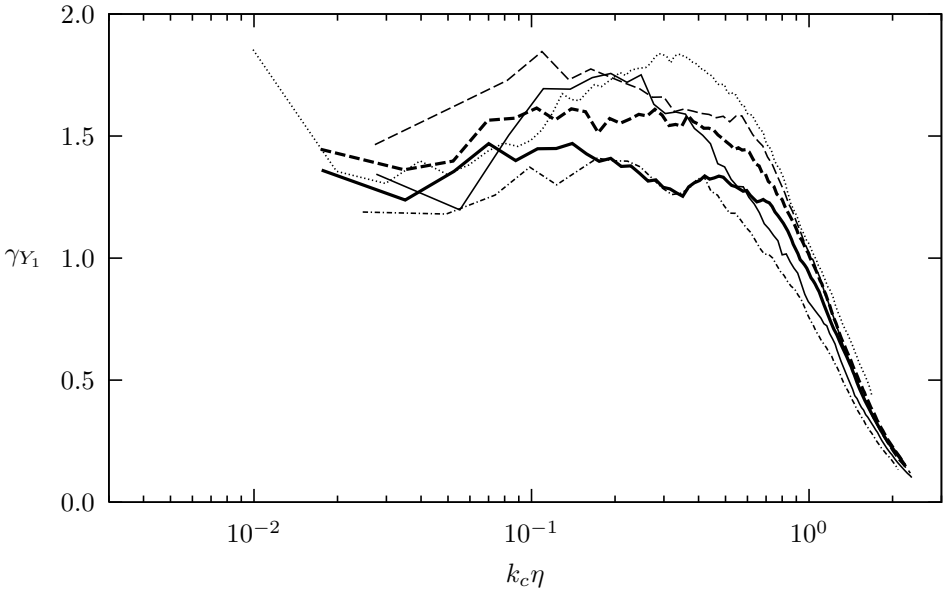

Figure 3.6. Normalized scalar flux using passive scalar SGS model, given by (3.29) with $Ri = 0$. See table 2.1 for key.

for passive scalars.

Recasting (3.27) into the framework of chapter 2, (also compare with (3.8)), we have

$$\langle \rho'' w'' \rangle_c = -\gamma_{Y_1} \frac{\Delta_c}{2} K^{1/2} \frac{\partial \langle \rho \rangle_c}{\partial z} \left(1 - \frac{Ri}{8} \right), \tag{3.28}$$

where gravity points in the $-z$ direction; Y_1 is the scalar; $\langle\ \rangle_c$ is interpreted as the xy-plane LES filter associated with the cutoff scale Δ_c ($\equiv \pi/k_c$), formally defined as

$$\langle f'' g'' \rangle_c = \int_{k_c}^{\infty} E_{fg}^{2D}(k_r)\, \mathrm{d}k_r,$$

$k_r = (k_x^2 + k_y^2)^{1/2}$; $Ri = -(g/\langle \rho \rangle_c)(\partial \langle \rho \rangle_c / \partial z)\Delta_c^2 / K$; and $K = \langle u_i'' u_i'' \rangle_c / 2$ is the subgrid (specific) kinetic energy. Pullin (2000) estimated that $\gamma_{Y_1} = 0.89$–1.3. Solving for γ_{Y_1},

$$\gamma_{Y_1}(k_c) = \frac{-\langle \rho'' w'' \rangle_c}{(\Delta_c/2)\left(\langle u_i'' u_i'' \rangle_c / 2\right)^{1/2} \left(\partial \langle \rho \rangle_c / \partial z\right)(1 - Ri/8)}, \tag{3.29}$$

which can be interpreted as the normalized subgrid scalar flux.

Plotting $\gamma_{Y_1}(k_c)$ using $Ri = 0$ at the midplane location ($z = L_z/2$) for all the DNS simulations in figure 3.6, we observe that, in agreement with the analysis by Pullin (2000), $\gamma = O(1)$ and is roughly constant with values in the range 1.2–1.8 over one decade of wavenumbers before dropping to zero when $k_c\eta > 1$. This is rather surprising, since we have applied a passive scalar model to an active scalar with moderately high density ratios, $R = 3$, 7. A possible explanation is that,

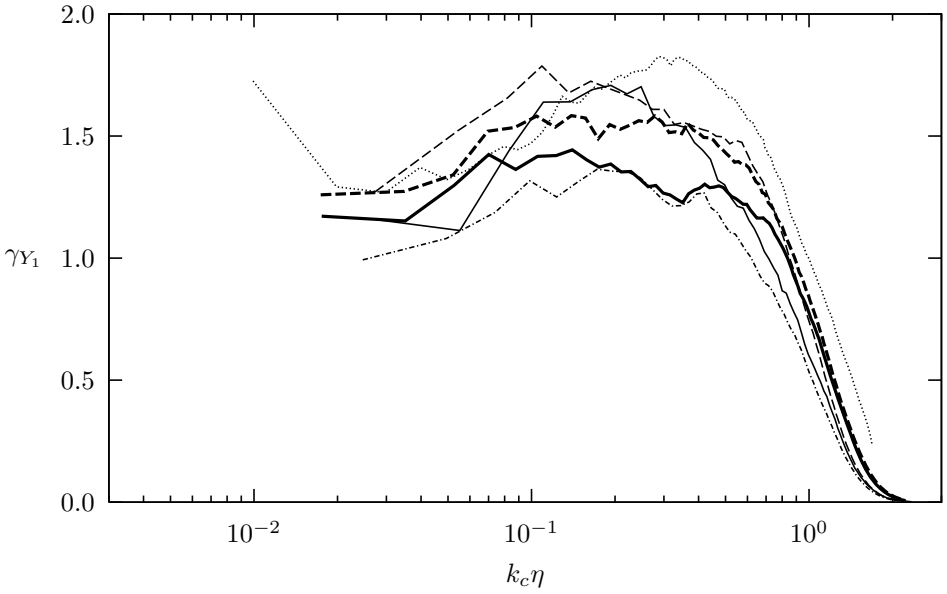

Figure 3.7. Normalized scalar flux using active scalar SGS model, given by (3.29). See table 2.1 for key.

regardless of R, the present simulations of unstably stratified flows are still rate limited by turbulent mixing, which is a key argument used in the development of the passive scalar flux model. One could imagine a different outcome in a stably stratified configuration ($Ri > 0$), where stable stratification overwhelms turbulent mixing by converting kinetic energy related to countergradient motion into potential energy, effectively damping the flow.

We also plot (3.29) with the Ri corrections in figure 3.7, showing that, as expected, $\gamma_{Y_1}(k_c)$ remains relatively unchanged, compared to figure 3.6, which did not have the buoyancy corrections.

Chapter 4

LES and Wall Modeling of Wall-Bounded Turbulence

4.1 Background

The idea of LES—directly simulating the large eddies while modeling the small eddies—cannot be applied near walls in a straightforward way. Near walls, "large eddies", implicitly defined by the coarse grid, simply do not exist (Pope 2004). The near-wall eddies, having sizes constrained by the wall, become underresolved at high Re and are therefore considered part of the subgrid motion. In unbounded flows, the large eddies, carrying most of the turbulent kinetic energy, set the lengthscales and timescales that describe the rest of the small-scale turbulence. This picture is reversed near the wall, where the most energetically productive eddies are necessarily part of the small-scale motion. Further, both these descriptions are present in wall-bounded flows, and both contribute significantly to the overall turbulent flow field. This was demonstrated by Hutchins and Marusic (2007b), who plotted velocity spectra of high-Re boundary layers at various wall distances and showed the existence of two distinct energetic peaks: one that scales with viscous units, another that scales with boundary layer thickness. Guided by even higher Re experiments (Mathis, Hutchins and Marusic 2009), they later revised the location of the outer peak to scale as $z \sim Re_\tau^{1/2}$. A related complication is that, given sufficiently high Re, even the mean velocity gradient is too steep to be resolved on the coarse LES grid, appearing as a numerical discontinuity. The jump conditions across this discontinuity depend on unclosed turbulent stresses, which themselves require reliable models.

One can always perform a partially resolved LES, where the near-wall grid is refined to resolve the near-wall eddies (e.g., Voelkl, Pullin and Chan 2000). Although this kind of simulation has its role in the development of LES models, its resolution requirement, which scales as $O(Re^{1.8})$ (Piomelli 2008), is almost as restrictive as DNS. But if we require that the resolution requirements of LES be at most weakly dependent on Re, we are forced to explicitly model the vigorous near-wall fluctuations and the numerical discontinuity (slip) in the mean velocity profile. Ample experimental

evidence that suggests some degree of universality in wall-bounded flows, e.g., the empirical log law of the wall, offers hope that a viable LES wall model could be found.

Past modeling efforts were focussed on fitting a log law to the near-wall filtered velocity to obtain the implied wall shear stress, which, in turn, is used as a wall stress boundary condition (Cabot and Moin 1999, Pantano et al. 2008). Instead of the log law, the thin boundary layer equations (TBLEs) coupled with a damped mixing-length eddy viscosity can also be used, giving good agreement with experiments even in separating flows (Cabot and Moin 1999, Wang and Moin 2002). Yet another method of determining the wall stress is by matching the LES eddy viscosity with the Reynolds-averaged Navier–Stokes (RANS) eddy viscosity (Templeton, Medic and Kalitzin 2005), with success at high Re.

We do not attempt to describe each of these methods in detail, but we will highlight some of these efforts to provide a sample of the prevalent ideas in the field. Pantano et al. (2008) used $800\times302\times64$ points to simulate flow in a $8\pi\delta \times 3\pi\delta \times 2\delta$ channel up to $Re_\tau = 2\,\mathrm{M}$. They demonstrated that the stretched-vortex SGS model (Misra and Pullin 1997) was able to capture anisotropic near-wall SGS stresses. Their wall model involves relating the instantaneous wall-parallel velocity to the wall shear stress boundary condition via the log law with empirical constants. Although we presently use the same SGS model for the interior LES (away from the wall), we use a different wall model, one that is based on the phenomenology of attached eddies and the conservation of momentum—attached eddies to provide off-wall Dirichlet boundary conditions and conservation of momentum to provide an ODE for the wall shear stress.

Another interesting approach is taken by Templeton, Medic and Kalitzin (2005), who matched an expression for the near-wall LES eddy viscosity with the RANS counterpart to calculate both the wall shear stress boundary condition and the SGS eddy viscosity for the wall-adjacent cells. In the interior LES, they used the dynamic Smagorinsky SGS model (Germano, Piomelli, Moin and Cabot 1991) with the modification of Lilly (1992). They reported good results up to $Re_\tau = 10\,\mathrm{k}$ with only $32 \times 32 \times 33$ points in a $2\pi\delta \times \pi\delta \times 2\delta$ channel. Templeton, Wang and Moin (2008) later used a more sophisticated technique employing optimal control to couple a RANS model with the LES. In contrast, the present effort attempts to circumvent some of the inherent empiricism in RANS models by developing a unified framework of SGS modeling and wall modeling based on the stretched-spiral vortex model of (Misra and Pullin 1997).

Presently we apply the wall stress boundary condition in reverse: given the wall shear stress, we impose the corresponding slip velocity at a predetermined lifted virtual boundary, located well above the viscous layer and fixed in outer coordinates. We approach the wall modeling problem by considering the physics of near-wall vortices, giving us a relationship between the wall shear stress and slip velocity. We assume that the dynamics of each wall-adjacent cell are partially determined by its wall shear stress, similar to the class of equilibrium-stress models (see Piomelli 2008), but,

presently, the wall shear stress is governed by its own ordinary differential equation (ODE) derived from assumptions somewhat like those used to derive the TBLE. We do not, however, use an inner mesh to solve the TBLE, called a zonal approach by Piomelli and Balaras (2002); instead, we assume only that the law of the wall, irrespective of its detailed form, holds locally. This is then used only for the treatment of one term in our reduction of the streamwise momentum equation. Indeed, our approach attempts to essentially eliminate the Reynolds number dependence of the wall model. In terms of the classification of Piomelli (2008), we have combined elements of both the equilibrium-stress models and the zonal approaches, since we assume a localized near-wall layer characterized by its wall shear stress, and we also solve a reduced form of the TBLE.

Much understanding of wall turbulence has been gained by studying simple physical models based on a statistical ensemble of vortical structures that have tractable analytical expressions. The attached eddy model of Townsend (1976) (see also Perry and Chong 1982, Nickels et al. 2007) was able to reproduce various observed physics of wall turbulence, e.g., the mean velocity profile, the Reynolds stress profiles and some aspects of the velocity spectra. A part of our wall model is based on related ideas, where we assume a hierarchy of vortices with sizes that scale with wall distance. These are aligned in the streamwise direction and act to wrap the streamwise momentum, that is the vortex axial velocity, as if it behaved locally like a passive scalar.

In what follows, the filtered Navier–Stokes equations are given in § 4.2.1, and the basics of the stretched-vortex SGS model (Misra and Pullin 1997) are described in § 4.2.2. This is followed by the development of an extended SGS model that incorporates the effect of vortex winding of axial velocity to produce off-diagonal components of the vortex-frame subgrid Reynolds stresses (§ 4.2.3). We then introduce the ideas of wall-normal averaging (§ 4.3.1) and local–inner scaling (§ 4.3.2), which together lead to an ODE for the wall-normal streamwise velocity gradient at each wall-adjacent cell without the need to resolve the wall layer. The SGS dynamics in the wall-adjacent cell are split into three layers (§ 4.3.3): a viscous dominated region, a constant-stress region and an outer region. The extended SGS model, applied within the constant-stress layer with streamwise-aligned SGS vortices, leads to a log relationship for the streamwise velocity. A factor, equivalent to an inverse Kármán-like constant, that multiplies the log term is calculated dynamically by the LES to within a mixing constant. The latter is determined *a priori* by a stress-matching argument. Together with the use of an empirically determined matching point, in inner variables, for the logarithmic and viscous sublayer velocity intersection, the overall SGS wall model provides a slip boundary condition for the streamwise velocity at a lifted "virtual" wall (§ 4.3.4) that is placed within the log layer. Statistical estimates of the Kármán "constant" can then be obtained from the LES. Details of the numerical method are in § 4.4, and the results obtained from LES of channel flow are described in detail in § 4.5.

4.2 Equations of Motion and SGS Model

4.2.1 Filtered Navier–Stokes Equations

Presently, the following notation is adopted: x_1 or x is the streamwise coordinate; x_2 or y is the spanwise coordinate; and x_3 or z is the wall-normal coordinate. We obtain the governing equations for LES by applying a filter to the Navier–Stokes equations. Presently this filtering operation is considered strictly formal; no explicit filtering is used in the present work. We shall denote with a tilde any field quantity $\phi(\boldsymbol{x})$ subjected to the filter G with cutoff length Δ_c, that is

$$\widetilde{\phi}(\boldsymbol{x}) = \int G(\boldsymbol{x}-\boldsymbol{x}';\Delta_c)\phi(\boldsymbol{x}')\,\mathrm{d}\boldsymbol{x}'.$$

Except for Δ_c, which is prescribed through the SGS model, no other filter properties enter into the flow simulation. After applying the filter and explicitly decomposing the velocity field as $u_i \equiv \widetilde{u}_i + u_i'$, we obtain the filtered Navier–Stokes equations

$$\frac{\partial \widetilde{u}_i}{\partial t} + \frac{\partial \widetilde{u}_i\widetilde{u}_j}{\partial x_j} = -\frac{\partial \widetilde{p}}{\partial x_i} + \nu\frac{\partial^2 \widetilde{u}_i}{\partial x_j^2} - \frac{\partial T_{ij}}{\partial x_j} + f(t)\delta_{i1}, \quad \frac{\partial \widetilde{u}_i}{\partial x_i} = 0,$$

$$T_{ij} = \widetilde{u_i u_j} - \widetilde{u}_i\widetilde{u}_j = \widetilde{\widetilde{u}_i u_j'} + \widetilde{u_i'\widetilde{u}_j} + \widetilde{u_i' u_j'}.$$

In the above equation T_{ij} is the subgrid stress tensor. We have neglected the Leonard stresses since a numerical method with high spectral resolution is used, allowing us to focus on LES modeling; ν is the kinematic viscosity; p is the kinematic pressure; and $f(t)$ is a force that maintains a given mass flux through the channel. Temporal filtering is implicit in LES, since the time step size is chosen by the Courant–Friedrichs–Levy (CFL) condition, which is based on the advection timescale of spatially resolved scales. In other words, spatially unresolved scales are also temporally unresolved.

4.2.2 The Stretched-Vortex SGS Model

The stretched-spiral vortex (Lundgren 1982) is a physical model for turbulent fine scales, where the flow is composed of tube-like structures with concentrated vorticity. On a segment of such tubes, the flow is approximated by an axially stretched two-dimensional flow. These simplified equations admit analytical large-time asymptotic solutions, from which ensemble statistics, such as correlation and spectra, follow. These have been studied extensively and were found to be consistent with experimental data (e.g., Pullin and Saffman 1993, Pullin and Lundgren 2001, O'Gorman and Pullin 2003).

Misra and Pullin (1997) used a stretched vortex to model subgrid scales for LES in the following way: Embedded in each computational cell it is assumed that there exists a superposition of stretched

vortices, each having orientation taken from a p.d.f. If we further assume that the subgrid ensemble dynamics are dominated by a vortex aligned with the unit vector $\boldsymbol{e}^v$, modeled via a delta-function p.d.f., the resulting subgrid stress tensor of the ensemble is (Misra and Pullin 1997)

$$T_{ij} = (\delta_{ij} - e_i^v e_j^v)K, \tag{4.1}$$

where K is the subgrid kinetic energy,

$$K = \int_{k_c}^{\infty} E(k)\,\mathrm{d}k, \tag{4.2}$$

where presently, we use the cutoff wavenumber $k_c = \pi/\Delta_c$, $\Delta_c = (\Delta_x\,\Delta_y\,\Delta_z)^{1/3}$, and $E(k)$ is the SGS energy spectrum.

The above expression is essentially kinematical and is independent of the detailed subgrid vortex dynamics. If it is further assumed that the SGS vortices are of the stretched-spiral type, which have energy spectra, determined by detailed Navier–Stokes dynamics, of the form (Lundgren 1982)

$$E(k) = \mathcal{K}_0 \epsilon^{2/3} k^{-5/3} \exp\left[-2k^2\nu/(3|\widetilde{a}|)\right], \tag{4.3}$$

where $\widetilde{a} = e_i^v e_j^v \widetilde{S}_{ij}$, the stretching felt along the subgrid vortex axis imposed by the resolved scales, and $\widetilde{S}_{ij} = (1/2)\,(\partial\widetilde{u}_i/\partial x_j + \partial\widetilde{u}_j/\partial x_i)$, the resolved strain-rate tensor, then combining (4.2) and (4.3), we obtain

$$K = \frac{1}{2}\,\mathcal{K}_0'\,\Gamma\left[-1/3, \kappa_c^2\right],$$

where

$$\mathcal{K}_0' = \mathcal{K}_0 \epsilon^{2/3} \lambda_v^{2/3}, \quad \lambda_v = (2\nu/3|\widetilde{a}|)^{1/2}, \quad \kappa_c = k_c \lambda_v.$$

In the above expressions Γ is an incomplete gamma function, and κ_c^2 can be interpreted as the inverse grid-level Re: the LES model is most active when $\kappa_c \to 0$ and turns off for $\kappa_c \to \infty$.

Except for the choice of $\boldsymbol{e}^v$, we obtain a parameter-free SGS model by calculating the grouped constant $\mathcal{K}_0'$ from the following matching procedure (Voelkl, Pullin and Chan 2000): Calculate the local average, denoted by $\langle\ \rangle$, of the resolved-scale second-order structure function from the running LES simulation, and match it to the stretched-spiral vortex prediction of the same grouped constant,

$$\langle F_2 \rangle = \left\langle 4 \int_0^{k_c} E(k)\,[1 - J_0(kr)]\ \mathrm{d}k \right\rangle,$$

where F_2 is the local second-order structure function as calculated from the running simulation,

$$F_2 = [\delta\widetilde{u}_i]^2 = [\widetilde{u}_i(\boldsymbol{x}) - \widetilde{u}_i(\boldsymbol{x}')]^2, \quad r^2 = (|\delta\boldsymbol{x}|)^2 - (\delta\boldsymbol{x}\cdot\boldsymbol{e}^v)^2, \quad \delta\boldsymbol{x} = \boldsymbol{x} - \boldsymbol{x}'.$$

Here, $\boldsymbol{x}'$ is the integration variable; J_0 is the zeroth-order Bessel function of the first kind; and r is the distance from $\boldsymbol{x}'$ to the vortex axis. Substituting the energy spectrum, (4.3), and simplifying, we find that

$$\mathcal{K}_0' = \langle F_2 \rangle \,/\, \langle Q(\kappa_c, d) \rangle \,,$$

where

$$d = r/\Delta_c, \quad Q(\kappa_c, d) = 4 \int_0^{\kappa_c} \kappa^{-5/3} \mathrm{e}^{-\kappa^2} \left[1 - J_0((\kappa/\kappa_c)\,\pi\, d)\right] \,\mathrm{d}\kappa.$$

Computationally efficient asymptotic approximations for $Q(\kappa_c, d)$ as $\kappa_c \to 0$, similar to Voelkl, Pullin and Chan (2000), are presently used.

We now choose the averaging operator to be the ensemble average,

$$\langle \phi \rangle = \frac{1}{N} \sum_{\boldsymbol{x}' \in \mathcal{N}(\boldsymbol{x})} \phi,$$

where ϕ is either F_2 or Q; $\mathcal{N}(\boldsymbol{x})$ is the set of all points near $\boldsymbol{x}$; and N is the number of points in $\mathcal{N}(\boldsymbol{x})$. Presently $\mathcal{N}(\boldsymbol{x})$ consists of points within the closed $(2\Delta_x) \times (2\Delta_y) \times (2\Delta_z)$ block centered on $\boldsymbol{x}$, that is

$$\mathcal{N}(\boldsymbol{x}) = \{\boldsymbol{x}' : \boldsymbol{x}' \neq \boldsymbol{x}, |x - x'| \leq \Delta_x, |y - y'| \leq \Delta_y, |z - z'| \leq \Delta_z\};$$

correspondingly, $N = 3^3 - 1 = 26$.

4.2.3 Extended Stretched-Vortex SGS Model

The original stretched-vortex SGS model consists of an ensemble of local two-dimensional two-component flows. That is, only planar motions of planar velocities of these local flows are considered when calculating ensemble statistics. The stretched-vortex SGS model used by Misra and Pullin (1997) and Voelkl, Pullin and Chan (2000) is largely based on this construction. Pullin and Lundgren (2001) found that planar motions (no axial coordinate dependence) inside cylindrical vortices convecting both passive scalars and the axial velocity could also be analyzed within the same stretched-spiral vortex framework. An asymptotic two-dimensional three-component flow solution exists for which the evolution of the axial velocity and of a passive scalar follows essentially the same mapped evolution equations (Pullin and Lundgren 2001, O'Gorman and Pullin 2003). Using a simplified version of analysis, Pullin (2000) developed a vortex-based, SGS scalar flux model (see also Hill, Pantano and Pullin 2006).

These ideas motivate the present extension to the stretched-vortex SGS stress model (Misra and Pullin 1997) by incorporating the added effects of axial velocity transport modeled as a passive

scalar. Recapitulating the result for subgrid scalar flux (Pullin 2000),

$$\widetilde{v_i'\widetilde{c}} = -K_s \frac{\partial \widetilde{c}}{\partial y_i} \quad \text{if} \quad i = 1, 2, \quad \widetilde{v_3'\widetilde{c}} = 0, \tag{4.4}$$

where $K_s = \gamma \Delta_c K^{1/2}/2$. Here, v_i is the vortex-frame velocity and y_i is the vortex-frame spatial coordinate (y_3 coincides with the vortex axis); $\widetilde{c}$ is the resolved passive scalar; v_i' is the vortex-frame subgrid velocity; and γ is an $O(1)$ universal dimensionless constant, estimated by Pullin (2000) to be equal to unity. Equation (4.4) says that the turbulent fluctuations of a subgrid spiral vortex of size Δ_c and energy K transports the passive scalar in a way that results in a net flux of resolved passive scalar against its gradient.

Assuming analogous axial velocity transport dynamics ($\widetilde{c} = \widetilde{v}_3$), we write the analogue of (4.4),

$$\widetilde{v_i'\widetilde{v}_3} = -K_s \frac{\partial \widetilde{v}_3}{\partial y_i} \quad \text{if} \quad i = 1, 2, \quad \widetilde{v_3'\widetilde{v}_3} = 0.$$

We shall later allow for a different value of γ appropriate to axial velocity transport (see § 4.3.5). Rotating back to the laboratory frame using the identities

$$\delta_{i3}\widetilde{v}_3 = \delta_{i3}(\delta_{j3}\widetilde{v}_j) = e_i^v(e_j^v\widetilde{u}_j),$$
$$(\delta_{i1}\delta_{j1} + \delta_{i2}\delta_{j2})\partial/\partial y_j = (\delta_{ij} - \delta_{i3}\delta_{j3})\partial/\partial y_j = (\delta_{ij} - e_i^v e_j^v)\partial/\partial x_j,$$

we arrive at the tensor form

$$\widetilde{u_i'\widetilde{u}_j} = -K_s \left[e_j^v e_k^v \frac{\partial \widetilde{u}_k}{\partial x_l}(\delta_{li} - e_l^v e_i^v) \right].$$

We add this, and its transpose (since the subgrid stress tensor is symmetric), to the existing terms, (4.1), to obtain the extended subgrid stress model:

$$\begin{aligned} T_{ij} &= \widetilde{u_i'u_j'} + \widetilde{u_i'\widetilde{u}_j} + \widetilde{\widetilde{u}_i u_j'} \\ &= K(\delta_{ij} - e_i^v e_j^v) - K_s \left[e_j^v e_k^v \frac{\partial \widetilde{u}_k}{\partial x_l}(\delta_{li} - e_l^v e_i^v) + e_i^v e_k^v \frac{\partial \widetilde{u}_k}{\partial x_l}(\delta_{lj} - e_l^v e_j^v) \right]. \end{aligned} \tag{4.5}$$

Note that the form is invariant under axis rotations and to sign reversals of $\boldsymbol{e}^v$. In other words, the subgrid stresses are understood to be produced by pairs of counterrotating SGS vortices. Also, the new terms are traceless so that the SGS kinetic energy remains unchanged ($T_{ii} = 2K$).

We will later use (4.5) in the development of a special SGS wall model while retaining the standard stretched-vortex model, with SGS vortex aligned with the most extensive eigenvector of the resolved strain-rate tensor, that is $\boldsymbol{e}^v = \boldsymbol{e}_{\widetilde{S}}$, within the main body of the flow.

4.3 Near-Wall SGS Model: Boundary Treatment

We now describe in detail the development of our wall-adjacent SGS model. This recognizes explicitly the highly anisotropic character of near-wall turbulence. The main idea is to integrate across the near-wall layer in a way that models the appropriate physics while providing a slip boundary condition at a raised virtual wall for the resolved-scale LES.

4.3.1 Near-Wall Filtering

A novel feature of our boundary treatment is an ODE governing the local wall shear stress that, when coupled with the LES, eliminates the need to resolve the near-wall region. In this section, we shall, without loss of generality, fix the location of the wall at $z = 0$. We first define an xy-plane filter:

$$\widetilde{\phi}(x, y, z, t) = \int\int \phi(x', y', z, t) G(x - x'; \Delta_f) G(y - y'; \Delta_f)\, \mathrm{d}x'\, \mathrm{d}y'. \tag{4.6}$$

We require the filter width Δ_f to be much larger than the viscous wall unit l^+, to be defined below. We apply this filter to the streamwise momentum equation to obtain

$$\frac{\partial \widetilde{u}}{\partial t} + \frac{\partial \widetilde{uu}}{\partial x} + \frac{\partial \widetilde{uv}}{\partial y} + \frac{\partial \widetilde{uw}}{\partial z} = -\frac{\partial \widetilde{p}}{\partial x} + \nu \frac{\partial^2 \widetilde{u}}{\partial z^2}, \tag{4.7}$$

where we have neglected lateral diffusion, which is justifiably small, given the relative size of the filter width. The planar filtering is purely formal; we do not perform such filtering or indeed any explicit filtering in the present approach. In terms of inner variables, $\Delta_f \gg l^+$, where $l^+ = (\nu/\eta_0)^{1/2}$ is the viscous, near-wall lengthscale and the wall velocity gradient η_0 is defined below. In outer variables $\Delta_f \ll \delta$, and we therefore consider G in (4.6) as a delta function for the purposes of LES, that is $\Delta_f = \Delta_x$ or Δ_y. The nonlinear terms include both resolved and subgrid contributions, $\widetilde{u_i u_j} = \widetilde{u}_i \widetilde{u}_j + T_{ij}$, and, for notational convenience, we have bundled the fluctuating pressure gradient with the mean pressure gradient, renaming $-\partial\widetilde{p}/\partial x + f(t)$ as $-\partial\widetilde{p}/\partial x$.

We next define a second, top-hat filter, which is an average in a wall-adjacent layer of arbitrary thickness, h,

$$\langle\phi\rangle(x, y, t) = \frac{1}{h} \int_0^h \widetilde{\phi}(x, y, z, t)\, \mathrm{d}z. \tag{4.8}$$

Applying this to (4.7) along with the no-slip condition, $\widetilde{u}(x, y, 0, t) = 0$, and assuming that the streamwise pressure gradient is constant throughout this wall-adjacent layer, we obtain

$$\frac{\partial \langle u\rangle}{\partial t} + \frac{\partial \langle uu\rangle}{\partial x} + \frac{\partial \langle uv\rangle}{\partial y} = -\frac{1}{h}\, \widetilde{uw}|_h - \left.\frac{\partial \widetilde{p}}{\partial x}\right|_h + \frac{\nu}{h}\left(\left.\frac{\partial \widetilde{u}}{\partial z}\right|_h - \eta_0 \right), \tag{4.9}$$

where the local wall streamwise velocity gradient is

$$\eta_0 \equiv \left.\frac{\partial \widetilde{u}}{\partial z}\right|_0 . \tag{4.10}$$

The local wall shear stress is $\tau_0(x,y,t) = \nu\eta_0(x,y,t) \equiv u_\tau^2(x,y,t)$ where $u_\tau(x,y,t)$ is the local wall-friction velocity. Since $\Delta_f \gg l^+$, each computational cell is effectively assumed to behave as a local statistically homogeneous unit of wall turbulence, similar to the so-called minimal flow unit of Jiménez and Moin (1991). Experiments based on one-dimensional filtering conducted by Nakayama, Noda and Maeda (2004) suggest $\Delta_f > 1800\, l^+$. When two-dimensional filtering is employed, as in the present LES application, they argued that filter widths larger than $\Delta_x^+ \times \Delta_y^+ = 200 \times 360$ are adequate.

4.3.2 Local–Inner Scaling

We now introduce a local–inner-scaling ansatz. This states that the statistics of each cell are characterized by their respective local–inner scales ν and $\eta_0(x,y,t)$ or equivalently l^+ and $u_\tau(x,y,t)$. Specifically, we assert that the SGS streamwise velocity, within a near-wall, sugbrid region to be defined subsequently, can, for each cell, be collapsed onto the form

$$\widetilde{u}(x,y,z,t) = (\nu\eta_0(x,y,t))^{1/2} F(z^+), \quad z^+ = z\,(\eta_0(x,y,t)/\nu)^{1/2} \equiv z/l^+, \tag{4.11}$$

where $F(z^+)$ can be thought of as a local "law of the wall". Next, differentiate (4.11) with respect to η_0 to give

$$\frac{\partial \widetilde{u}}{\partial \eta_0} = \frac{1}{2}(\nu/\eta_0)^{1/2}\left[F + z^+F'\right], \tag{4.12}$$

where $F' = \mathrm{d}F/\mathrm{d}z^+$; perform the wall-adjacent average (4.8); and then back-substitute the inner scaling (4.11), evaluated at $z = h$,

$$\frac{\partial \langle u\rangle}{\partial \eta_0} = \frac{1}{2}(\nu/\eta_0)^{1/2} F(h^+) = \frac{\widetilde{u}|_h}{2\eta_0},$$

where $\widetilde{u}|_h = F(h^+)$ with $h^+ = h/l^+$. Finally, using the chain rule we find

$$\frac{\partial \langle u\rangle}{\partial t} = \frac{\partial \langle u\rangle}{\partial \eta_0}\,\frac{\partial \eta_0}{\partial t} = \frac{\widetilde{u}|_h}{2\eta_0}\,\frac{\partial \eta_0}{\partial t}. \tag{4.13}$$

We emphasize that (4.13) is an exact consequence of (4.8) and (4.11). Moreover, using (4.13) to evaluate the time derivative of the plane-filtered and vertically averaged streamwise velocity, the explicit form of $F(z^+)$ in $0 \le z < h$ is not needed; this occurs owing to the cancellation of two integrals. The velocity $\widetilde{u}|_h$ will later be obtained directly from the LES.

Now substitute (4.13) into the first term of (4.9) to obtain

$$\frac{\widetilde{u}|_h}{2\eta_0}\frac{\partial \eta_0}{\partial t} + \frac{\partial \langle uu\rangle}{\partial x} + \frac{\partial \langle uv\rangle}{\partial y} = -\frac{1}{h}\,\widetilde{uw}|_h - \left.\frac{\partial \widetilde{p}}{\partial x}\right|_h + \frac{\nu}{h}\left(\left.\frac{\partial \widetilde{u}}{\partial z}\right|_h - \eta_0\right). \tag{4.14}$$

Our motivation for performing the wall-adjacent average, (4.8), is to remove the steep near-wall gradients, which we do not wish to resolve. In-plane (x, y) gradients of filtered quantities in (4.14) are now approximated by values at $z = h$, supplied by the LES,

$$\frac{\partial \langle uu\rangle}{\partial x} \approx \frac{\partial \widetilde{uu}|_h}{\partial x}, \quad \frac{\partial \langle uv\rangle}{\partial y} \approx \frac{\partial \widetilde{uv}|_h}{\partial y}.$$

This approximation captures some of the nonequilibrium effects arising from large-scale in-plane inhomogeneities. With these assumptions, we rewrite (4.14) as

$$\frac{\partial \eta_0}{\partial t} = \frac{2\eta_0}{\widetilde{u}|_h}\left[-\frac{1}{h}\,\widetilde{uw}|_h - \frac{\partial \widetilde{uu}|_h}{\partial x} - \frac{\partial \widetilde{uv}|_h}{\partial y} - \left.\frac{\partial \widetilde{p}}{\partial x}\right|_h + \frac{\nu}{h}\left(\left.\frac{\partial \widetilde{u}}{\partial z}\right|_h - \eta_0\right)\right]. \tag{4.15}$$

Equation (4.15) governs the evolution of the wall shear stress, written in terms of η_0. Viewed as a standalone entity, we treat (4.15) as an ODE driven by external forcing, even though it is strictly a partial differential equation when coupled with the LES. The right-hand side of (4.15) only involves known quantities at h, which is arbitrary. In practice, we choose h to be at the first grid point within the LES (see figure 4.1), and the quantities on the right-hand side can then be determined from resolved-scale LES quantities. We remark that our use of local–inner scaling, (4.11), is restricted to the reduction of the unsteady term in (4.9) and that this operation does not require a specific form for $F(z^+)$. The other terms in (4.15) will be provided from the resolved-scale LES itself, so that (4.15) can then be viewed in this sense as resulting from mixed inner–outer scaling. When coupled with an LES, (4.15) then allows us to determine the wall shear stress without resolving the near-wall steep gradients, which have been integrated out by the wall averaging. One can also interpret (4.15) as an integrated form of the local unsteady turbulent boundary layer equations with the added assumption of local–inner scaling for the unsteady term. Further, (4.15) knows nothing about the channel geometry and should, therefore, be applicable to general flows. To close this coupling, appropriate boundary conditions for the LES need to be applied, which is the subject of the next subsection.

4.3.3 Multilayer SGS Wall Model

We do not resolve the near-wall region. Instead, the LES computation takes place above a certain fixed, *Re*-independent height h_0, which will later be chosen as a small fraction of the near-wall cell size. To proceed we first define three regions for the lower half channel. It is understood that, for the present simulations, similar regions exist on the upper wall. These regions are (see figure 4.1)

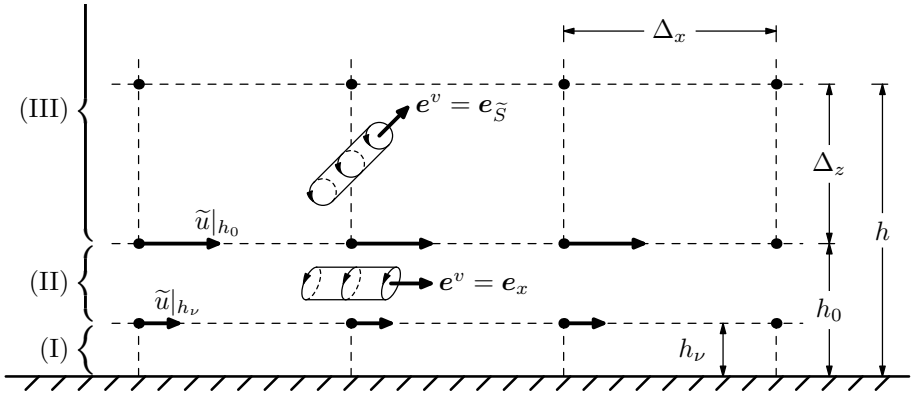

Figure 4.1. Schematic showing the near-wall setup: h_0 locates the lifted virtual wall, where boundary conditions are applied; h locates the input plane to the wall shear stress equation, (4.14); h_ν locates the outer edge of the viscous sublayer; $\boldsymbol{e}^v$ is the alignment of SGS vortices in their respective regions.

(i) $0 \le z \le h_\nu$, region (I), essentially the viscous sublayer;

(ii) $h_\nu < z \le h_0$, region (II), viewed as an overlap layer, where the shear stress is approximately constant and will be modeled by the extended stretched-vortex SGS model consisting of attached vortices aligned with $\boldsymbol{e}_x$; and

(iii) $h_0 < z \le \delta$, region (III), where nonuniversal outer flow features are computed with LES coupled with the original stretched-vortex SGS model of detached subgrid vortices aligned with $\boldsymbol{e}_{\widetilde{S}}$.

We remark that the combination of attached and detached vortices was also used by Marušić and Perry (1995) to model wall turbulence. The plane $z = h$ lies at the top of the first grid cell in region (III). The plane $z = h_0$ will be referred to as the lifted virtual wall. We now proceed to model the flow in regions (I) and (II) in a way that provides a slip velocity at $z = h_0$.

In region (I) we use $\widetilde{u}^+ = z^+$, where $\widetilde{u}^+ = \widetilde{u}/u_\tau$, $z^+ = z/l^+$, and u_τ is known. In particular, $\widetilde{u}^+|_{h_\nu} = h_\nu^+$, where $h_\nu^+ = h_\nu/l^+$. For a hydrodynamically smooth wall, where the wall roughness is small compared to l^+, experiments indicate that the outer edge of the viscous sublayer is located at $h_\nu^+ \approx 11$ (based on the intercept between the linear and log components of the law of the wall). We will therefore take $\widetilde{u}^+|_{h_\nu} = h_\nu^+ = 11$. In fact, this intercept is found to be sensitive to pressure gradients and can assume values in the range 10–15 (Nickels 2004). A cubic equation was successfully used in the paper of Nickels (2004) to model this effect; we do not pursue this presently in favor of simplicity, although this generalization should certainly be included for separating flows. Above $z^+ = h_\nu^+$, inviscid outer flow dynamics become important.

4.3.4 Slip Velocity at Lifted Virtual Wall

We now model the mean-flow dynamics in region (II), $h_\nu < z \leq h_0$. We require h_0 to scale with outer flow thickness δ but to remain relatively small, $h_0 < 0.1\,\delta$, say, so that nonuniversal effects (the wake) uncharacteristic of the inner scales can be captured by the LES in region (III). This will permit the LES to be performed with the same grid for a wide range of Re, eliminating the $O(Re_\tau^2)$ scaling requirement for the grid resolution of a partially resolved wall-bounded LES (Piomelli 2008). Put another way, h_0 remains fixed, $O(\delta)$, but h_ν becomes thinner, $O(l^+)$, with increasing Re.

Region (II) is, by construction, the so-called overlap region, or the production-equals-dissipation layer, where the shear stress is approximately constant. Furthermore, the shear stress is balanced by the wall shear stress (Townsend 1976). Casting these ideas in LES terminology,

$$u_\tau^2(x,y,t) = -\widetilde{uw} = -\widetilde{u}\widetilde{w} - T_{xz} = -T_{xz}, \quad \text{since } \widetilde{w} = 0.$$

The existence of quasi-streamwise vortical structures in wall turbulence have long been observed by researchers (e.g., Head and Bandyopadhyay 1981, Robinson 1991), and have also served as useful physical models (e.g., Bakewell and Lumley 1967, Townsend 1976, Perry and Chong 1982, Marušić and Perry 1995, Nickels et al. 2007, Adrian 2007). Motivated by these studies, we model region (II) with an ensemble of vortices aligned in the streamwise direction, $(e_x^v, e_y^v, e_z^v) = (1,0,0) \Leftrightarrow \boldsymbol{e}^v = \boldsymbol{e}_x$. Substituting these into the expression for the shear stress produced by the extended stretched-spiral vortex SGS model, (4.5), and noting that the only nonzero component of the mean velocity gradient tensor is $\mathrm{d}\widetilde{u}/\mathrm{d}z$, we obtain

$$T_{xz} = -\frac{1}{2}\gamma_{\mathrm{II}} K^{1/2} \Delta_c \frac{\mathrm{d}\widetilde{u}}{\mathrm{d}z}. \tag{4.16}$$

Recall the physical mechanism that produces this shear stress: the action of the spiralling streamwise vortex is to wrap its own axial velocity, now identified as the mean streamwise velocity, as if it were a passive scalar (see figure 4.2), thereby transporting higher-momentum fluid toward the wall and transporting low-momentum fluid away from the wall. This process has the observed effect of a flattened streamwise velocity profile.

Unlike the SGS vortices in region (III), which are unaware of the presence of the wall and are, therefore, considered as detached from the wall, the size of these near-wall vortices, Δ_c, are constrained by the presence of the wall so that $\Delta_c = z$. That is, (4.16) with $\Delta_c \to z$ can be interpreted as the shear stress produced by a hierarchy of longitudinal vortices that scale with the wall distance. This scaling assumption is, in fact, the idea of the so-called attached wall eddy (Nickels et al. 2007). We therefore write (4.16) in the form

$$\frac{\mathrm{d}\widetilde{u}}{\mathrm{d}z} = \frac{1}{\mathcal{K}_1}\frac{u_\tau}{z}, \tag{4.17}$$

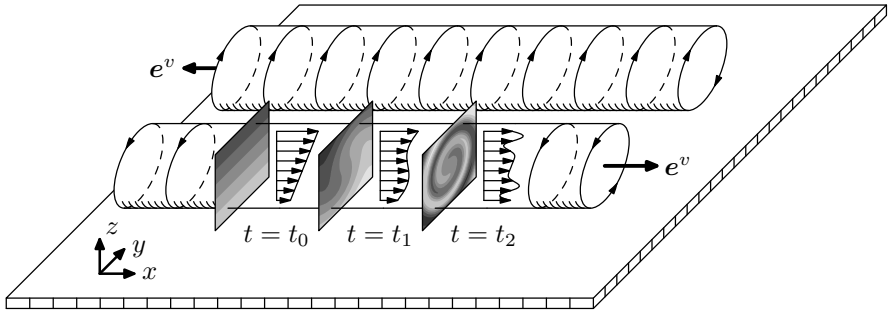

Figure 4.2. Schematic of a pair of attached counterrotating vortices. The winding effect of the vortices are shown on contour plots of the streamwise velocity along with the accompanying profiles. Darker shades represent higher-momentum fluid. The various stages of mixing are characterized by the times $t = t_0 < t_1 < t_2$.

where the dimensionless local quantity given by

$$\mathcal{K}_1(x, y, t) = \frac{\gamma_{\text{II}} K^{1/2}}{2\,(-T_{xz}/u_\tau)} \tag{4.18}$$

resembles the Kármán constant κ. An implicit assumption in the derivation of (4.17) is that K is sensibly independent of z, even though Δ_c decreases as the wall is approached. This is possible if the number of these vortices (population density) also increase in proportion to their decrease in size in order to maintain the same K.

Recall that K is also the SGS kinetic energy of the vortices lying in region (II) and should be obtained from the structure-function-matching procedure local to the vortex location. However, since, by construction, no grid points are placed within region (II), we will use the grid points just inside the LES domain, centered on the plane, $z = h = h_0 + \Delta_z$, for this purpose.

In region (II), we now consider T_{xz} as constant in (4.18) and model this as the geometric average of its value at the true wall and at the top of region (II), so that

$$-T_{xz} = u_\tau \left(- \, T_{xz}|_{\boldsymbol{e}_{\widetilde{S}}} \right)^{1/2}.$$

Hence (4.18) becomes

$$\mathcal{K}_1 = \frac{\gamma_{\text{II}} K^{1/2}}{2 \left(- \, T_{xz}|_{\boldsymbol{e}_{\widetilde{S}}} \right)^{1/2}}. \tag{4.19}$$

Equation (4.19), used in the limit $\kappa_c \to 0$ for increased robustness (to avoid division by small numbers), provides a way to calculate the local Kármán constant. Solving (4.17) in region (II), $h_\nu < z \leq h_0$, and evaluating the result at $z = h_0$ yields

$$\widetilde{u}|_{h_0} = \frac{u_\tau}{\mathcal{K}_1} \log\left(\frac{h_0}{h_\nu}\right) + \widetilde{u}|_{h_\nu} = u_\tau \left(\frac{1}{\mathcal{K}_1} \log\left(\frac{h_0}{h_\nu}\right) + h_\nu^+ \right), \tag{4.20}$$

where the constant of integration has been chosen by putting $\widetilde{u}|_{h_\nu} = u_\tau\, h_\nu^+$. We will use (4.20), which serves as a jump condition between the h_ν–h_0 planes, along with $\widetilde{v} = 0$ and $\widetilde{w} = 0$, to set the Dirichlet boundary conditions at the lifted virtual wall h_0; u_τ is obtained from the solution of (4.15).

Equation (4.20) has been obtained from a physical model of region (II) in which the dominant Reynolds shear stress is modeled by streamwise-aligned vortices that transport low-momentum mean streamwise velocity away from the wall and high-momentum mean streamwise velocity toward the wall. The idea that these self-similar vortices scale only with z—independent of l^+ and δ—implies an overlap argument. Equation (4.20) couples $\widetilde{u}|_{h_0}$ with the resolved-scale LES in region (III), $h_0 < z \leq \delta$, which provides both K and $\boldsymbol{e}_{\widetilde{S}}$. Equation (4.20) contains two constants, γ and h_ν^+. The latter is given empirically by $h_\nu^+ = 11$ from our discussion of region (I); a different value could be used for rough-wall flows. This physical model provides a means of dynamically calculating the instantaneous local "Kármán constant" $\mathcal{K}_1$ as part of the LES. This will be demonstrated later.

It appears from the present construction that we have confined attached eddies to region (II). This is not the case; the existence of attached eddies in region (II) does not preclude their existence in region (III). We have only assumed that region (II) is dominated by attached eddies, which led us to explicitly model their dynamics. If they exist in region (III) and have sizes larger than the grid spacing, $z > \Delta_x$, they would be directly captured by the LES. On the other hand, if they exist in region (III) and have sizes smaller than the grid spacing, $z < \Delta_x$, they would be modeled by the SGS model.

One may also wonder if these attached eddies still exist near the top of region (II), h_0, in very high Reynolds number flows since we designed h_0 to be fixed relative to δ. In the present simulations h_0^+ is as high as 149 k. Note, however, that the attached-eddy idea–that they have size z and have characteristic velocity u_τ–is intimately linked with the overlap argument that says that both z and u_τ are the relevant parameters in the overlap region, $\nu/u_\tau \ll z \ll \delta$. In other words, as long as h_0/δ is small, it does not matter how large h_0^+ is for both z and u_τ to emerge as the relevant parameters, the necessary ingredients for attached eddies.

4.3.5 Estimation of the Mixing Time Constant γ_{II}

A constant, γ_{II}, is required in (4.20). Owing to the highly anisotropic character of near-wall turbulent physics, this is expected to be somewhat different in value from that used in the SGS scalar application (Pullin 2000).

Consider the interface of regions (II) and (III), $z = h_0$, where both inner and outer layer modeling ideas are valid; in the spirit of LES filtering, we interpret this interface as a blurred boundary between the two regions so that the change in underlying vortical flow is gradual. This interface, $z \approx h_0 < 0.1\,\delta$, is near the wall, so the LES filtered flow field can be approximated by simple shear

flow, $\partial\widetilde{u}_i/\partial x_j = \delta_{i1}\delta_{j3}S$, where $S = \mathrm{d}\widetilde{u}/\mathrm{d}z$. This implies that, in this region, $\boldsymbol{e}_{\widetilde{S}} = (1/\sqrt{2}, 0, 1/\sqrt{2})$; that is the detached vortices are inclined at 45° to the wall.

We estimate γ_{II} by matching Townsend's structure parameter,

$$a_1 = T_{13}/T_{ii} = T_{13}/(2K),$$

of the two vortical flow descriptions at this interface region. Given the vortex alignment, this parameter measures the amount of shear stress that can be supported relative to the vortex kinetic energy. First, the $\boldsymbol{e}_{\widetilde{S}}$ alignment and (4.5) give

$$a_1|_{\boldsymbol{e}_{\widetilde{S}}} = (-K|_{\boldsymbol{e}_{\widetilde{S}}}/2)/(2K|_{\boldsymbol{e}_{\widetilde{S}}}) = -1/4.$$

Similarly, the $\boldsymbol{e}_x$ alignment and (4.5) give

$$a_1|_{\boldsymbol{e}_x} = (-\gamma_{\mathrm{II}}(K|_{\boldsymbol{e}_x})^{1/2}\Delta_c S/2)/(2K|_{\boldsymbol{e}_x}) = -\gamma_{\mathrm{II}}\Delta_c S(K|_{\boldsymbol{e}_x})^{-1/2}/4.$$

To proceed, we assume high Re so that $\kappa_c \to 0$. Also, for simplicity, $d \to 0$. The subgrid kinetic energy of the streamwise vortex then reduces to

$$K|_{\boldsymbol{e}_x} = 2\langle(\delta u_i)^2\rangle/\left(\pi^2\langle d^2\rangle\right).$$

The local averaging is dominated by the background shear, so we can approximate $\langle(\delta\widetilde{u}_i)^2\rangle \approx \langle(\delta\widetilde{u})^2\rangle \approx (\Delta_z S)^2$, and for the same reason $\langle d^2\rangle = (\Delta_z/\Delta_c)^2$. Then

$$K|_{\boldsymbol{e}_x} = 2\left(\Delta_c S/\pi\right)^2.$$

Using this, we obtain a_1 for the $\boldsymbol{e}_x$ aligned vortex,

$$a_1|_{\boldsymbol{e}_x} = -2^{-5/2}\,\pi\,\gamma_{\mathrm{II}}.$$

Finally, matching these, $a_1|_{\boldsymbol{e}_{\widetilde{S}}} = a_1|_{\boldsymbol{e}_x}$, we have $\gamma_{\mathrm{II}} = 2^{1/2}/\pi \approx 0.45$. This is the value used presently for all LES.

4.3.6 Summary of SGS Wall Model

Our SGS model for the near-wall dynamics can be summarized as follows: for every cell adjacent to both the top and bottom walls, (4.15) is solved for η_0 with terms on the right-hand side provided by the LES at the top of the wall-adjacent cell at $z = h = \Delta_z + h_0$. This provides $\eta_0(x, y, t)$ and thus $u_\tau(x, y, t)$. Equation (4.20) is then used to evaluate the streamwise slip velocity $\widetilde{u}|_{h_0}(x, y, t)$ at

$z = h_0$, with $\mathcal{K}_1$ evaluated from (4.19) and with K and $T_{xz}|_{\boldsymbol{e}_{\widetilde{S}}}$ evaluated at $z = h = \Delta_z + h_0$ from the LES structure-function-matching procedure. The other boundary conditions at the virtual wall are taken as $\widetilde{v}|_{h_0}(x, y, t) = \widetilde{w}|_{h_0}(x, y, t) = 0$. This method couples the LES with the modeled, near-wall dynamics. The LES has implicit knowledge of the true no-slip boundary condition, because this was used in obtaining (4.15), and the smooth-wall condition through use of $h_\nu^+ = 11$. Because the LES quantities in both (4.15) and (4.19) are evaluated at the top of the first cell at $z = h = \Delta_z + h_0$, the height of the virtual wall at $z = h_0$ should satisfy $h_\nu < h_0 < h$. Presently we use $h_0 = 0.18\,\Delta_z$, independent of the LES resolution, and consider this as part of the overall grid. Some tests to investigate sensitivity to h_0 were performed.

4.4 Numerical Method

The low-storage third-order semi-implicit Runge–Kutta method of Spalart, Moser and Rogers (1991) is used for temporal discretization. The implicit treatment of the viscous term allows large time steps to be taken; in the simulations, the CFL number

$$\Delta_t \max\left(\frac{|u|}{\Delta_x}, \frac{|v|}{\Delta_y}, \frac{|w|}{\Delta_z}\right)$$

was set to unity. The low-storage property simplifies the time step advancement into three sequential substeps, $n = 0, 1, 2$, of the same form:

$$\frac{\widetilde{u}_i^{(n+1)} - \widetilde{u}_i^{(n)}}{\Delta_t} = -(\gamma_n + \zeta_n)\frac{\partial \widetilde{p}^{(n+1)}}{\partial x_i} + \gamma_n H_i^{(n)} + \zeta_n H_i^{(n-1)} + \alpha_n L_i^{(n)} + \beta_n L_i^{(n+1)}, \quad (4.21a)$$

$$\frac{\partial \widetilde{u}_i^{(n+1)}}{\partial x_i} = 0, \quad (4.21b)$$

$$H_i = -\frac{1}{2}\left(\frac{\partial \widetilde{u}_i \widetilde{u}_j}{\partial x_j} + \widetilde{u}_j \frac{\partial \widetilde{u}_i}{\partial x_j}\right) - \frac{\partial T_{ij}}{\partial x_j} + f_i, \quad L_i = \nu \frac{\partial^2 \widetilde{u}_i}{\partial x_j^2}. \quad (4.21c)$$

For an arbitrary reference time, t_0, $\widetilde{u}_i^{(3)} = \widetilde{u}_i(t_0 + \Delta_t)$. The value of the constants α_n, β_n, γ_n and ζ_n are given by Spalart, Moser and Rogers (1991). The discrete pressure $\widetilde{p}^{(n+1)}$ is formally a Lagrange multiplier that enforces (4.21b), including at the boundary.

The governing equations are solved in an $L_x \times L_y \times L_z$ box with periodic boundary conditions applied in both the x- and y-directions. Applying the Fourier spectral method for both these directions results in $N_x \times N_y$ sets of one-dimensional complex Helmholtz equations in the z-direction for each mode (k_x, k_y), where

$$\begin{aligned} k_x &= 2\pi/L_x(-N_x/2, \ldots, -1, 0, 1, \ldots, N_x/2 - 1), \\ k_y &= 2\pi/L_y(-N_y/2, \ldots, -1, 0, 1, \ldots, N_y/2 - 1). \end{aligned}$$

In practice, only half of the $N_x \times N_y$ sets of complex equations (or $N_x \times N_y$ sets of real equations, separately counting real and imaginary parts) are solved due to the symmetry of the Fourier coefficients.

An explicit finite difference scheme with fourth-order global accuracy (third-order boundary, sixth-order interior) is used to approximate the z derivative on $N_z + 1$ uniformly spaced nodes, located at $z_k = L_z(-1/2 + k/N_z)$, $k = 0, 1, \ldots, N_z$. When coupled with a certain diagonal norm, the finite-difference approximation satisfies the summation-by-parts (SBP) property (Strand 1994, Carpenter, Gottlieb and Abarbanel 1994, Mattsson and Nordström 2004). Although stability in the sense described in those papers is not preserved because Dirichlet boundary conditions are applied directly (injection method), our experience indicates that stability is not an issue, at least presently, where the diffusion operator is advanced implicitly. In explicit schemes, a seven-point stencil is required to achieve sixth-order accuracy, but, following Hill and Pullin (2004), we use two additional points to minimize the Ghosal truncation error (Ghosal 1996). The Ghosal truncation error pertains to errors resulting from the application of spatial discretization schemes to the Navier–Stokes equations. Unsurprisingly, in reducing the Ghosal truncation error, the high-wavenumber performance of the finite-difference scheme is also simultaneously improved (Hill and Pullin 2004). Such a scheme, called a tuned centered-difference (TCD) method by Hill and Pullin (2004), is also combined with the SBP scheme in Pantano et al. (2007). Complete details of the $N_z + 1 \times N_z + 1$ finite-difference matrix D_z are provided in § 4.4.1.

Spatially discretizing (4.21), we obtain for each mode (k_x, k_y) and node z_k:

$$\left.\begin{aligned} \left(D_z^2 - \lambda^2\right)\widehat{u} &= \mathrm{i}k_x\zeta'\widehat{p} + R_1 + \sigma_1, \\ \left(D_z^2 - \lambda^2\right)\widehat{v} &= \mathrm{i}k_y\zeta'\widehat{p} + R_2 + \sigma_2, \\ \left(D_z^2 - \lambda^2\right)\widehat{w} &= D_z\zeta'\widehat{p} + R_3 + \sigma_3, \end{aligned}\right\} \tag{4.22a}$$

$$\mathrm{i}k_x\widehat{u} + \mathrm{i}k_y\widehat{v} + D_z\widehat{w} = 0, \tag{4.22b}$$

where $\lambda^2 = k_x^2 + k_y^2 + 1/(\beta\nu\Delta_t)$ and $\zeta' = (\gamma+\zeta)/(\beta\nu)$. The spatial discretization of $(\boldsymbol{u}, p)^{(n+1)}(x, y, z)$ is denoted $(\widehat{\boldsymbol{u}}, \widehat{p})(k_x, k_y, k)$. For clarity, we have dropped the superscript and subscript n from (4.21); R_i are known terms, obtained by simple rearrangement; σ_i are incurred penalty terms for directly imposing Dirichlet boundary conditions on the velocity at $k = 0$ and $k = N_z$ (or equivalently, at $z = \pm L_z/2$),

$$\left.\begin{aligned} (\widehat{u}, \widehat{v}, \widehat{w})(k_x, k_y, 0) &= (\widehat{g_1}^-, \widehat{g_2}^-, \widehat{g_3}^-)(k_x, k_y), \\ (\widehat{u}, \widehat{v}, \widehat{w})(k_x, k_y, N_z) &= (\widehat{g_1}^+, \widehat{g_2}^+, \widehat{g_3}^+)(k_x, k_y). \end{aligned}\right\} \tag{4.23}$$

In other words, because we choose to satisfy (4.23), (4.22) written without σ_i cannot be satisfied at $k = 0$ and $k = N_z$. Although we call σ_i a penalty term, it should not be confused with the simultaneous-approximation-term (SAT) technique (Carpenter, Gottlieb and Abarbanel 1994),

where σ_i is explicitly specified. Here, σ_i must be determined as part of the solution procedure. Note, however, that the divergence constraint, (4.22 b), is satisfied everywhere, even at the boundaries, $k = 0$ and $k = N_z$.

The discrete pressure Poisson equation is obtained by applying the discrete divergence to the momentum equations:

$$\left(D_z^2 - \left[k_x^2 + k_y^2\right]\right)\zeta'\widehat{p} = -R_p - \left(\mathrm{i}k_x\sigma_1 + \mathrm{i}k_y\sigma_2 + D_z\sigma_3\right), \tag{4.24}$$

where $R_p = \mathrm{i}k_xR_1 + \mathrm{i}k_yR_2 + D_zR_3$. In general, $D_z\sigma_3$ is nonzero in the interior of the domain, $k = 1, 2, \ldots, N_z - 1$. That is σ_i, appearing only at the boundaries of (4.22 a) carry over as additional interior source terms to (4.24). Careful accounting of the σ_i terms is key to ensuring discrete mass conservation up to machine precision. Unlike in well-resolved simulations such as DNS in which σ_i is small and can thus be safely ignored, σ_i in LES is large and if ignored will be a source of nonzero velocity divergence that leads to numerical instability (Canuto et al. 1987). The method for solving this coupled problem in the discrete framework is the Kleiser–Schumann influence-matrix method, detailed by Canuto et al. (1987). Although they presented it for the Chebyshev-tau and spectral collocation discretizations with homogeneous boundary conditions, the method is quite general, and we extend its usage here for finite differences with nonhomogeneous boundary conditions.

As written, the nonlinear products in (4.21 c) are computed in skew-symmetric form in physical space. Then, H_i, which includes the nonlinear products and the LES contributions, is transformed to wavenumber space, where a p_1th-order Fourier exponential filter (Gottlieb and Shu 1997, Hou and Li 2007) of the form

$$\sigma(\xi) = \exp(-\alpha_1\xi^{p_1}) \tag{4.25}$$

is applied in the periodic directions, $\xi = |k_x|/(\pi/\Delta_x), |k_y|/(\pi/\Delta_y)$; $p_1 = 36$; α_1 is chosen so that $\sigma(2/3) = 1/2$. The high-order filter, with flat response at resolved wavenumbers and sharp but smooth drop at the cutoff wavenumber, mimics the 2/3-dealiasing rule. In an LES employing a local physical-space SGS model, the filter's smooth cutoff minimizes Gibbs oscillations that, posing as steep local gradients, would artificially activate the SGS model.

The set of ODEs, (4.15) for the wall shear stress, $\tau_0(x, y, t) = \nu\eta_0(x, y, t)$, are advanced using the same third-order Runge–Kutta scheme as the main part of the flow simulation. The overall computing overhead for the implementation of the stretched-vortex SGS model is less than 10% of the overall computing time. Because the numerical solution of the wall ODE set occurs only in boundary cells, this constitutes a small part of the SGS-related computing effort.

4.4.1 SBP TCD Derivative Matrix

We provide details of the fourth-order globally accurate explicit finite-difference $N_z + 1 \times N_z + 1$ matrix, D_z. This matrix operates on any $N_z + 1$ vector, u, say, whose elements u_k represent nodal discretizations of the continuous function $u(z)$ at uniformly spaced nodes, $z_k = -L_z/2 + k\Delta_z$, $\Delta_z = L_z/N_z$ $k = 0, 1, \ldots, N_z$, such that $u(z_k) = u_k$. SBP operators (Strand 1994, Mattsson and Nordström 2004) are constructed from the following decomposition:

$$D_z = \frac{1}{\Delta_z} H^{-1} Q, \quad Q + Q^T = B, \quad B = \mathrm{diag}(-1, 0, \ldots, 0, 1); \tag{4.26a,b,c}$$

$H = H^T > 0$ and is used to define an inner product, $(u, u)_H = u^T H u$, which, in turn, defines a norm on u, given by $||u||_H^2 = (u, u)_H$. Although many possible choices for such H exist, we will only consider the diagonal norm,

$$H = \mathrm{diag}(h_0, h_1, \ldots, h_{N_z}), \tag{4.27}$$

which restricts the order of accuracy of the boundary scheme to at most half the order of accuracy of the interior scheme (Strand 1994). Although not pursued presently, an SBP scheme with diagonal norm can be easily generalized to apply on arbitrarily mapped grids by absorbing the scaling factors into H. Presently, a third-order boundary scheme coupled with a sixth-order interior scheme, equivalent to a fourth-order global scheme, is chosen. The boundary scheme covers the finite-difference approximation for the first and last six points, $k = 0, 1, \ldots, 5, N_z - 5, N_z - 4, \ldots, N_z$, while the interior scheme covers the rest, $k = 6, 7, \ldots, N_z - 6$.

The sixth-order TCD (Hill and Pullin 2004), which has a wider nine-point stencil, is used as the interior scheme. The extra degree of freedom is used to improve spectral resolution by reducing truncation errors inherent in the Navier–Stokes equations. Any nine-point sixth-order centered difference approximation for the derivative is given by

$$D_z u_k = \frac{1}{\Delta_z} \sum_{j=0}^{4} d_j \left(u_{k+j} - u_{k-j} \right), \tag{4.28}$$

where $d_0 = 0$; $d_1 = 3/4 - 14d_4$; $d_2 = -3/20 + 14d_4$; $d_3 = 1/60 - 6d_4$; and d_4 is the free parameter. Setting $d_4 = 0$ recovers the standard sixth-order explicit scheme; setting $d_4 = -1/280$ recovers the standard eighth-order explicit scheme; d_4 is determined by minimizing the Ghosal truncation error (Ghosal 1996), a procedure detailed by Hill and Pullin (2004). Here, we only give the final result: $d_4 = -0.0166$.

Comparing (4.26a), (4.27) and (4.28), we identify the TCD scheme in the context of the SBP

operator as

$$h_k = 1, \quad Q_{kj} = \begin{cases} d_{j-k}, & 0 \le j-k \le 4, \\ -d_{k-j}, & 0 < k-j \le 4, \\ 0, & \text{otherwise}, \end{cases} \tag{4.29a,b}$$

for $k = 6, 7, \ldots, N_z - 6$.

To determine the boundary scheme, write (4.26a) and (4.27) explicitly for $k = 0, 1, \ldots, 5$:

$$h_k(\Delta_z)(D_z u)_k = \sum_{j=0}^{10} Q_{kj} u_j = \sum_{j=0}^{5} Q_{kj} u_j + \sum_{j=6}^{10} Q_{kj} u_j. \tag{4.30}$$

The second term on the right-hand side is known from using (4.26b) and (4.29):

$$Q_{kj} = -Q_{jk} = -(-d_{j-k}) = d_{j-k}$$

for $k = 0, 1, \ldots, 5$, $j = 6, 7, \ldots, 10$, $0 < j - k \le 4$. Substituting this in (4.30) gives

$$h_k(\Delta_z)(D_z u)_k = \sum_{j=0}^{5} Q_{kj} u_j + \sum_{j=6}^{k+4} d_{j-k} u_j. \tag{4.31}$$

The remaining unknowns to be solved are the 6×6 block, Q_{kj} $(k, j = 0, 1, \ldots, 5)$ and the six-element vector h_k $(k = 0, 1, \ldots, 5)$. For each k, match the coefficients from the series expansion of (4.31) up to $(\Delta_z)^3$ and apply (4.26b) to determine the remaining unknowns up to a another free parameter, Q_{45}, say, different from d_4 (see Strand 1994). We choose Q_{45} by minimizing the so-called average boundary truncation error (Diener et al. 2007), giving $Q_{45} = (17\,171 - 329\,670 d_4)/24\,300$.

4.4.2 Code Validation

To validate our code, we reproduced the $Re_\tau = 180$ DNS of Kim, Moin and Moser (1987) using $L_x \times L_y \times L_z = 2\pi\delta \times 4\pi\delta/3 \times 2\delta$ and $N_x \times N_y \times N_z = 192 \times 192 \times 192$. The main difference between these two codes is the discretization scheme in the wall-normal direction: Kim, Moin and Moser (1987) used a Chebyshev-tau scheme on a stretched–cosine grid, while we used a fourth-order finite-difference scheme on a uniformly spaced grid. The statistics from the present code are taken at a snapshot in time. As seen in figures 4.3 and 4.4, these are in good agreement with Kim, Moin and Moser (1987).

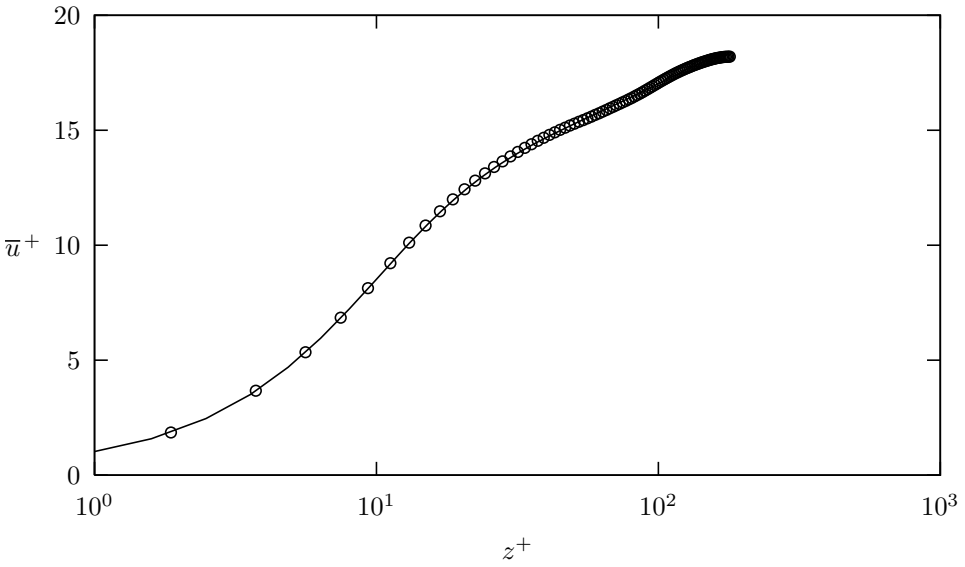

Figure 4.3. Mean velocity profile from $Re_\tau = 180$ DNS: ∘ , present code; —— , Kim, Moin and Moser (1987).

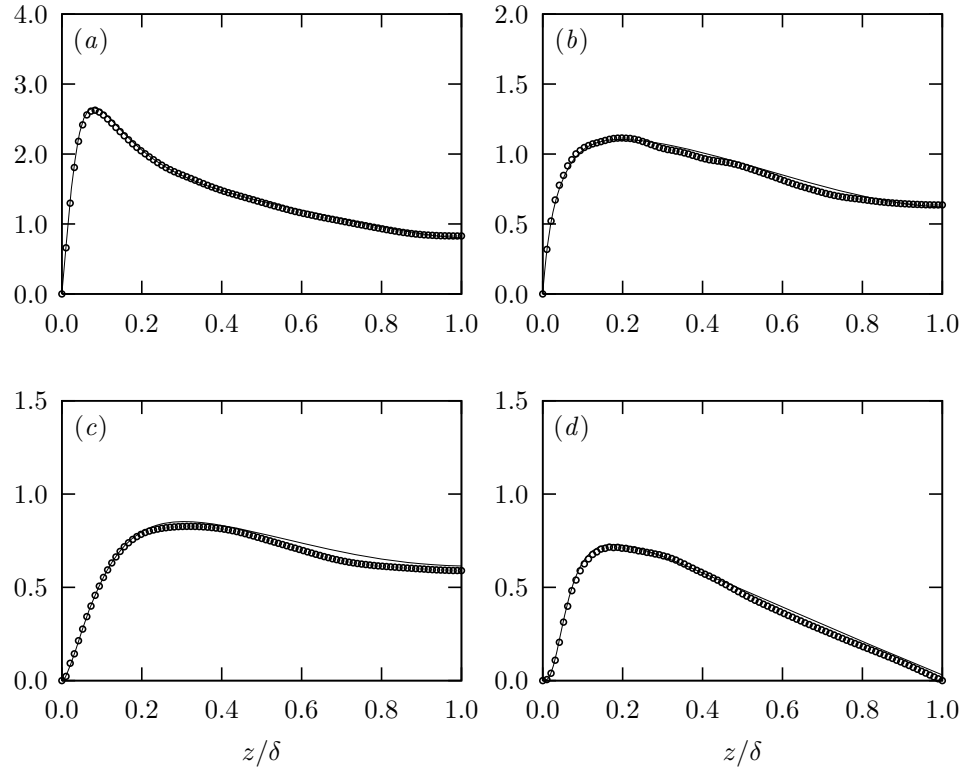

Figure 4.4. Turbulence statistics, (a) u^+_{rms}, (b) v^+_{rms}, (c) w^+_{rms} and (d) $-\overline{uw}^+$ from $Re_\tau = 180$ DNS: ∘ , present code; —— , Kim, Moin and Moser (1987).

Table 4.1. LES parameters and outputs for turbulent channel flow.

Case	Re_c	Re_τ	$\eta(\%)$	L_x/δ'	L_y/δ'	h_0/Δ_z	N_x	N_y	N_z	Δ_x^+	$\gamma_{\rm III}$	$\overline{\mathcal{K}}_1$
A1	49 k	2 k	1.1	32	8	0.18	192	48	48	3.3×10^2	0	0.37
A2	610 k	20 k	2.2	32	8	0.18	192	48	48	3.3×10^3	0	0.38
A3	7400 k	200 k	2.9	32	8	0.18	192	48	48	3.3×10^4	0	0.38
A4	87 M	2 M	2.1	32	8	0.18	192	48	48	3.3×10^5	0	0.37
A5	990 M	20 M	1.7	32	8	0.18	192	48	48	3.3×10^6	0	0.37
B2	610 k	20 k	2.9	32	8	0.18	384	96	96	1.7×10^3	0	0.38
B3	7400 k	200 k	2.7	32	8	0.18	384	96	96	1.7×10^4	0	0.38
B4	86 M	2 M	2.2	32	8	0.18	384	96	96	1.7×10^5	0	0.38
C2	580 k	20 k	3.6	32	8	0.18	192	48	48	3.3×10^3	0.45	0.39
C3	6900 k	200 k	1.0	32	8	0.18	192	48	48	3.3×10^4	0.45	0.40
C4	81 M	2 M	−0.4	32	8	0.18	192	48	48	3.3×10^5	0.45	0.39
F2	620 k	20 k	−0.8	32	8	0.36	192	48	48	3.3×10^3	0	0.38
F3	7600 k	200 k	0.6	32	8	0.36	192	48	48	3.3×10^4	0	0.38
F4	89 M	2 M	0.8	32	8	0.36	192	48	48	3.3×10^5	0	0.38

4.5 Results and Discussion

The LES presently performed are summarized in table 4.1: k $\equiv 10^3$, M $\equiv 10^6$; $Re_c \equiv u_c\delta/\nu$; u_c is the mean centerline velocity; $Re_\tau \equiv u_\tau\delta/\nu$; $\eta \equiv (Re_\tau)_{act}/Re_\tau - 1$; $\delta' \equiv L_z/2 = \delta - h_0 \approx \delta$; $\Delta_x = \Delta_y = 4\Delta_z$; Re_τ is nominal, $(Re_\tau)_{act}$ is actual; and $\gamma_{\rm III}$ refers to γ in (4.5) used in the interior of the LES domain. Four sets were done and are labeled A, B, C and D. All used the same form of the wall SGS model with $\gamma_{\rm II} = 0.45$. For sets A and B, the original form of the stretched-vortex SGS model was used in region (III). This corresponds to $\gamma_{\rm III} = 0$ in (4.5). For set C, $\gamma_{\rm III} = 0.45$ was used in (4.5). There is no inconsistency with $\gamma_{\rm II} \neq \gamma_{\rm III}$: the former is a necessary part of the special SGS model in region (II), while the latter forms part of the global SGS model for LES in region (III). Set F is used to evaluate the wall model's sensitivity to the virtual wall location h_0. The simulations are run until the first- and second-order statistics have converged. Data is then collected from one snapshot in time; our interest is in low-order statistics, which do not benefit significantly from time averaging.

4.5.1 Profiles

The mean streamwise velocity profiles for $Re_\tau = 2\,$k–$20\,$M (set A) corresponding to the original LES model ($\gamma_{\rm III} = 0$) coupled with the present wall model are shown in figure 4.5, where $\overline{(\ )}$ denotes the xy-plane average at a particular time. Also shown is the log relationship (4.20) with the predicted $\overline{\mathcal{K}}_1$ averaged across all cases, $(\overline{\mathcal{K}}_1)_{avg} = 0.37$. Its intercept is $11 - \log(11)/0.37 = 4.5$ (compare with the classic value of ~ 5). The slight drop in the mean-flow profile for the two points adjacent to

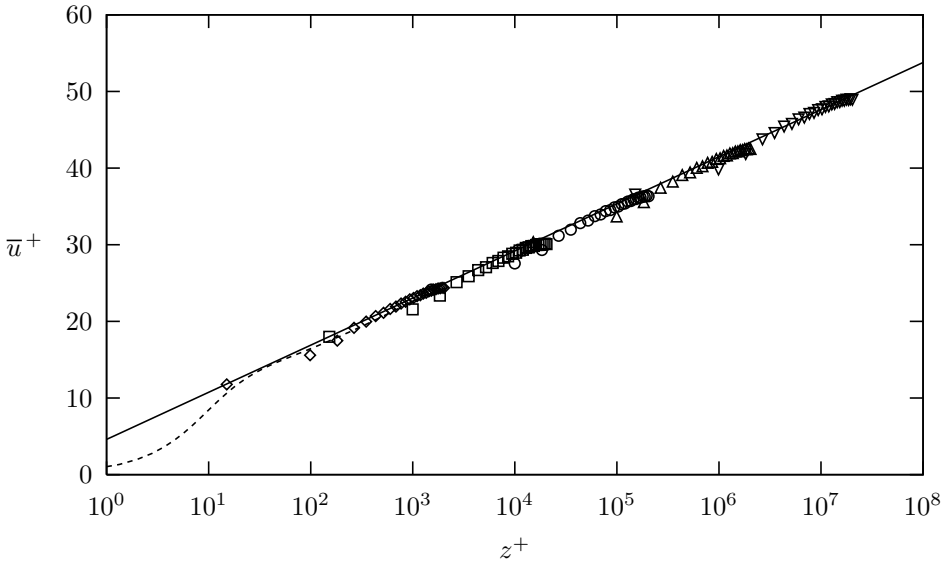

Figure 4.5. Mean velocity profiles for LES with $\gamma_{\mathrm{III}} = 0$ (set A): $\diamond$, $Re_\tau = 2\,\mathrm{k}$; $\square$, $Re_\tau = 20\,\mathrm{k}$; $\circ$, $Re_\tau = 200\,\mathrm{k}$; $\triangle$, $Re_\tau = 2\,\mathrm{M}$; $\triangledown$, $Re_\tau = 20\,\mathrm{M}$; ---- , $Re_\tau = 2\,\mathrm{k}$ DNS (Hoyas and Jiménez 2006); ——— , $\log(z^+/11)/0.37 + 11$.

the lifted virtual wall was thought to be a manifestation of a spurious sublayer due to the Dirichlet slip and no-transpiration boundary conditions (Cabot and Moin 1999). This issue is not specific to Dirichlet boundary conditions but can also be observed in wall stress boundary conditions (see Pantano et al. 2008). The flow quickly recovers beyond the two points and appears to follow the log profile.

We plot the corresponding profiles of the turbulent statistics in figure 4.6, where $(\,)_{rms}$ refers to the root mean square (r.m.s.) of the fluctuations. The mild near-wall oscillations may suggest that we used an inadequate time-averaging interval. However, the localized nature of these oscillations and similar observations by Pantano et al. (2008) offer the explanation that they are, in fact, Gibbs oscillations caused by the singular no-penetration boundary condition.

Recently, the peak in near-wall u-fluctuations was observed to be mildly increasing with Reynolds number (DeGraaff and Eaton 2000, Del Álamo et al. 2004). This peak, located at $z^+ \approx 12$, is beneath our lifted wall, $z = h_0$, and well within our modeled near-wall layer consisting of streamwise vortices—region (II). Accordingly, we do not expect to capture this trend with statistics of the present simulations, which are essentially an outer-layer—region (III)—LES. This is a limitation of the present wall model.

The w-fluctuations are uniformly underpredicted; this is not surprising, since we used the no-transpiration boundary condition, which does not strictly hold at the lifted virtual wall. This amounts to letting the LES SGS model predict all near-wall w-fluctuations, as confirmed by the subgrid component in figure 4.6(c). The overall anisotropy in the Reynolds stresses, however, is preserved by our anisotropic LES model, even close to the wall. Physically, we are letting the LES

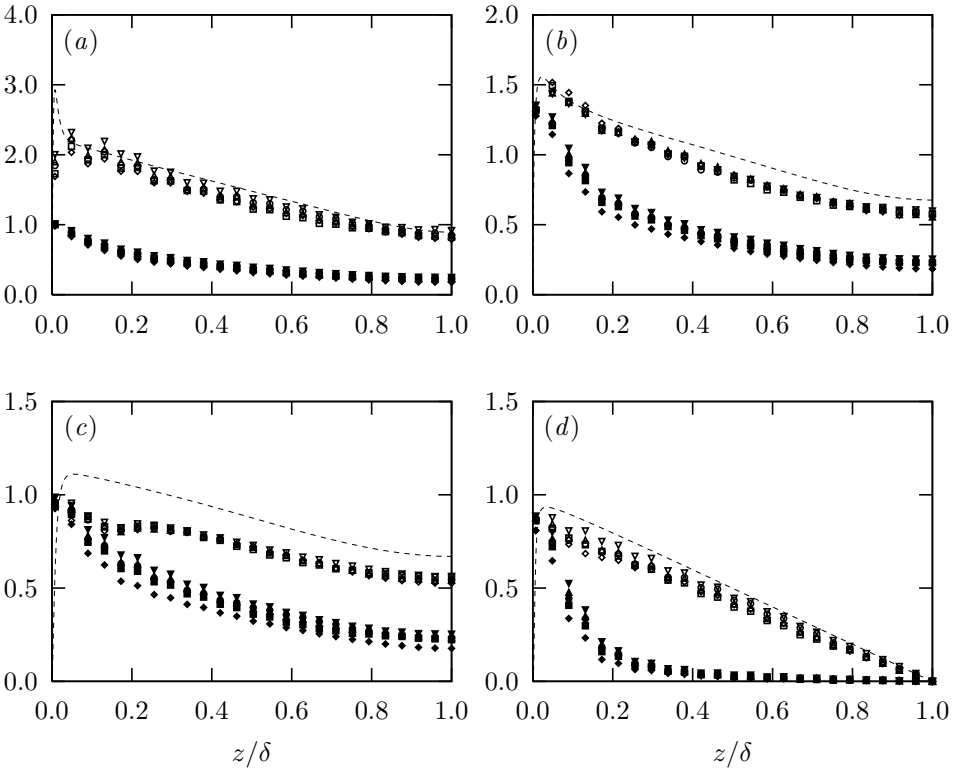

Figure 4.6. Turbulence statistics, (a) u^+_{rms}, (b) v^+_{rms}, (c) w^+_{rms} and (d) $-\overline{uw}^+$, for LES with $\gamma_{\rm III} = 0$ (set A): $\diamond$, $Re_\tau = 2\,\mathrm{k}$; $\square$, $Re_\tau = 20\,\mathrm{k}$; $\circ$, $Re_\tau = 200\,\mathrm{k}$; $\triangle$, $Re_\tau = 2\,\mathrm{M}$; $\triangledown$, $Re_\tau = 20\,\mathrm{M}$; – – – – , $Re_\tau = 2\,\mathrm{k}$ DNS (Hoyas and Jiménez 2006); open symbols, total (resolved plus subgrid); solid symbols, subgrid.

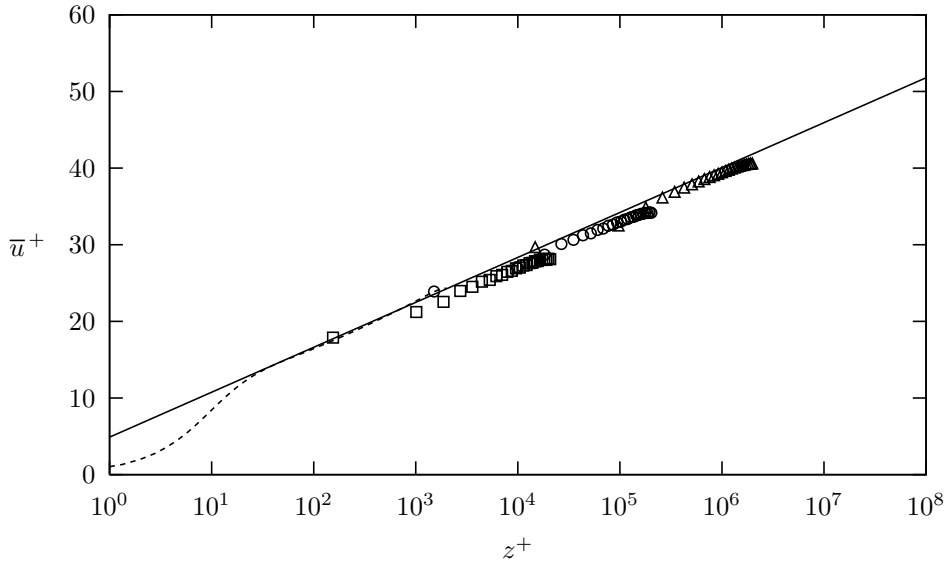

Figure 4.7. Mean velocity profiles for LES with $\gamma_{\rm III} = 0.45$ (set C): ▫ , $Re_\tau = 20\,\mathrm{k}$; ∘ , $Re_\tau = 200\,\mathrm{k}$; △ , $Re_\tau = 2\,\mathrm{M}$; - - - - , $Re_\tau = 2\,\mathrm{k}$ DNS (Hoyas and Jiménez 2006); ——— , $\log(z^+/11)/0.39 + 11$.

model do the work of modeling the near-wall "large eddies", since these, constrained by the wall, become part of the near-wall subgrid motion. This capability of the stretched-spiral vortex SGS model is also clearly shown by Pantano et al. (2008).

Near the wall $-\overline{uw}^+$ is slightly smaller than unity (see figure 4.6(d)), indicating a small imbalance between $-\overline{uw}$, as determined by the LES SGS model, and $\overline{u_\tau^2} = \overline{\nu\eta_0}$, as determined by the ODE for η_0. To understand this, we set $\partial/\partial t = 0$ in the ODE (4.15), solve for $\nu\eta_0$ and then take the plane average to reveal that this imbalance is caused by a nonvanishing plane average of $\partial\widetilde{uu}|_h/\partial x$ and $\partial\widetilde{uv}|_h/\partial y$, as these are numerically calculated in the skew-symmetric form. Similar trends in mean profiles and turbulence statistics are observed (not shown) when the resolution is doubled in all directions (set B).

The mean streamwise velocity profiles for $Re_\tau = 20\,\mathrm{k}$–$2\,\mathrm{M}$ (set C) that are LES performed with the extended form for T_{ij} given by (4.5) and $\gamma_{\rm III} = 0.45$ slightly underpredict the logarithmic relationship (see figure 4.7). The average of the predicted Kármán constant is 0.39. The corresponding turbulent statistics are shown in figure 4.8. For these cases, the near-wall w-fluctuations are underpredicted (see figure 4.8(c)).

For LES with $\gamma_{\rm III} = 0$ (sets A and B), we plot the subgrid kinetic energy fraction, $\overline{K}_{sgs}/(\overline{K}_{res} + \overline{K}_{sgs})$, where $K_{res} = \widetilde{u}_i\widetilde{u}_i/2$ and $K_{sgs} = T_{ii}/2 = K$, in figure 4.9. Near the channel center, the LES SGS model behaves in the classical LES view, where it carries roughly 10%–20% of the overall kinetic energy. This, however, is reversed near the wall, independent of Re_τ and resolution (compare figures 4.9(a) and 4.9(b)).

A feature of our wall model is its ability to predict the local Kármán constant, $\mathcal{K}_1$. Its p.d.f. in

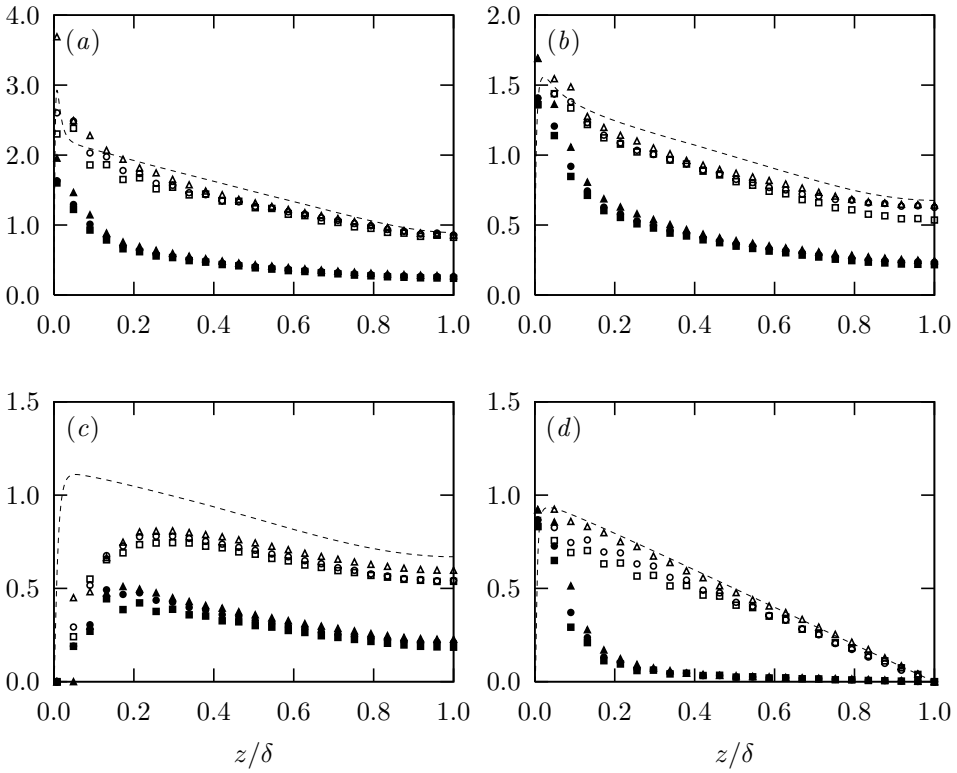

Figure 4.8. Turbulence statistics, (a) u^+_{rms}, (b) v^+_{rms}, (c) w^+_{rms} and (d) $-\overline{uw}^+$, for LES with $\gamma_{\rm III} = 0.45$ (set C): ▫ , $Re_\tau = 20\,\mathrm{k}$; ○ , $Re_\tau = 200\,\mathrm{k}$; △ , $Re_\tau = 2\,\mathrm{M}$; ---- , $Re_\tau = 2\,\mathrm{k}$ DNS (Hoyas and Jiménez 2006); open symbols, total (resolved plus subgrid); solid symbols, subgrid.

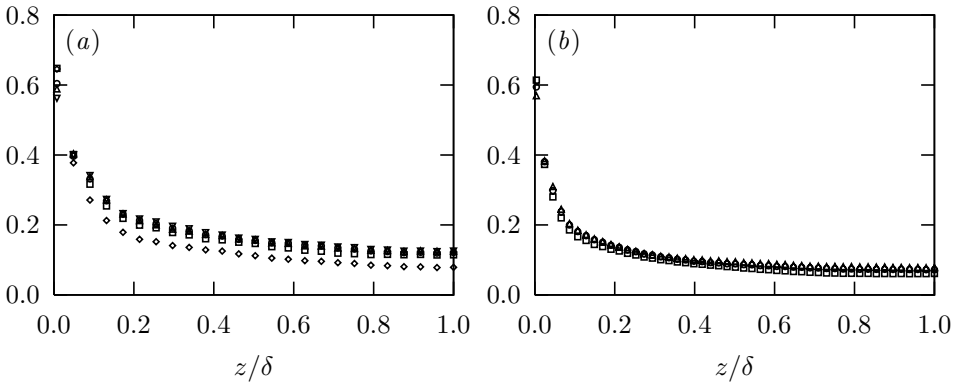

Figure 4.9. The subgrid kinetic energy fraction $\overline{K}_{sgs}/(\overline{K}_{res} + \overline{K}_{sgs})$ with (a) coarse resolution (set A), and (b) fine resolution (set B): ◇ , $Re_\tau = 2\,\mathrm{k}$; ▫ , $Re_\tau = 20\,\mathrm{k}$; ○ , $Re_\tau = 200\,\mathrm{k}$; △ , $Re_\tau = 2\,\mathrm{M}$; ▽ , $Re_\tau = 20\,\mathrm{M}$.

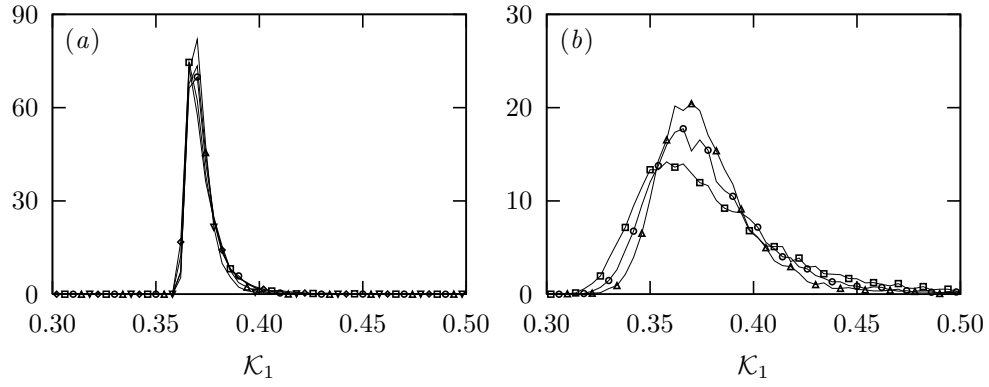

Figure 4.10. P.d.f.s of the predicted Kármán constant, $\mathcal{K}_1$, for LES with (a) $\gamma_{\rm III} = 0$ (set A), $(\overline{\mathcal{K}}_1)_{avg} = 0.37$ and (b) $\gamma_{\rm III} = 0.45$ (set C), $(\overline{\mathcal{K}}_1)_{avg} = 0.39$: $\diamond$, $Re_\tau = 2\,\mathrm{k}$; $\square$, $Re_\tau = 20\,\mathrm{k}$; $\circ$, $Re_\tau = 200\,\mathrm{k}$; $\triangle$, $Re_\tau = 2\,\mathrm{M}$; $\triangledown$, $Re_\tau = 20\,\mathrm{M}$.

figure 4.10 shows peak values around 0.38, with a wider distribution for the cases with $\gamma_{\rm III} = 0.45$. The notion of variable $\mathcal{K}_1$ was also suggested by Nickels (2004), who found that $\mathcal{K}_1$ could also be sensitive to pressure gradients. This is consistent with the present modeling approach, where all local wall-adjacent cells are subjected to outer flow forcing with pressure gradients and should therefore have their own $\mathcal{K}_1$, although their average $\overline{\mathcal{K}}_1$ should agree with experiments or DNS data.

Figure 4.11 shows that the mean velocity profiles are not very sensitive to a doubling of the virtual wall location, h_0, from $h_0 = 0.18\,\Delta_z$ to $h_0 = 0.36\,\Delta_z$, We found some sensitivity when h_0 was decreased below $0.1\,\Delta_z$ and this is not recommended. With $\zeta_0 \equiv h_0/\Delta_z$ and $\Delta_z = L_z/N_z$, $\delta = L_z/2 + h_0$, we have, in inner variables, $h_0^+ = 2\zeta_0 Re_\tau/(N_z + 2\zeta_0)$. We require that $h_0^+ > h_\nu^+ = 11$. This is satisfied always presently. We note that for $Re_\tau = 2\,\mathrm{k}$, this is not satisfied with $N = 96$, and these runs were done only with $N = 48$ for which $h_0^+ \approx 15$ with $\zeta_0 = 0.18$.

4.5.2 Resolved-Scale Spectra

The one-dimensional power spectra of streamwise velocity fluctuations, E_{uu}, at the quarter-channel height $z/\delta = 0.5$ is shown in figure 4.12. We adopt the following convention

$$u_{rms}^2 = \int_0^\infty E_{uu}(k_x)\,\mathrm{d}k_x = \int_0^\infty E_{uu}(k_y)\,\mathrm{d}k_y.$$

The plots are normalized with the plane-averaged Kolmogorov scales $\overline{\epsilon}$ and ν, where the total dissipation $\epsilon = \epsilon_{res} + \epsilon_{sgs}$, the resolved dissipation $\epsilon_{res} = 2\nu\widetilde{S}_{ij}\widetilde{S}_{ij}$ and the subgrid dissipation $\epsilon_{sgs} = \int_{k_c}^\infty 2\nu k^2 E(k)\,\mathrm{d}k$. For reference, $\overline{K}_{sgs}/(\overline{K}_{res} + \overline{K}_{sgs}) \lesssim 0.2$ at this wall-normal plane (figure 4.9(a)). Also in figure 4.12 are model spectra (Pope 2000, figure 6.14) that fit data from nearly two decades (30–1500) of Taylor-scale Reynolds numbers, as compiled by Saddoughi and Veeravalli (1994). To reproduce the model spectra of Pope (2000), we use the parameters $\overline{\epsilon}$, ν and the isotropic

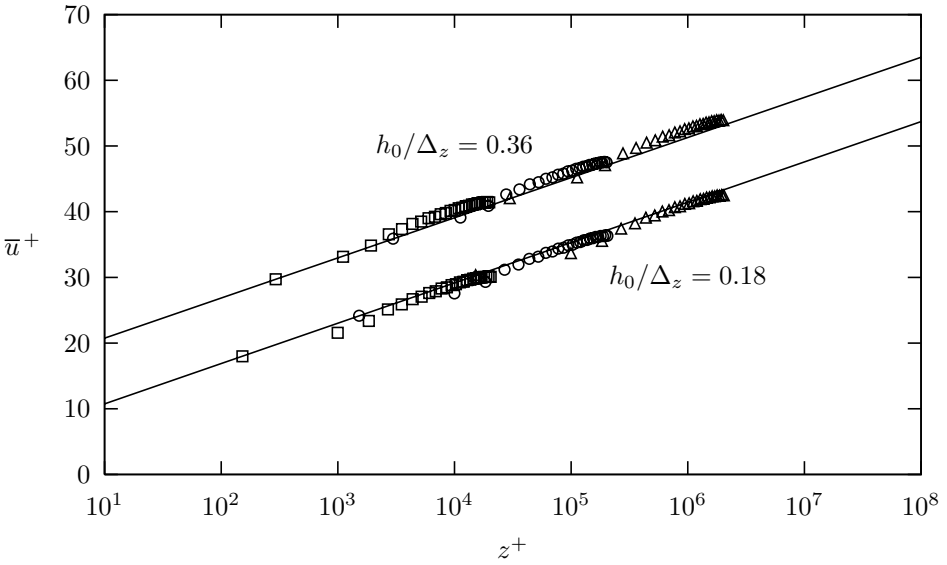

Figure 4.11. Model sensitivity to virtual wall location, h_0: upper set (set F), $(\overline{\mathcal{K}}_1)_{avg} = 0.38$, shifted up by 10 units for clarity; lower set (set A), $(\overline{\mathcal{K}}_1)_{avg} = 0.37$; ▫ , $Re_\tau = 20\,\mathrm{k}$; ○ , $Re_\tau = 200\,\mathrm{k}$; △ , $Re_\tau = 2\,\mathrm{M}$; ——— , $\log(z^+/11)/(\overline{\mathcal{K}}_1)_{avg} + 11$.

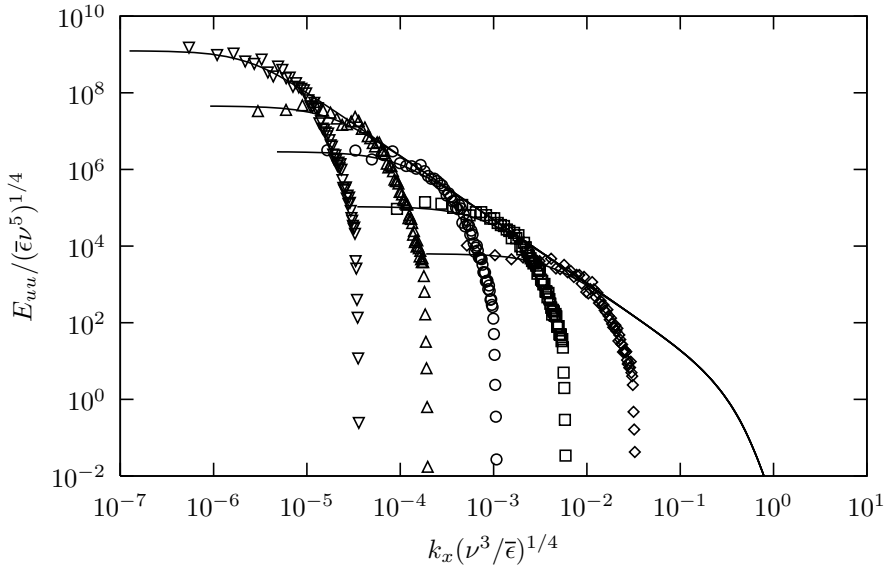

Figure 4.12. Resolved spectra at $z/\delta = 0.5$ for set A: ◇ , $Re_\tau = 2\,\mathrm{k}$; ▫ , $Re_\tau = 20\,\mathrm{k}$; ○ , $Re_\tau = 200\,\mathrm{k}$; △ , $Re_\tau = 2\,\mathrm{M}$; ▽ , $Re_\tau = 20\,\mathrm{M}$; ——— , model spectra (Pope 2000).

surrogate for the turbulent kinetic energy, $3u_{rms}^2/2$, where $u_{rms}^2 = \widetilde{\widetilde{u}\widetilde{u}} + \overline{T}_{xx}$. The envelope produced by the composite of all the spectra collapses onto the same $k^{-5/3}$ line, suggesting that in all cases, the Kolmogorov scale—and hence the total dissipation—are accurately predicted by the LES model, independent of Re_τ. The rapid (~ 6 points) drop near the 2/3-cutoff wavenumber is purely an artifact of the exponential smoothing, (4.25). The rest of the drop could be attributed to dominant SGS dynamics that overwhelm the resolved scales in that wavenumber range, resulting in the observed effect of excess resolved wavenumbers. To test this idea, we need the subgrid extension of the spectrum representing the dynamics of the SGS model.

4.5.3 Subgrid-Continued Spectra

A benefit of the stretched-spiral vortex model for LES is the availability of a closed-form spectral representation of the local Navier–Stokes solution that can be used to obtain the subgrid-continued spectra down to Kolmogorov scales. This was demonstrated for both velocity and scalar spectra by Hill, Pantano and Pullin (2006).

Given that the SGS vortices are oriented according to the delta-function distribution (§ 4.2.2), the one-dimensional spectrum tensors derived by Pullin and Saffman (1994) (equations (49)–(51)) for an ensemble of cylindrical vortices reduce to

$$\Theta_{11}(k_3) = \frac{2}{\pi}\int_{|k_3/\sin\theta|}^{\infty} E(k)\left(k^2 - \frac{k_3^2}{\sin^2\theta}\right)^{-1/2} \times \left[\frac{1}{k^2}\cos^2\theta\cos^2\phi\left(k^2 - \frac{k_3^2}{\sin^2\theta}\right) + \frac{1}{k^2}\sin^2\phi\frac{k_3^2}{\sin^2\theta}\right]\frac{1}{\sin\theta}\,\mathrm{d}k, \tag{4.32a}$$

$$\Theta_{22}(k_3) = \frac{2}{\pi}\int_{|k_3/\sin\theta|}^{\infty} E(k)\left(k^2 - \frac{k_3^2}{\sin^2\theta}\right)^{-1/2} \times \left[\frac{1}{k^2}\cos^2\theta\sin^2\phi\left(k^2 - \frac{k_3^2}{\sin^2\theta}\right) + \frac{1}{k^2}\cos^2\phi\frac{k_3^2}{\sin^2\theta}\right]\frac{1}{\sin\theta}\,\mathrm{d}k, \tag{4.32b}$$

$$\Theta_{33}(k_3) = \frac{2}{\pi}\int_{|k_3/\sin\theta|}^{\infty} E(k)\left(k^2 - \frac{k_3^2}{\sin^2\theta}\right)^{-1/2} \times \left[\frac{1}{k^2}\sin^2\theta\left(k^2 - \frac{k_3^2}{\sin^2\theta}\right)\right]\frac{1}{\sin\theta}\,\mathrm{d}k, \tag{4.32c}$$

with $E(k)$ is given by (4.3). Here, the Euler angles θ and ϕ (the delta-function peak locations) are defined relative to the (x_1, x_2, x_3) coordinate system, which is not necessarily coincident with the laboratory frame (different from § 4.2.2). The even function $\Theta_{ii}(k_3)$, no summation over i, is defined such that $\int_{-\infty}^{\infty}\Theta_{ii}(k_3)\,\mathrm{d}k_3 = (u_i)_{rms}^2$, from which it follows that $E_{ii}(k_3) = 2\Theta_{ii}(k_3)$. To obtain the subgrid-continued $E_{ii}(k_x)$, we choose k_3 to coincide with k_x; that is θ is the angle between the vortex axis and the x-axis. Given the wavenumber k_x, $E_{ii}(k_x)$ is found by averaging (4.32) over every cell on the xy-plane; $E_{ii}(k_y)$ is obtained in a similar manner. We remark that this calculation requires

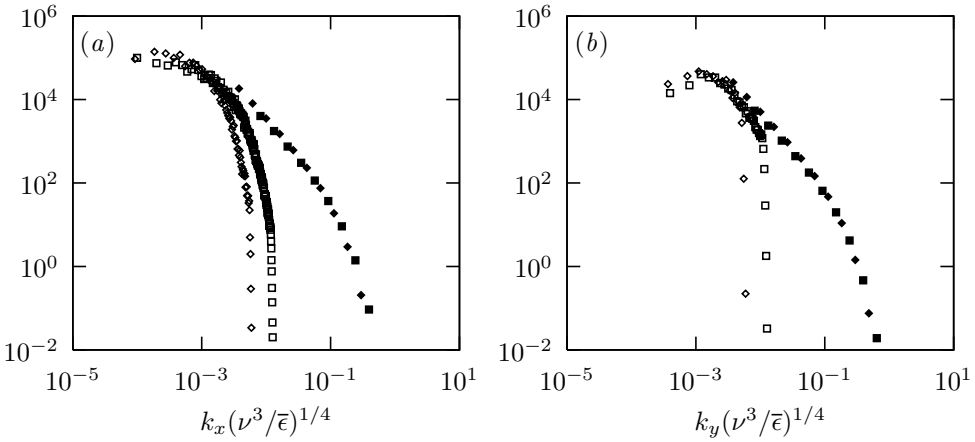

Figure 4.13. Effect of grid resolution on (a) $E_{uu}(k_x)/(\overline{\epsilon}\nu^5)^{1/4}$, and ($b$) $E_{uu}(k_y)/(\overline{\epsilon}\nu^5)^{1/4}$ at $z/\delta = 0.5$ for $Re_\tau = 20\,\mathrm{k}$: $\diamond$ case A2; $\square$ case B2; open symbols, resolved; solid symbols, subgrid.

only numerical information obtained from the LES through $E(k)$; no additional tuning parameters are required. Also, this calculation is only performed when subgrid-continued spectra are required; it is not a required part of the resolved-scale LES simulation.

Figure 4.13 shows both resolved and subgrid contributions to $E_{uu}(k_x)$ and $E_{uu}(k_y)$ for the $Re_\tau = 20\,\mathrm{k}$ case with two different grid resolutions. As the resolution is increased, the resolved spectra extend themselves to higher wavenumbers, following their subgrid extensions. Note, however, that the subgrid extensions remain unchanged as the resolution is increased; on this basis, one could claim that the SGS dynamics have converged. Unlike $E_{uu}(k_x)$, $E_{uu}(k_y)$ appears not to suffer from excess resolution, dropping sharply only near the 2/3-cutoff wavenumber. The subgrid part of $E_{uu}(k_x)$ (see figure 4.13(a)) continues where the resolved part drops off, reinforcing the idea that the SGS dynamics effectively take over.

We compare our LES prediction of E_{uu} at various wall distances with the DNS data of Hoyas and Jiménez (2006) in figure 4.14. The $z/\delta = 0.2$ plane corresponds to our fifth off-wall grid point, where $\overline{K}_{sgs}/(\overline{K}_{res} + \overline{K}_{sgs}) \approx 0.2$ (see figure 4.9(a)). At these wall locations, the composite of the resolved and subgrid components appear to faithfully capture the main features of the DNS spectra. These features include the spatial anisotropy of the subgrid extensions, seen in the ordering of the subgrid $E_{uu}(k_x)$ and $E_{uu}(k_y)$, and the hump in the resolved $E_{uu}(k_y)$ in the range $10^{-3} < k_y^+ < 10^{-2}$, which becomes less prominent as z/δ increases from 0.2 to 1. In figure 4.14(a), the subgrid extension of $E_{uu}(k_x)$ is slightly steeper than the DNS result. This may be due to a mismatch between the near-wall physics, which, perhaps, is exhibiting a k^{-1} range (Perry and Chong 1982), and our LES model based on stretched-spiral vortices, which have an inherent $k^{-5/3}$ inertial range.

We also plot one-dimensional spectra for the spanwise and wall-normal velocity components at $z/\delta = 0.5$ in figure 4.15. Comparing the spectra for the three velocities at the same wall-normal location (figures 4.15(a, b) and 4.14(b)), we see a faithful reproduction of the velocity anisotropy, as

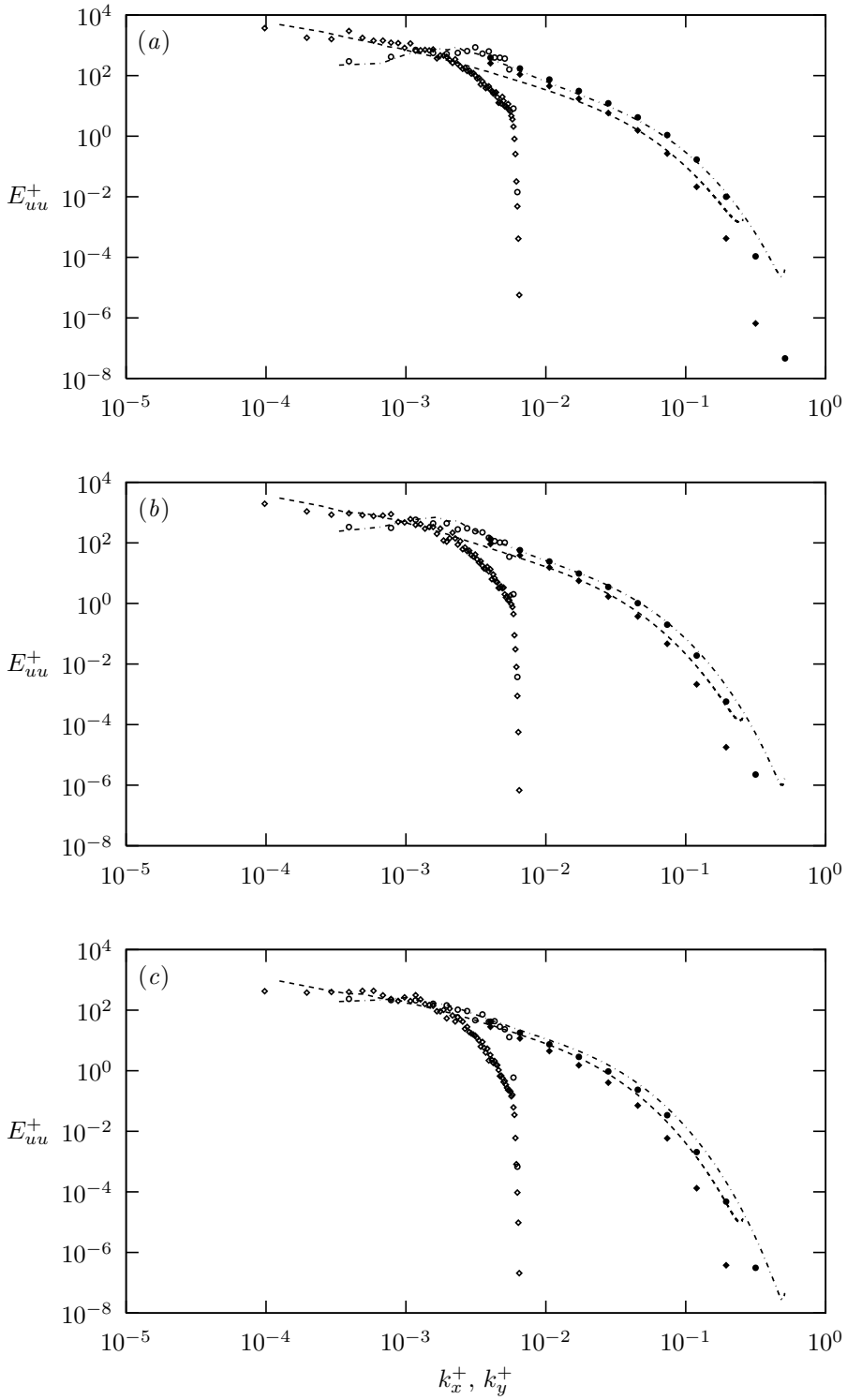

Figure 4.14. Spectra for $Re_\tau = 2\,\mathrm{k}$ (case A1) at (*a*) $z/\delta = 0.2$, (*b*) $z/\delta = 0.5$, and (*c*) $z/\delta = 1$: $\diamond$ and – – – – , $E^+_{uu}(k^+_x)$; $\circ$ and —·— , $E^+_{uu}(k^+_y)$; open symbols, resolved; solid symbols, subgrid; lines, DNS (Hoyas and Jiménez 2006).

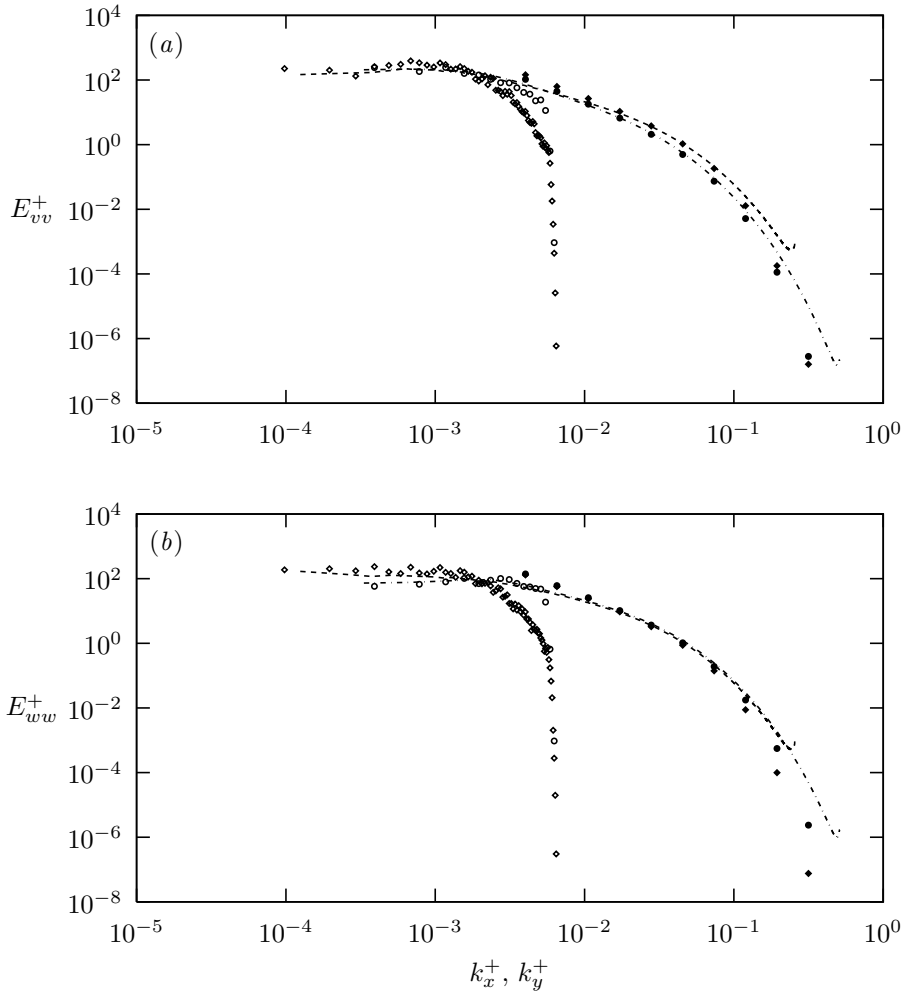

Figure 4.15. Spectra for $Re_\tau = 2\,\mathrm{k}$ (case A1) at $z/\delta = 0.5$: $\diamond$ and - - - - , $E^+_{vv}(k^+_x)$ and $E^+_{ww}(k^+_x)$; $\circ$ and —·— , $E^+_{vv}(k^+_y)$ and $E^+_{ww}(k^+_y)$; open symbols, resolved; solid symbols, subgrid; lines, DNS (Hoyas and Jiménez 2006).

well as the spatial anisotropy, both in the resolved components and the subgrid extension; in fact, the ordering of the subgrid $E_{uu}(k_x)$ and $E_{uu}(k_y)$ is switched for the subgrid $E_{vv}(k_x)$ and $E_{vv}(k_y)$ in $10^{-2} < k_x^+, k_y^+ < 10^{-1}$.

4.5.4 Wall Model in Inhomogeneous Flows

Since the present near-wall model is entirely local, it can readily be applied to inhomogeneous turbulent flows. While the predictive performance of a wall model in complex turbulent flows, especially those involving separation, can only be validated with an *a posteriori* analysis and further LES, some prior analysis may guide our expectations of the present model, which we now discuss.

First, we have argued that our approach is not an equilibrium model in the sense of Piomelli (2008). Presently the local–inner-scaling assumption (4.11) is used in a local sense to reduce only the unsteady term in the plane-filtered, wall-normal-averaged, streamwise momentum equation, leading to (4.15). We stress again that in this reduction, a specific $F(z^+)$ is not required. Further, our log-like profile (4.20) does not use (4.11) but is derived directly from the stretched-vortex subgrid model combined with the attached eddy hypothesis in a way that couples with the resolved-scale LES. In fact, the effective and local "Kármán constant" (4.19) depends partially on LES-derived quantities and so is also a mixed inner–outer scale parameter. Thus the combination of (4.15) and (4.20) can be viewed as containing elements of both restricted inner scaling and the outer flow via the LES. The overall model is therefore only partially reliant on inner scaling. This may be an improvement over TBLE approaches, where the log law is implied by the damped mixing-length eddy viscosity. We note that even when this log law is assumed, the TBLE approach improves the prediction of separated flows relative to equilibrium log law models (Cabot and Moin 1999).

Second, we can show that (4.15) contains an inherent signature for incipient separation in the sense that $u_\tau(x, y, t)$ vanishes locally. At each wall-adjacent (x, y) location, (4.15) can be written in the form ($\eta_0 \equiv \partial\widetilde{u}/\partial z|_0$)

$$\frac{\mathrm{d}\eta_0}{\mathrm{d}t} = \Lambda\eta_0(\widetilde{\eta}_0 - \eta_0), \tag{4.33}$$

where

$$\Lambda(t) = \frac{2\nu}{h\,\widetilde{u}|_h}, \quad \widetilde{\eta}_0(t) = -\frac{1}{\nu}\,\widetilde{uw}|_h - \frac{h}{\nu}\left(\frac{\partial\widetilde{uu}|_h}{\partial x} + \frac{\partial\widetilde{uv}|_h}{\partial y} + \left.\frac{\partial\widetilde{p}}{\partial x}\right|_h\right) + \left.\frac{\partial\widetilde{u}}{\partial z}\right|_h. \tag{4.34a,b}$$

After using the integrating factor,

$$I(t) = \exp\left(-\int_0^t \Lambda(s)\widetilde{\eta}_0(s)\,\mathrm{d}s\right), \tag{4.35}$$

(4.33) becomes separable, and its exact solution, written as an integral, is

$$\frac{1}{\eta_0(t)} = \frac{I(t)}{\eta_0(0)} + I(t)\int_0^t \frac{\Lambda(s)}{I(s)}\,\mathrm{d}s, \tag{4.36}$$

For simplicity now assume constant coefficients $\widetilde{\eta}_0(t) = \widetilde{\eta}_0(0)$ and $\Lambda(t) = \Lambda(0)$; then

$$\frac{1}{\eta_0(t)} = \frac{1}{\eta_0(0)}\mathrm{e}^{-t\Lambda(0)\widetilde{\eta}_0(0)} + \frac{1}{\widetilde{\eta}_0(0)}\left(1 - \mathrm{e}^{-t\Lambda(0)\widetilde{\eta}_0(0)}\right),$$

so that $\eta_0(t) \sim \widetilde{\eta}_0(0)$ for $t \gg 1/[\Lambda(0)\widetilde{\eta}_0(0)]$. Roughly, this means η_0 tends toward the steady state $\widetilde{\eta}_0$ at the rate $\Lambda\widetilde{\eta}_0$. A separation criterion can now be obtained based on (4.36). Without loss of generality, assume that $\eta_0(t=0) > 0$. Separation, defined by $\eta_0 = 0$, would occur at $t = t_s > 0$.

We know $I(t_s) > 0$ from (4.35), and upon assuming that $I(t_s) < \infty$, we require the integral in (4.36) to be singular for separation. A sufficient condition is $\Lambda(t) = O(t-t_s)^{-1}$ to give a logarithmic singularity. From the definition of $\Lambda(t)$ in (4.34 *a*), we require that $\widetilde{u}|_h = O(t - t_s)$. When $t > t_s$, $\widetilde{u}|_h$ changes sign, indicating that the outer flow has separated and is now reversed.

When the lifted wall penetrates the outer edge of the viscous sublayer, $h_0^+ < h_\nu^+ = 11$, which occurs near separation or in a laminar flow, the logarithmic boundary condition (4.20) would be replaced with the linear relationship $\widetilde{u}^+|_{h_0} = {h_0}^+$.

Finally, in the interests of minimizing discretization errors, we tested the present model on a purpose-built high-accuracy research code. However, we expect similar model performance on general-purpose codes—see Pantano et al. (2008), who successfully employed a second-order code to run a similar LES SGS model coupled with a different wall model.

Chapter 5

LES of Long Channel Flows

5.1 Background

Recently, Monty et al. (2007), Hutchins and Marusic (2007a,b), Mathis, Hutchins and Marusic (2009) observed long meandering structures in the log layer of boundary layers, channels, and pipes. These structures are marked by streamwise-oriented alternating low- and high-momentum streaks, and have lengths ranging from 6δ to 25δ (δ is the boundary layer thickness, channel half width, or pipe diameter). The relative energy content of these structures can be observed when plotting contours of the premultiplied longitudinal energy spectra, $k_x\,E_{uu}(k_x, z)$, on the $\log(\lambda_x)$–$\log(z)$ plane, where $\lambda_x = 2\pi/k_x$; Hutchins and Marusic (2007b) found that the long structures were related to the peak found at $(z/\delta, \lambda_x/\delta) = (0.06, 6)$ for $Re_\tau = 7.3\,\mathrm{k}$. Mathis, Hutchins and Marusic (2009) later found that the wall-normal location of this peak to scale with the middle of the log layer $z^+ = \sqrt{15}\,Re_\tau^{1/2}$, or equivalently, $z/\delta = \sqrt{15}Re_\tau^{-1/2}$.

According to Mathis, Hutchins and Marusic (2009), these large-scale structures are responsible for modulating the amplitudes of superimposed small-scale fluctuations. To test this idea, they extracted the large-scale signal by low-pass filtering the streamwise velocity at $\lambda_x/\delta > 1$, and then computed the correlation coefficients between the large-scale signal and the remaining small-scale signal at various z for Re_τ from 2.8–650 k.

In this chapter, we attempt to reproduce some of their results using the wall model for LES developed in chapter 4.

5.2 Simulation Details

The two LES simulations reported in this chapter are detailed in table 5.1: $\mathrm{k} \equiv 10^3$; $\delta' \equiv L_z/2 = \delta - h_0 \approx \delta$; u_c is the centerline velocity. To capture the effects of the long meandering structures, we use long channels, $L_x \approx 96\delta$. The mixing constant used in the interior of the LES domain, γ_{III}, was set to zero. Cases G1 and H3 are essentially the long channel versions of cases A1 and B3 detailed

Table 5.1. LES parameters for long channel flows.

Case	Re_τ	L_x/δ'	L_y/δ'	h_0/Δ_z	N_x	N_y	N_z	$T_\infty u_c/L_x$
G1	2 k	96	8	0.18	576	48	48	55.0
H3	200 k	96	8	0.18	1152	96	96	4.6

in table 4.1. The statistics reported in this chapter were taken over the period T_∞ (see table 5.1).

5.3 Sliding Averages and Sliding Intensities

We extract the large-scale component, u_L, of the streamwise velocity, u, by performing a local sliding average with period T (effectively a low-pass filter):

$$u_L(z,t;T) = \frac{1}{T}\int_t^{t+T} u(z,t')\,\mathrm{d}t'. \tag{5.1}$$

For notational clarity in (5.1), we omit the dependence on the homogeneous directions, x and y. The remaining part of the motion, $u-u_L$, is referred to as the local small-scale (relative to timescale T) fluctuations. The intensity of these small-scale fluctuations is measured by its root-mean-square value, u_{rms}, defined by

$$u_{rms}^2(z,t;T) = \frac{1}{T}\int_t^{t+T} \left[u(z,t') - u_L(z,t;T)\right]^2\,\mathrm{d}t'.$$

For the present LES, we also add the SGS contributions, which accounts for modeled fluctuations associated with timescale smaller than the numerical discretization Δ_t:

$$u_{rms}^2(z,t;T) = \frac{1}{T}\int_t^{t+T} \Big(\left[u(z,t') - u_L(z,t;T)\right]^2 + T_{xx}(z,t')\Big)\,\mathrm{d}t'.$$

The global mean is

$$\overline{u}(z) \equiv u_L(z,0;T_\infty),$$

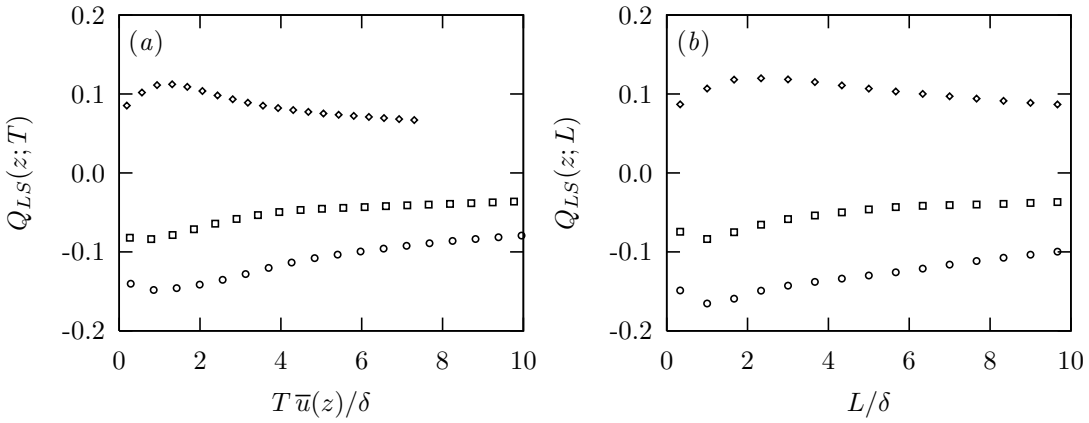

Figure 5.1. Effect of filter size on the large-scale–small-scale correlations at $Re_\tau = 2\,\mathrm{k}$ using (a) temporal averages and (b) spatial averages: $\diamond$, $z/\delta = 0.042$; $\square$, $z/\delta = 0.333$; $\circ$, $z/\delta = 0.625$.

where T_∞ is the data-recording period, and $T_\infty \gg z/\overline{u}(z)$. We now define the normalized correlation between the small scales and large scales, $Q(z;T)$, by

$$R_{LL}(z;T) = \frac{1}{T_\infty - T}\int_0^{T_\infty - T} \left[u_L(z,t;T) - \overline{u}(z)\right]^2 \,\mathrm{d}t, \tag{5.2a}$$

$$R_{SS}(z;T) = \frac{1}{T_\infty - T}\int_0^{T_\infty - T} u_{rms}^2(z,t;T)\,\mathrm{d}t, \tag{5.2b}$$

$$R_{LS}(z;T) = \frac{1}{T_\infty - T}\int_0^{T_\infty - T} \left[u_L(z,t;T) - \overline{u}(z)\right] u_{rms}(z,t;T)\,\mathrm{d}t, \tag{5.2c}$$

$$Q_{LS}(z;T) = \frac{R_{LS}(z;T)}{R_{LL}^{1/2}(z;T)R_{SS}^{1/2}(z;T)}. \tag{5.2d}$$

If large-scale higher-momentum streaks carry higher small-scale intensity, then $Q_{LS}(z;T) > 0$. Although the correlation coefficient defined in $(5.2d)$ is different from that used by Mathis, Hutchins and Marusic (2009), we expect similar qualitative features if the LES is successful.

The spatial counterpart to $(5.2d)$, called $Q_{LS}(z;L)$, is defined analogously. In this case, the large-scale component can be obtained by using the sliding average with length L:

$$u_L(x,z;L) = \frac{1}{L}\int_x^{x+L} u(x',z)\,\mathrm{d}x'.$$

5.4 Results and Discussion

In figure 5.1, we compare the correlations based on temporal filtering, $Q_{LS}(z;T)$, and correlations based on spatial filtering, $Q_{LS}(z;L)$, at various wall-normal distances, z for $Re_\tau = 2\,\mathrm{k}$. Near the wall, $z/\delta = 0.042$, the large scales and small scales are positively correlated but away from the wall, $z/\delta = 0.333$ and 0.625, they are negatively correlated. This observation holds for the range of filter sizes presently considered, $0.5\delta \lesssim T\overline{u}(z), L \lesssim 8\delta$. Also, when the filter sizes are increased beyond

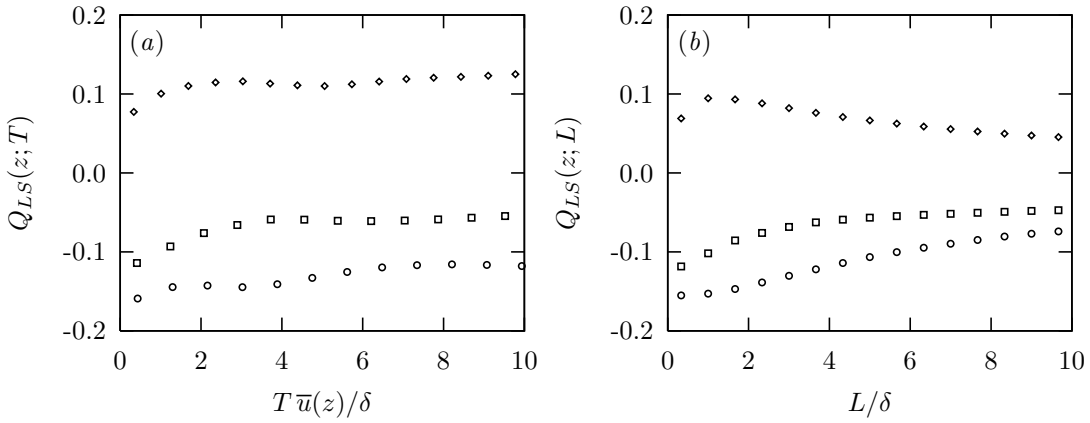

Figure 5.2. Effect of filter size on the large-scale–small-scale correlations at $Re_\tau = 200\,\mathrm{k}$ using (a) temporal averages and (b) spatial averages: $\diamond$, $z/\delta = 0.042$; $\square$, $z/\delta = 0.333$; $\circ$, $z/\delta = 0.625$.

δ, the near-wall correlations tend to become less positive while the correlations away from the wall tend to become less negative. Similar trends are reported in (Mathis, Hutchins and Marusic 2009, figure 11).

These general features are also present for $Re_\tau = 200\,\mathrm{k}$, although the near-wall peak for $Q_{LS}(z;T)$ is less obvious (see figure 5.2).

The wall-normal profiles of the same $Q_{LS}(z;T)$ and $Q_{LS}(z;L)$ for various filter sizes are shown in figures 5.3 and 5.4. The zero-crossing of these correlations appear to occur closer to the wall with increasing Re_τ. This is consistent with Mathis, Hutchins and Marusic (2009), who find these zero-crossings to scale with $z/\delta \sim \sqrt{15} Re_\tau^{-1/2}$. A quantitative comparison is impossible owing to the different low-pass filtering techniques, and perhaps also owing to the different flows (theirs is a boundary layer).

Note that at the center of the channel, the correlation increases slightly, but remains negative (see figures 5.3 and 5.4). This increase is also reported in Mathis, Hutchins and Marusic (2009), but their increase is from negative correlations to positive correlations.

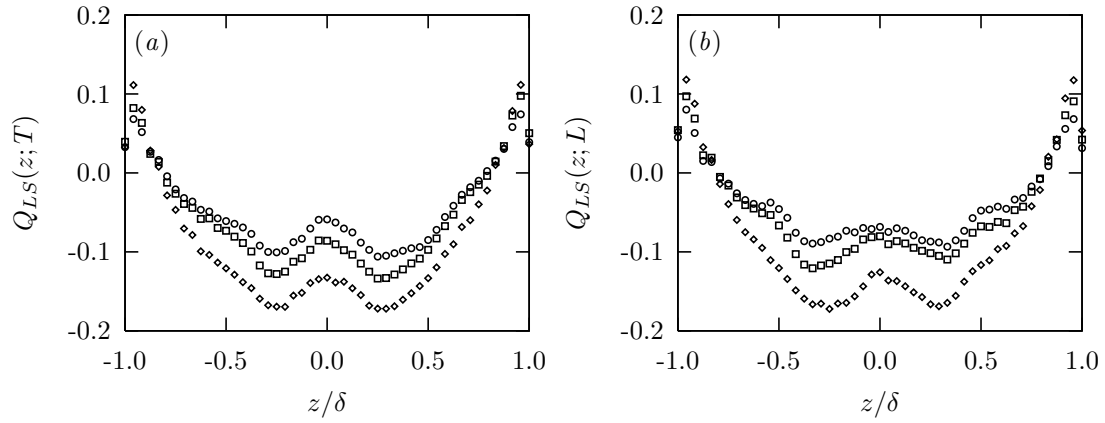

Figure 5.3. Large-scale–small-scale correlations at $Re_\tau = 2\,\mathrm{k}$ using (a) temporal averages and (b) spatial averages: $\diamond$, $Tu_c/\delta = 1.5$ and $L/\delta = 1.7$; $\square$, $Tu_c/\delta = 6.1$ and $L/\delta = 7.0$; $\circ$, $Tu_c/\delta = 10.8$ and $L/\delta = 12.3$. u_c is the centerline velocity.

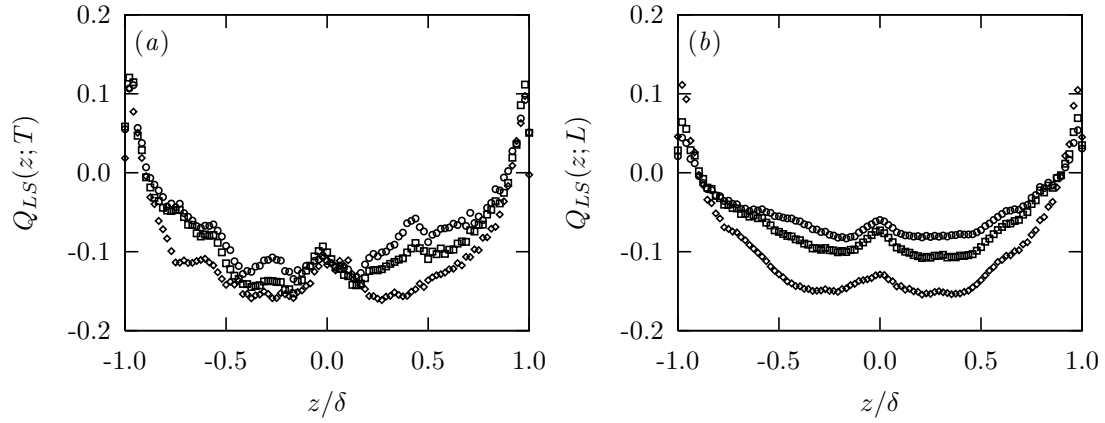

Figure 5.4. Large-scale–small-scale correlations at $Re_\tau = 200\,\mathrm{k}$ using (a) temporal averages and (b) spatial averages: $\diamond$, $Tu_c/\delta = 0.4$ and $L/\delta = 0.8$; $\square$, $Tu_c/\delta = 3.1$ and $L/\delta = 3.5$; $\circ$, $Tu_c/\delta = 5.7$ and $L/\delta = 6.2$. u_c is the centerline velocity.

Chapter 6

Conclusions

In the introduction, we argued for the need of a reliable yet cost-effective method to simulate turbulent flows of practical interest. To address this need, we extended the idea of multiscale LES, the underresolved fluid dynamical simulation that is furnished with a physical description of SGS dynamics. This was accomplished via the vortex-based SGS model for passive scalar mixing of Pullin (2000). We considered two areas of specialization: active scalar mixing in which an active (buoyant) scalar is modeled by small-Ri corrections to the passive scalar model; and wall-bounded turbulence in which the near-wall region was modeled with attached streamwise vortices that wind the streamwise velocity to produce near-wall turbulent shear stresses. We summarize in detail the contributions of each chapter in turn.

6.1 DNS of Statistically Stationary Buoyancy-Driven Turbulence

To better understand the nature of buoyancy-driven turbulence, we proposed in chapter 2 a novel method to simulate statistically stationary buoyancy-driven turbulence. The idea was to adapt the fringe-region technique to supply the flow with unmixed fluids within a triply periodic domain in the presence of gravity. The flow comprised an unforced mixing zone sandwiched between two thin horizontal fringe layers that injected unmixed fluids in an unstable configuration—heavy on top of light. At each point in the fringe, heavy unmixed fluid was introduced at the same mass rate as light unmixed fluid was removed so that no mass, momentum or energy was introduced; that is the flow was driven purely by buoyancy, which in turn was generated by density fluctuations created in the fringes. The fringes could also be interpreted as "unmixing" zones. This setup resulted in a statistically stationary flow, characterized by a linear mean mole-fraction profile.

We also developed a method to integrate the variable-density incompressible flow equations in a way that satisfies discrete mass conservation (expressed as a constraint on the velocity divergence)

regardless of iteration errors. This involved replacing the pressure with an alternative Lagrange multiplier, obtained from the Helmholtz–Hodge decomposition of $(1/\rho)(\partial p/\partial x_i)$. When the governing equations were discretized in this form, iteration errors were isolated to the time integration of baroclinic vorticity.

The DNS was performed at various Reynolds numbers, Atwood numbers and aspect ratios of the computational domain. For the aspect ratios investigated, $L_z/L_x = 1/2$, 1 and 2, we found that the large eddies tended to fill the horizontal extent of the simulation domain: $l_\rho \approx 0.5L_x$, where l_ρ is the horizontal integral wavelength of the box based on density fluctuations. Consequently, this DNS should be viewed as a model to study only the small scales of buoyancy-driven turbulence in the same way that we view DNS of homogeneous–isotropic turbulence.

When the computational domain is short relative to its width (case B), we report nontrivial correlations between the forced flow in the fringes and the flow at the midplane location ($z = L_z/2$); this reduced the usefulness of physical generalizations that can be drawn from that particular case. Except for case B, the ratio of Taylor-microscale Reynolds numbers was found to be $Re_{\lambda_z}/Re_{\lambda_{xy}} \approx 2$–2.5, indicating sustained anisotropy. This is close to the values reported in the Rayleigh–Taylor instability simulations of Cook and Dimotakis (2001) in which $Re_{\lambda_z}/Re_{\lambda_{xy}} \approx 2.5$–4.

We report that all the present DNS midplane planar spectra, namely E^{2D}_{ww}, $(E^{2D}_{uu} + E^{2D}_{vv})/2$, $E^{2D}_{\rho\rho}$ and $-E^{2D}_{\rho w}$, collapsed when scaled with the Kolmogorov–Obukhov–Corrsin scales: ν, ϵ, and ϵ_ρ. For the Reynolds numbers considered, the spectra appear to exhibit about one decade of power-law range, where $E^{2D}_{ww} \sim k_r^{-5/3}$, $(E^{2D}_{uu} + E^{2D}_{vv})/2 \sim k_r^{-5/3}$, $E^{2D}_{\rho\rho} \sim k_r^{-5/3}$ and $-E^{2D}_{\rho w} \sim k_r^{-7/3}$; k_r is the radial wavenumber. When compared with the corresponding spectra from the 3072^3 DNS of Rayleigh–Taylor instability (Cabot and Cook 2006), we found collapse in $E^{2D}_{\rho\rho}$ and $-E^{2D}_{\rho w}$, but not in the velocity spectra, where the present spectra shows slightly more energy in the dissipation range ($k_r\eta > 10^{-1}$). We suggested that this could be attributed to the difference between a statistically evolving flow, in which production exceeds dissipation (Rayleigh–Taylor), and a statistically stationary flow, in which production equals dissipation (present simulations).

Except for case B, the heavy-fluid mole-fraction (X_2) p.d.f.s plotted at various vertical locations within the mixing region (outside the fringe) exhibited a unimodal Gaussian-like distribution with peaks approaching $X_2 = 0$ near the lower fringe, and gradually shifting towards peaks approaching $X_2 = 1$ near the upper fringe.

6.2 LES and SGS Modeling of Active Scalar Mixing Flows

In chapter 3, we reasoned that the SGS active scalar modeling problem could be conceptually divided into two separate problems: a model for unstably stratified flows and a model for stably stratified flows. We discuss each of these in turn.

For unstably stratified flows, we showed that the SGS model of Pullin (2000), which was originally designed for passive scalars, can be used without modifications. This is because unstably stratified flows are rate limited by turbulent mixing, a key argument used in the development of the passive scalar SGS model. We ran LES of the flow described in chapter 2 to demonstrate this point.

At a small fraction (up to 10^{-5}) of the DNS computational effort, we ran LES of the DNS case E described in chapter 2. The LES spectra, including subgrid extensions, captured many essential features of the DNS spectra. For example, the LES velocity spectra exhibited large-scale anisotropy in the resolved component and also small-scale anisotropy in the subgrid extension including the viscous rolloff. Further, the LES velocity-anisotropy parameter, $E^{2D}_{ww}/E^{2D}_{u_iu_i} - 1/3$, showed a minimum at the beginning of the dissipation range, $k_r\eta = 10^{-1}$, in agreement with the present DNS, and also the 3072^3 Rayleigh–Taylor DNS of Cabot and Cook (2006). The occurrence of the anisotropy minimum was also reported by Livescu and Ristorcelli (2008). We also showed that the SGS model of Pullin (2000) contains an intrinsic $-7/3$ power-law scaling for the SGS ρ–w cospectrum. We then used this to obtain the subgrid extension of $-E^{2D}_{\rho w}$, which showed fair agreement with DNS.

For stably stratified flows, we developed an SGS model to operate in the wavenumber range $L_O^{-1} < k < \eta^{-1}$, where L_O is the Ozmidov lengthscale. Eddying motions larger than L_O are strongly affected by buoyancy via conversion from kinetic energy to potential energy. In the range $L_O^{-1} < k < \eta^{-1}$, the Richardson cascade is still preserved, although the dissipation that characterizes this range is slightly reduced by buoyancy. It is in this sense that we deemed a scalar to be mildly active. More precisely, the grid-dependent Richardson number, $Ri_{\Delta_c} = (\Delta_c/L_O)^{4/3} \sim (k_cL_O)^{-4/3} \ll 1$.

Starting from the passive scalar model of Pullin (2000), we added buoyancy effects, and identified the appropriate Ri. To make analytical progress, we performed a regular perturbation expansion in small Ri (equivalently, small g in dimensional form) of the vortex model equations and obtained its solution up to $O(Ri)$. We then averaged the solution across initial conditions, space and time to obtain the SGS kinetic energy and SGS scalar flux that contains $O(Ri)$ correction terms. These expressions showed that both the SGS kinetic energy and the SGS scalar flux are reduced slightly when $Ri > 0$.

Even though the physical meaning of the gradient Ri is undefined for unstable stratification, where $Ri < 0$, its value could still be computed, and we performed an *a posteriori* test of the new active scalar flux model based on the DNS of chapter 2. First, we tested the model in passive-scalar mode, where $Ri = 0$, by computing the mixing constant γ_{Y_1} of the model evaluated at various cutoff wavenumbers to show that it is indeed an $O(1)$ constant in the inertial range with values 1.2–1.8. This is in fair agreement with the elementary calculations of Pullin (2000), who estimated that $\gamma_{Y_1} = 0.89$–1.3. This suggests that our use of the passive scalar model in unstably stratified turbulence was well founded.

When the Ri corrections were included in this *a posteriori* test, we found little change. However,

the active scalar model could be potentially useful for LES of stably stratified flows, (e.g., Shih et al. 2005, Brethouwer et al. 2007). In that case, the scales in the wavenumber range $k < L_O^{-1}$ would be directly simulated, while the scales in the wavenumber range $L_O^{-1} < k < \eta^{-1}$ would be modeled by the present active scalar SGS model.

6.3 LES and Wall Modeling of Wall-Bounded Turbulence

An LES wall model based on SGS stretched vortices was developed in chapter 4. Its salient feature is the implementation of Dirichlet boundary conditions, including a streamwise slip velocity at a lifted, virtual wall that lies within the overlap region. This is done using a tailored SGS near-wall model based on the plane filtering and wall-normal averaging of the streamwise momentum equation combined with an extended version of the general stretched-vortex SGS model that incorporates the dominant near-wall physics. When coupled with outer, resolved-scale LES, use of the wall model produces satisfactory mean velocity profiles and acceptable second-order turbulence statistics over a wide range of Re_τ. This scheme also provides dynamic estimates of the Kármán constant that are consistent with experimental measurements. In the main body of the channel flow, subgrid-continued spectra agree well with DNS down to Kolmogorov scales, and capture anisotropy effects.

It may be interpreted that we have used the empirical logarithmic law of the wall to obtain the model boundary condition, thereby diminishing the predictive capability of the LES. However, we have only assumed a physical model of near-wall vortices to arrive at (4.20). It is the very physics of attached near-wall longitudinal stretched-spiral vortices that warrants the use of the logarithmic relationship in the same way that the very physics of stretched-spiral vortices warrants the use of the $-5/3$ inertial-range spectrum for the prediction of K in (4.3). Further, this physical model provides a means of dynamically calculating the instantaneous local Kármán constant, $\mathcal{K}_1$. A successful physical model should reproduce the logarithmic law of the wall along with the Kármán constant, so that the appearance of the logarithm only reinforces the validity of the present approach.

6.4 LES of Long Channel Flows

In chapter 5, we considered an application of the new wall model of chapter 4 by performing LES of long channels, $L_x \approx 96\delta$, at $Re_\tau = 2\,\mathrm{k}$ and $Re_\tau = 200\,\mathrm{k}$. These simulations were designed to capture the amplitude-modulation effects of recently reported large-scale log-layer structures.

After decomposing the streamwise velocity into large-scale and small-scale components via a top-hat window filter, we computed the correlation Q_{LS} between the large-scale deviations and its associated small-scale fluctuation intensities. These correlations were found to be in qualitative agreement with the recent findings of Mathis, Hutchins and Marusic (2009): 1) $Q_{LS} > 0$ near the

wall and $Q_{LS} < 0$ away from the wall; 2) the zero crossings of Q_{LS} occurred closer to the wall at the higher Re_τ; and 3) Q_{LS} increased near the channel center but remains negative, while Mathis, Hutchins and Marusic (2009) reported an increase from $Q_{LS} < 0$ to $Q_{LS} > 0$ at the boundary layer edge. A quantitative comparison is impossible owing to the different flows—channel versus zero pressure gradient boundary layer—and to the different low-pass filter definitions.

Appendix A

Subgrid Extension of Planar Cospectrum

This appendix follows closely the derivation outlined by Hill, Pantano and Pullin (2006) and Pullin and Saffman (1994). We define the velocity–scalar cross correlation (O'Gorman and Pullin 2003):

$$R_{u_ic}(\boldsymbol{r}) = \frac{1}{L^3}\int u_i(\boldsymbol{x})c(\boldsymbol{x}+\boldsymbol{r})\,\mathrm{d}\boldsymbol{x}.$$

Its Fourier-transform pair is

$$R_{u_ic}(\boldsymbol{r}) = \int \Phi_{u_ic}(\boldsymbol{k})\,\exp(\mathrm{i}\boldsymbol{k}\cdot\boldsymbol{r})\,\mathrm{d}\boldsymbol{k}, \quad \Phi_{u_ic}(\boldsymbol{k}) = \frac{1}{(2\pi)^3}\int R_{u_ic}(\boldsymbol{r})\,\exp(-\mathrm{i}\boldsymbol{k}\cdot\boldsymbol{r})\,\mathrm{d}\boldsymbol{r}. \tag{A.1}$$

We then define the x_1x_2-plane cospectrum from

$$R_{u_ic}(\boldsymbol{0}) = \frac{1}{L^3}\int u_i(\boldsymbol{x})c(\boldsymbol{x})\mathrm{d}\boldsymbol{x} = \int \Phi_{u_ic}(\boldsymbol{k})\,\mathrm{d}\boldsymbol{k} = \int_0^\infty E^{2D}_{u_ic}(k_r)\,\mathrm{d}k_r,$$

where

$$E^{2D}_{u_ic}(k_r) = k_r\int_{-\infty}^{\infty}\int_0^{2\pi}\Phi_{u_ic}\,\mathrm{d}\theta\,\mathrm{d}k_3, \tag{A.2}$$

and $k_r^2 = k_1^2+k_2^2$. If the subgrid turbulent flow field is described by an ensemble of m vortex segments, each of which has length l_m and orientation given by Euler angles (α,β,γ), the velocity–scalar cross correlation can then be written as (Lundgren 1982)

$$\begin{aligned} R_{u_ic}(\boldsymbol{\rho}) = \frac{1}{L^3}\sum_m l_m\int_{-\infty}^{\infty}\int_{-\infty}^{\infty}\frac{1}{8\pi^2}\int_0^{2\pi}\int_0^{2\pi}\int_0^{\pi} E_{ji}u_j'^{(m)}(r_1',r_2')c^{(m)}(r_1'+\rho_1',r_2'+\rho_2') \\ \times P(\alpha,\beta,\gamma)\,\sin\alpha\,\mathrm{d}\alpha\,\mathrm{d}\beta\,\mathrm{d}\gamma\,\mathrm{d}r_1'\,\mathrm{d}r_2', \end{aligned} \tag{A.3}$$

where primes indicate vortex-frame variables; $P(\alpha,\beta,\gamma)$ is the p.d.f. of vortex orientation ($P=1$ for isotropic turbulence); and E_{ij} is the rotation matrix that maps laboratory frame and vortex frame

such that $r_i = E_{ji} r'_j$ and $r'_j = E_{ji} r_i$. Define the Fourier-transform pair:

$$u_i'^{(m)}(r'_1, r'_2) = \int_{-\infty}^{\infty}\int_{-\infty}^{\infty} \widehat{u}_i'^{(m)}(\kappa_1, \kappa_2) \mathrm{e}^{\mathrm{i}\kappa_1 r'_1 + \mathrm{i}\kappa_2 r'_2}\, \mathrm{d}\kappa_1\, \mathrm{d}\kappa_2, \tag{A.4a}$$

$$\widehat{u}_i'^{(m)}(\kappa_1, \kappa_2) = \frac{1}{(2\pi)^2}\int_{-\infty}^{\infty}\int_{-\infty}^{\infty} u_i'^{(m)}(r'_1, r'_2) \mathrm{e}^{-\mathrm{i}\kappa_1 r'_1 - \mathrm{i}\kappa_2 r'_2}\, \mathrm{d}r'_1\, \mathrm{d}r'_2; \tag{A.4b}$$

a similar Fourier-transform pair can be written for $c^{(m)}$ and $\widehat{c}^{(m)}$. Substitute (A.4) in (A.3), and then use $\int_{-\infty}^{\infty} \mathrm{e}^{\mathrm{i}kr}\, \mathrm{d}r = 2\pi\delta(k)$ to get

$$\begin{aligned} R_{u_i c}(\boldsymbol{r}) = \frac{(2\pi)^2}{L^3}\sum_m l_m \int_{-\infty}^{\infty}\int_{-\infty}^{\infty} \frac{1}{8\pi^2}\int_0^{2\pi}\int_0^{2\pi}\int_0^{\pi} E_{ji}\widehat{u}_j'^{(m)}(\kappa_1, \kappa_2)\widehat{c}^{*(m)}(\kappa_1, \kappa_2) \\ \times \mathrm{e}^{-\mathrm{i}\kappa_1 r'_1 - \mathrm{i}\kappa_2 r'_2} P(\alpha, \beta, \gamma) \sin\alpha\, \mathrm{d}\alpha\, \mathrm{d}\beta\, \mathrm{d}\gamma\, \mathrm{d}\kappa_1\, \mathrm{d}\kappa_2. \end{aligned} \tag{A.5}$$

Substitute (A.5) in the expression for $\Phi_{u_i c}$ (A.1), and then use $\kappa_1 r'_1 + \kappa_2 r'_2 = (\kappa_1 E_{1i} + \kappa_2 E_{2i}) r_i$ to evaluate the $\boldsymbol{r}$ integrals:

$$\begin{aligned} &\int_{-\infty}^{\infty}\int_{-\infty}^{\infty}\int_{-\infty}^{\infty} \mathrm{e}^{-\mathrm{i}(\kappa_1 r'_1 + \kappa_2 r'_2)} \mathrm{e}^{-\mathrm{i}(k_1 r_1 + k_2 r_2 + k_3 r_3)}\, \mathrm{d}r_1\, \mathrm{d}r_2\, \mathrm{d}r_3 \\ &= (2\pi)^3 \delta(\kappa_1 E_{11} + \kappa_2 E_{21} + k_1)\delta(\kappa_1 E_{12} + \kappa_2 E_{22} + k_2)\delta(\kappa_1 E_{13} + \kappa_2 E_{23} + k_3). \end{aligned}$$

After putting the resulting expression for $\Phi_{u_i c}$ in (A.2), we arrive at

$$\begin{aligned} E^{2D}_{u_i c}(k_r) = k_r \int_{-\infty}^{\infty}\int_0^{2\pi} \frac{(2\pi)^2}{L^3}\sum_m l_m \int_{-\infty}^{\infty}\int_{-\infty}^{\infty} \frac{1}{8\pi^2}\int_0^{2\pi}\int_0^{2\pi}\int_0^{\pi} \\ \delta(\kappa_1 E_{11} + \kappa_2 E_{21} + k_1)\delta(\kappa_1 E_{12} + \kappa_2 E_{22} + k_2)\delta(\kappa_1 E_{13} + \kappa_2 E_{23} + k_3) \\ \times E_{ji}\widehat{u}_j'^{(m)}(\kappa_1, \kappa_2)\widehat{c}^{*(m)}(\kappa_1, \kappa_2) P(\alpha, \beta, \gamma) \sin\alpha\, \mathrm{d}\alpha\, \mathrm{d}\beta\, \mathrm{d}\gamma\, \mathrm{d}\kappa_1\, \mathrm{d}\kappa_2\, \mathrm{d}\theta\, \mathrm{d}k_3. \end{aligned} \tag{A.6}$$

Evaluate the k_3 integral:

$$\int_{-\infty}^{\infty} \delta(\kappa_1 E_{13} + \kappa_2 E_{23} + k_3)\, \mathrm{d}k_3 = 1$$

with

$$0 = -\kappa_1 \sin\alpha\cos\gamma + \kappa_2 \sin\alpha \sin\gamma + k_3 = -\kappa\cos(\gamma + \theta_\kappa)\sin\alpha + k_3, \tag{A.7}$$

where $\kappa_1 = \kappa\cos\theta_\kappa$ and $\kappa_2 = \kappa\sin\theta_\kappa$. To evaluate the θ and γ integrals, we will use

$$\delta\left[f(\theta,\gamma)\right]\delta\left[g(\theta,\gamma)\right] = \sum_q \frac{\delta(\theta - \theta_q)\delta(\gamma - \gamma_q)}{J(\theta_q, \gamma_q)},$$

where

$$J(\theta,\gamma) = \begin{vmatrix} \dfrac{\partial f}{\partial \theta} & \dfrac{\partial g}{\partial \theta} \\ \dfrac{\partial f}{\partial \gamma} & \dfrac{\partial g}{\partial \gamma} \end{vmatrix}, \quad f(\theta_q,\gamma_q) = g(\theta_q,\gamma_q) = 0. \tag{A.8}$$

That is, the sum is over the roots of f and g, which are arguments of the two delta functions:

$$\begin{aligned} f(\theta,\gamma) &= \kappa_1(\cos\alpha\cos\beta\cos\gamma - \sin\beta\sin\gamma) + \kappa_2(-\cos\alpha\cos\beta\sin\gamma - \sin\beta\cos\gamma) + k_1, \\ &= \kappa(\cos\alpha\cos\beta\cos(\gamma+\theta_\kappa) - \sin\beta\sin(\gamma+\theta_\kappa)) + k_r\cos\theta, \qquad (A.9a) \\ g(\theta,\gamma) &= \kappa_1(\cos\alpha\sin\beta\cos\gamma + \cos\beta\sin\gamma) + \kappa_2(-\cos\alpha\sin\beta\sin\gamma + \cos\beta\cos\gamma) + k_2, \\ &= \kappa(\cos\alpha\sin\beta\cos(\gamma+\theta_\kappa) + \cos\beta\sin(\gamma+\theta_\kappa)) + k_r\sin\theta, \qquad (A.9b) \end{aligned}$$

where $k_1 = k_r\cos\theta$ and $k_2 = k_r\sin\theta$. Compute $J(\theta,\gamma)$ from the partial derivatives in (A.8), then substitute for k_1 and k_2 obtained from $f(\theta_q,\gamma_q) = g(\theta_q,\gamma_q) = 0$ to get

$$J(\theta_q,\gamma_q) = \kappa^2\sin^2\alpha\cos(\gamma+\theta_\kappa)\sin(\gamma+\theta_\kappa). \tag{A.10}$$

But $k^2 = \kappa^2$ and $k^2 = k_r^2 + k_3^2$, so $k_3^2 = \kappa^2 - k_r^2$ and hence, together with (A.7),

$$\cos^2(\gamma+\theta_\kappa) = \frac{k_3^2}{\kappa^2\sin^2\alpha} = \frac{\kappa^2 - k_r^2}{\kappa^2\sin^2\alpha}, \tag{A.11a}$$

$$\sin^2(\gamma+\theta_\kappa) = \frac{\kappa^2\sin^2\alpha - k_3^2}{\kappa^2\sin^2\alpha} = \frac{k_r^2 - \kappa^2\cos^2\alpha}{\kappa^2\sin^2\alpha}. \tag{A.11b}$$

Put (A.11) in (A.10) to get

$$J(\theta_q,\gamma_q) = (\kappa^2 - k_r^2)^{1/2}(k_r^2 - \kappa^2\cos^2\alpha)^{1/2}, \quad k_r < \kappa < |k_r/\cos\alpha|. \tag{A.12}$$

The inequality ensures that the square roots in (A.12) can be taken; it also ensures that the roots (θ_q,γ_q) exist. Note that $J(\theta_q,\gamma_q)$ is independent of (θ_q,γ_q). We will assume that the orientation p.d.f. is independent of the spin angle γ, that is $P(\alpha,\beta,\gamma) = P(\alpha,\beta)$. The passive scalar SGS model of Pullin (2000) says that $u_3'^{(m)} = 0$, so

$$E_{ji}\widehat{u}_j'^{(m)} = E_{1i}\widehat{u}_1'^{(m)} + E_{2i}\widehat{u}_2'^{(m)} = E_{1i}E_{1j}\widehat{u}_j^{(m)} + E_{2i}E_{2j}\widehat{u}_j^{(m)} = (\delta_{ij} - E_{3i}E_{3j})\widehat{u}_j^{(m)},$$

which is also independent of γ. But then, the integrand in (A.6) is independent of (θ_q,γ_q). Therefore, to evaluate the θ and γ integrals, we need to only know how many roots (θ_q,γ_q) exist and when they exist. The form of (A.9) indicate that there are four pairs of such roots. Perform the θ and γ

integrals:

$$\int_0^{2\pi}\int_0^{2\pi}\delta(\kappa_1 E_{11}+\kappa_2 E_{21}+k_1)\,\delta(\kappa_1 E_{12}+\kappa_2 E_{22}+k_2)\,\mathrm{d}\gamma\,\mathrm{d}\theta$$
$$=\frac{4}{(\kappa^2-k_r^2)^{1/2}(k_r^2-\kappa^2\cos^2\alpha)^{1/2}}$$

if $k_r<\kappa<|k_r/\cos\alpha|$, otherwise the integrals vanish. Equation (A.6) then becomes

$$E_{u_ic}^{2D}(k_r)=k_r\frac{(2\pi)^2}{L^3}\sum_m l_m\int_{k_r}^{|k_r/\cos\alpha|}\int_0^{2\pi}\frac{1}{8\pi^2}\int_0^{2\pi}\int_0^{\pi}(\delta_{ij}-E_{3i}E_{3j})\widehat{u}_j^{(m)}(\kappa,\theta_\kappa)\widehat{c}^{*(m)}(\kappa,\theta_\kappa)$$
$$\times\frac{4}{(\kappa^2-k_r^2)^{1/2}(k_r^2-\kappa^2\cos^2\alpha)^{1/2}}P(\alpha,\beta)\sin\alpha\,\mathrm{d}\alpha\,\mathrm{d}\beta\,\kappa\,\mathrm{d}\theta_\kappa\,\mathrm{d}\kappa. \tag{A.13}$$

But the velocity–scalar cospectrum of the two-dimensional flow in an (α,β)-oriented vortex cross section is given by

$$E_{u_ic}(\kappa;\alpha,\beta)=\frac{(2\pi)^2}{L^3}\sum_m l_m\int_0^{2\pi}(\delta_{ij}-E_{3i}E_{3j})\widehat{u}_j^{(m)}(\kappa,\theta_\kappa)\widehat{c}^{*(m)}(\kappa,\theta_\kappa)\,\kappa\,\mathrm{d}\theta_\kappa. \tag{A.14}$$

Put (A.14) in (A.13):

$$E_{u_ic}^{2D}(k_r)=k_r\int_{k_r}^{|k_r/\cos\alpha|}\frac{1}{8\pi^2}\int_0^{2\pi}\int_0^{\pi}E_{u_ic}(\kappa;\alpha,\beta)$$
$$\times\frac{4}{(\kappa^2-k_r^2)^{1/2}(k_r^2-\kappa^2\cos^2\alpha)^{1/2}}P(\alpha,\beta)\sin\alpha\,\mathrm{d}\alpha\,\mathrm{d}\beta\,\mathrm{d}\kappa.$$

Finally, use the delta-function p.d.f. for vortex alignment,

$$P(\alpha,\beta)=\frac{4\pi}{\sin\alpha_0}\delta(\alpha-\alpha_0)\,\delta(\beta-\beta_0),$$

to get

$$E_{u_ic}^{2D}(k_r)=\frac{2k_r}{\pi}\int_{k_r}^{|k_r/\cos\alpha_0|}\frac{E_{u_ic}(\kappa;\alpha_0,\beta_0)}{(\kappa^2-k_r^2)^{1/2}(k_r^2-\kappa^2\cos^2\alpha_0)^{1/2}}\,\mathrm{d}\kappa.$$

Bibliography

Adrian, R. J. 2007 Hairpin vortex organization in wall turbulence. *Phys. Fluids* **19**, 041301.

Bakewell, H. P. and Lumley, J. L. 1967 Viscous sublayer and adjacent wall region in turbulent pipe flow. *Phys. Fluids* **10**, 1880–1889.

Batchelor, G. K., Canuto, V. M. and Chasnov, J. R. 1992 Homogeneous buoyancy-generated turbulence. *J. Fluid Mech.* **235**, 349–378.

Bertolotti, F. P., Herbert, T. and Spalart, P. R. 1992 Linear and nonlinear stability of the blasius boundary layer. *J. Fluid Mech.* **242**, 441–474.

Brethouwer, G., Billant, P., Lindborg, E. and Chomaz, J.-M. 2007 Scaling analysis and simulation of strongly stratified turbulent flows. *J. Fluid Mech.* **585**, 343–368.

Burton, G. C. 2008 The nonlinear large-eddy simulation method applied to $Sc \approx 1$ and $Sc \gg 1$ passive-scalar mixing. *Phys. Fluids* **20**, 035103.

Cabot, W. and Moin, P. 1999 Approximate wall boundary conditions in the large-eddy simulation of high Reynolds number flow. *Flow Turbul. Combust.* **63**, 269–291.

Cabot, W. H. and Cook, A. W. 2006 Reynolds number effects on Rayleigh–Taylor instability with possible implications for type-Ia supernovae. *Nature Phys.* **2**, 562–568.

Canuto, C., Hussaini, M. Y., Quarteroni, A. and Zang, T. A. 1987 *Spectral Methods in Fluid Dynamics*. Springer.

Carpenter, M. H., Gottlieb, D. and Abarbanel, S. 1994 Time-stable boundary conditions for finite-difference schemes solving hyperbolic systems: Methodology and application to high-order compact schemes. *J. Comput. Phys.* **111**, 220–236.

Chang, W., Giraldo, F. and Perot, B. 2002 Analysis of an exact fractional step method. *J. Comput. Phys.* **180**, 183–199.

Chorin, A. J. and Marsden, J. E. 1993 *A Mathematical Introduction to Fluid Mechanics*, 3rd edition. Springer.

Cook, A. W., Cabot, W. and Miller, P. L. 2004 The mixing transition in Rayleigh–Taylor instability. *J. Fluid Mech.* **511**, 333–362.

Cook, A. W. and Dimotakis, P. E. 2001 Transition stages of Rayleigh–Taylor instability between miscible fluids. *J. Fluid Mech.* **443**, 69–99.

Deardorff, J. W. 1970 A numerical study of three-dimensional turbulent channel flow at large Reynolds numbers. *J. Fluid Mech.* **41**, 453–480.

DeGraaff, D. B. and Eaton, J. K. 2000 Reynolds-number scaling of the flat-plate turbulent boundary layer. *J. Fluid Mech.* **422**, 319–346.

Del Álamo, J. C., Jiménez, J., Zandonade, P. and Moser, R. D. 2004 Scaling of the energy spectra of turbulent channels. *J. Fluid Mech.* **500**, 135–144.

Diener, P., Dorband, E. N., Schnetter, E. and Tiglio, M. 2007 Optimized high-order derivative and dissipation operators satisfying summation by parts, and applications in three-dimensional multi-block evolutions. *J. Sci. Comput.* **32**, 109–145.

Dimotakis, P. E. 2000 The mixing transition in turbulent flows. *J. Fluid Mech.* **409**, 69–98.

Dimotakis, P. E. 2005 Turbulent mixing. *Annu. Rev. Fluid Mech.* **37**, 329–356.

Germano, M., Piomelli, U., Moin, P. and Cabot, W. H. 1991 A dynamic subgrid-scale eddy viscosity model. *Phys. Fluids* A **3**, 1760–1765.

Ghosal, S. 1996 An analysis of numerical errors in large-eddy simulations of turbulence. *J. Comput. Phys.* **125**, 187–206.

Gottlieb, D. and Shu, C. 1997 On the Gibbs phenomenon and its resolution. *SIAM Rev.* **39**, 644–668.

Head, M. R. and Bandyopadhyay, P. 1981 New aspects of turbulent boundary-layer structure. *J. Fluid Mech.* **107**, 297–338.

Hill, D. J., Pantano, C. and Pullin, D. I. 2006 Large-eddy simulation and multiscale modelling of a Richtmyer–Meshkov instability with reshock. *J. Fluid Mech.* **557**, 29–61.

Hill, D. J. and Pullin, D. I. 2004 Hybrid tuned center-difference–WENO method for large eddy simulations in the presence of strong shocks. *J. Comput. Phys.* **194**, 435–450.

Hou, T. Y. and Li, R. 2007 Computing nearly singular solutions using pseudo-spectral methods. *J. Comput. Phys.* **226**, 379–397.

Hoyas, S. and Jiménez, J. 2006 Scaling of the velocity fluctuations in turbulent channels up to $Re_\tau = 2003$. *Phys. Fluids* **18**, 011702.

Hutchins, N. and Marusic, I. 2007a Evidence of very long meandering features in the logarithmic region of turbulent boundary layers. *J. Fluid Mech.* **579**, 1–28.

Hutchins, N. and Marusic, I. 2007b Large-scale influences in near-wall turbulence. *Phil. Trans. R. Soc.* A **365**, 647–664.

Ivey, G. N., Winters, K. B. and Koseff, J. R. 2008 Density stratification, turbulence, but how much mixing? *Annu. Rev. Fluid Mech.* **40**, 169–184.

Jiménez, J. and Moin, P. 1991 The minimal flow unit in near-wall turbulence. *J. Fluid Mech.* **225**, 213–240.

Kim, J., Moin, P. and Moser, R. 1987 Turbulence statistics in fully developed channel flow at low Reynolds number. *J. Fluid Mech.* **177**, 133–166.

Krawczynski, J. F., Renou, B., Danaila, L. and Demoulin, F. X. 2006 Small-scale measurements in a partially stirred reactor. *Exp. Fluids* **40**, 667–682.

Lilly, D. K. 1992 A proposed modification of the Germano subgrid-scale closure method. *Phys. Fluids* A **4**, 633–635.

Livescu, D. and Ristorcelli, J. R. 2007 Buoyancy-driven variable-density turbulence. *J. Fluid Mech.* **591**, 43–71.

Livescu, D. and Ristorcelli, J. R. 2008 Variable-density mixing in buoyancy-driven turbulence. *J. Fluid Mech.* **605**, 145–180.

Lumley, J. L. 1967 Similarity and the turbulent energy spectrum. *Phys. Fluids* **10**, 855–858.

Lundgren, T. S. 1982 Strained spiral vortex model for turbulent fine structure. *Phys. Fluids* **25**, 2193–2203.

Marušić, I. and Perry, A. E. 1995 A wall-wake model for the turbulence structure of boundary layers. Part 2. Further experimental support. *J. Fluid Mech.* **298**, 389–407.

Mathis, R., Hutchins, N. and Marusic, I. 2009 Large-scale amplitude modulation of the small-scale structures in turbulent boundary layers. *J. Fluid Mech.* In press.

Mattner, T., Pullin, D. and Dimotakis, P. 2004 Large-eddy simulations of Rayleigh–Taylor instability between miscible fluids. In *Proceedings of the 9th International Workshop on the Physics of Compressible Turbulent Mixing* (ed. S. B. Dalziel). Cambridge, UK.

Mattsson, K. and Nordström, J. 2004 Summation by parts operators for finite difference approximations of second derivatives. *J. Comput. Phys.* **199**, 503–540.

Misra, A. and Pullin, D. I. 1997 A vortex-based subgrid stress model for large-eddy simulation. *Phys. Fluids* **9**, 2443–2454.

Monty, J. P., Stewart, J. A., Williams, R. C. and Chong, M. S. 2007 Large-scale features in turbulent pipe and channel flows. *J. Fluid Mech.* **589**, 147–156.

Mueschke, N. J. and Schilling, O. 2009 Investigation of Rayleigh–Taylor turbulence and mixing using direct numerical simulation with experimentally measured initial conditions. I. Comparison to experimental data. *Phys. Fluids* **21**, 014106.

Nakayama, A., Noda, H. and Maeda, K. 2004 Similarity of instantaneous and filtered velocity fields in the near wall region of zero-pressure gradient boundary layer. *Fluid Dyn. Res.* **35**, 299–321.

Nickels, T. B. 2004 Inner scaling for wall-bounded flows subject to large pressure gradients. *J. Fluid Mech.* **521**, 217–239.

Nickels, T. B., Marusic, I., Hafez, S., Hutchins, N. and Chong, M. S. 2007 Some predictions of the attached eddy model for a high Reynolds number boundary layer. *Phil. Trans. R. Soc.* A **365**, 807–822.

Nordström, J., Nordin, N. and Henningson, D. 1999 The fringe region technique and the Fourier method used in the direct numerical simulation of spatially evolving viscous flows. *SIAM J. Sci. Comput.* **20**, 1365–1393.

O'Gorman, P. A. and Pullin, D. I. 2003 The velocity-scalar cross spectrum of stretched spiral vortices. *Phys. Fluids* **15**, 280–291.

Overholt, M. R. and Pope, S. B. 1996 Direct numerical simulation of a passive scalar with imposed mean gradient in isotropic turbulence. *Phys. Fluids* **8**, 3128–3148.

Pantano, C., Deiterding, R., Hill, D. J. and Pullin, D. I. 2007 A low numerical dissipation patch-based adaptive mesh refinement method for large-eddy simulation of compressible flows. *J. Comput. Phys.* **221**, 63–87.

Pantano, C., Pullin, D. I., Dimotakis, P. E. and Matheou, G. 2008 LES approach for high Reynolds number wall-bounded flows with application to turbulent channel flow. *J. Comput. Phys.* **227**, 9271–9291.

Perry, A. E. and Chong, M. S. 1982 On the mechanism of wall turbulence. *J. Fluid Mech.* **119**, 173–217.

Piomelli, U. 2008 Wall-layer models for large-eddy simulation. *Prog. Aerosp. Sci.* **44**, 437–446.

Piomelli, U. and Balaras, E. 2002 Wall-layer models for large-eddy simulations. *Annu. Rev. Fluid Mech.* **34**, 349–374.

Pope, S. B. 2000 *Turbulent Flows*. Cambridge University Press.

Pope, S. B. 2004 Ten questions concerning the large-eddy simulation of turbulent flows. *New J. Phys.* **6**, 35.

Pullin, D. I. 2000 A vortex-based model for the subgrid flux of a passive scalar. *Phys. Fluids* **12**, 2311–2319.

Pullin, D. I. and Lundgren, T. S. 2001 Axial motion and scalar transport in stretched spiral vortices. *Phys. Fluids* **13**, 2553–2563.

Pullin, D. I. and Saffman, P. G. 1993 On the Lundgren–Townsend model of turbulent fine scales. *Phys. Fluids* A **5**, 126–145.

Pullin, D. I. and Saffman, P. G. 1994 Reynolds stresses and one-dimensional spectra for a vortex model of homogeneous anisotropic turbulence. *Phys. Fluids* **6**, 1787–1796.

Robinson, S. K. 1991 Coherent motions in the turbulent boundary layer. *Annu. Rev. Fluid Mech.* **23**, 601–639.

Rogallo, R. S. and Moin, P. 1984 Numerical simulation of turbulent flows. *Annu. Rev. Fluid Mech.* **16**, 99–137.

Saddoughi, S. G. and Veeravalli, S. V. 1994 Local isotropy in turbulent boundary layers at high Reynolds number. *J. Fluid Mech.* **268**, 333–372.

Sagaut, P. 2006 *Large Eddy Simulation for Incompressible Flows: An Introduction*, 3rd edition. Springer.

Sandoval, D. L. 1995 The dynamics of variable-density turbulence. PhD thesis, University of Washington, Seattle.

Shih, L. H., Koseff, J. R., Ivey, G. N. and Ferziger, J. H. 2005 Parameterization of turbulent fluxes and scales using homogeneous sheared stably stratified turbulence simulations. *J. Fluid Mech.* **525**, 193–214.

Smagorinsky, J. 1963 General circulation experiments with the primitive equations. Part 1. The basic experiment. *Mon. Weather Rev.* **91**, 99–164.

Spalart, P. R., Moser, R. D. and Rogers, M. M. 1991 Spectral methods for the Navier–Stokes equations with one infinite and two periodic directions. *J. Comput. Phys.* **96**, 297–324.

Strand, B. 1994 Summation by parts for finite difference approximations for d/dx. *J. Comput. Phys.* **110**, 47–67.

Templeton, J. A., Medic, G. and Kalitzin, G. 2005 An eddy-viscosity based near-wall treatment for coarse grid large-eddy simulation. *Phys. Fluids* **17**, 105101.

Templeton, J. A., Wang, M. and Moin, P. 2008 A predictive wall model for large-eddy simulation based on optimal control techniques. *Phys. Fluids* **20**, 065104.

Townsend, A. A. 1976 *The Structure of Turbulent Shear Flow*, 2nd edition. Cambridge University Press.

Turner, J. S. 1973 *Buoyancy Effects in Fluids*. Cambridge University Press.

Voelkl, T., Pullin, D. I. and Chan, D. C. 2000 A physical-space version of the stretched-vortex subgrid-stress model for large-eddy simulation. *Phys. Fluids* **12**, 1810–1825.

Wang, M. and Moin, P. 2002 Dynamic wall modeling for large-eddy simulation of complex turbulent flows. *Phys. Fluids* **14**, 2043–2051.

Yeung, P. K., Donzis, D. A. and Sreenivasan, K. R. 2005 High-Reynolds-number simulation of turbulent mixing. *Phys. Fluids* **17**, 081703.